MOLECULAR IMAGING USING FEMTOSECOND LASER PULSES

by

PATRICK W. DOOLEY, M.Sc.

A Thesis
Submitted to the School of Graduate Studies
in Partial Fulfillment of the Requirements
for the Degree
Doctor of Philosophy

McMaster University

© Copyright Patrick W. Dooley, September, 2003

DOCTOR OF PHILOSOPHY (2003) McMaster University
(Physics) Hamilton, Ontario

TITLE: Molecular Imaging using Femtosecond Laser Pulses

AUTHOR: Patrick W. Dooley, M.Sc. (McMaster University)

SUPERVISOR: Professor Paul B. Corkum

NUMBER OF PAGES: x, 158

Abstract

Recent technological advances have brought the possibility of directly imaging polyatomic molecular dynamics within reach. Consequently, several diffractive and non-diffractive time-resolved imaging techniques are currently under development worldwide. The work described here was motivated by the desire to pioneer the femtosecond laser-initiated Coulomb explosion approach to molecular imaging.

The research project's original objective has been met using a unique instrument that can measure and correlate multiple three-dimensional ion velocities. Using this state-of-the-art machine, the first Coulomb explosion images of triatomic molecules have been produced. Furthermore, the apparatus has been employed to demonstrate that existing ultrafast laser technology is sufficient to confine virtually any molecule inertially during its multiple ionization.

In conjunction with the instrument's novel capabilities, the Coulomb explosion process has been exploited in numerous other applications. For instance, a time-resolved method for directly imaging rotational wave packets in diatomic molecules has been demonstrated. Further, a high-sensitivity technique has been developed for detecting nonsequential "shake-off" double ionization in molecular deuterium. In other experiments, the optical timing of ion flight has been demonstrated, which should enable the fabrication of the world's smallest time-of-flight mass spectrometer. Finally, the instrument's excellent momentum resolution has given rise to an entirely new technique for observing molecular dynamics: electron self-diffraction imaging.

Publications

This work is supported by the following publications:

Chapter 2

"Towards Timed Coulomb Explosion Imaging of Small Molecules"
P.W. Dooley, V.R. Bhardwaj, and P.B. Corkum
Proceedings of the International Conference on Lasers '99 (STS Press, McLean, VA, 2000) p. 8

Chapter 3

"Optically Timed Sub-Millimetre Time-of-Flight Mass Spectrometry"
P.W. Dooley, V.R. Bhardwaj, D.M. Rayner, and P.B. Corkum
Accepted for publication in *Analytical Chemistry* (2003)

Chapter 5

"Time-Resolved Double Ionization with Few Cycle Laser Pulses"
F. Légaré, I.V. Litvinyuk, P.W. Dooley, F. Quéré, A.D. Bandrauk, D.M. Villeneuve, and P.B. Corkum
Physical Review Letters **91** 093002 (2003)

Chapter 6

"Direct Imaging of Rotational Wave-Packet Dynamics of Diatomic Molecules"
P.W. Dooley, I.V. Litvinyuk, K.F. Lee, D.M. Rayner, M. Spanner, D.M. Villeneuve, and P.B. Corkum
Physical Review A **68** 023406 (2003)

"Alignment-Dependent Strong Field Ionization of Molecules"
I.V. Litvinyuk, K.F. Lee, P.W. Dooley, D.M. Rayner, D.M. Villeneuve, and P.B. Corkum
Physical Review Letters **90** 233003 (2003)

Acknowledgements

This dissertation represents the culmination of an endeavour to which many have lent their support and encouragement. For their generosity, I owe a great debt of gratitude to my colleagues, family, and friends.

I am principally beholden to my thesis adviser, Dr. Paul Corkum, whose insight, encouragement, and friendship have been so freely given. It has been a rare privilege to partake of the intellectually stimulating environment that is his Femtosecond Science program within the National Research Council's Steacie Institute for Molecular Sciences.

I am also indebted to the members of my supervisory committee at McMaster (Dr. Harold Haugen, Dr. Fiona McNeill, and Dr. John Preston) for their oversight and interest in my work. Further thanks are due to Dr. Haugen who (as Associate Chair of Physics and Astronomy) was instrumental in forging the link between McMaster and the National Research Council that enabled my off-campus research. A debt of gratitude is also owed to the additional thesis examiners (Dr. David Chettle, Dr. Carl Riehm (Defence Chair), Dr. Joseph Sanderson (University of Waterloo), and Dr. Ignacio Vargas-Baca). I am also grateful to the past and present staff of the Department of Physics and Astronomy (particularly Ms. Jackie Collin, Ms. Mara Esposto, Ms. Daphne Kilgour, and Ms. Wendy Malarek) for their invaluable assistance.

I deeply appreciate the support provided by numerous National Research Council personnel. Dr. Ravi Bhardwaj, Dr. Christoph Ellert, and Dr. Igor Litvinyuk each made essential contributions to the development of the experimental apparatus. Following its completion, it was my pleasure to work alongside Dr. Daniel Comtois, Mr. Kevin Lee, and Mr. François Légaré. Mr. Bert Avery, Mr. David Joines, Mr. John Parsons, and Mr. Chad Silverman furnished timely technical assistance and advice, as did Mr. Roger Coté and his staff at the M-36 machine shop. I

have profited greatly from scientific and technical discussions with Dr. David Villeneuve as well as Dr. Misha Ivanov, Dr. David Rayner, Mr. Michael Spanner, and Dr. Albert Stolow.

For her careful proofreading of this manuscript, I am indebted to Ms. Angela Cornack.

Finally, sincere thanks are due to my most influential early teachers of science, Ms. Noreen Maier and Mr. Domenic Sabetti.

Members of the Femtosecond Science Program, Steacie Institute for Molecular Sciences, National Research Council of Canada, Spring 2003

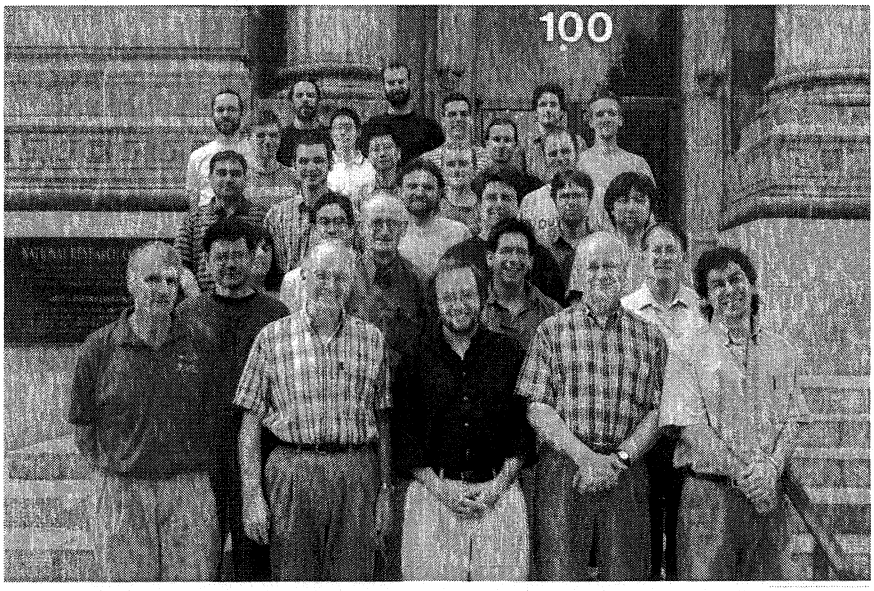

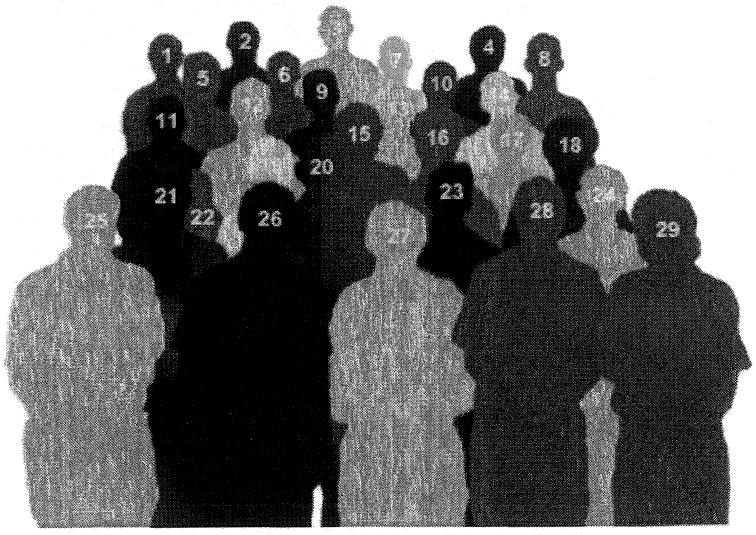

1. Zhenia Shapiro
2. Rune Lausten
3. Dirk Zeidler
4. Ben Sussman
5. Carey Luxford
6. Kevin Lee
7. Adrian Pegoraro
8. Torsten Siebert
9. Qun Zhang
10. Patrick Dooley
11. Ravi Bhardwaj
12. Justin Gagnon
13. Jérôme Levesque
14. Oliver Geβner
15. Igor Litvinyuk
16. François Légaré
17. Daniel Comtois
18. Hiromichi Niikura
19. Jiro Itatani
20. John Parsons
21. Shutao Li
22. Susanne Ullrich
23. Bert Avery
24. David Joines
25. David Rayner
26. Paul Corkum
27. Misha Ivanov
28. David Villeneuve
29. Albert Stolow

Absent

Shahruhk Alavi
Anthony Lee
Andrei Naumov
Marc Smits
Jonathan Underwood
Gennady Yudin

Table of Contents

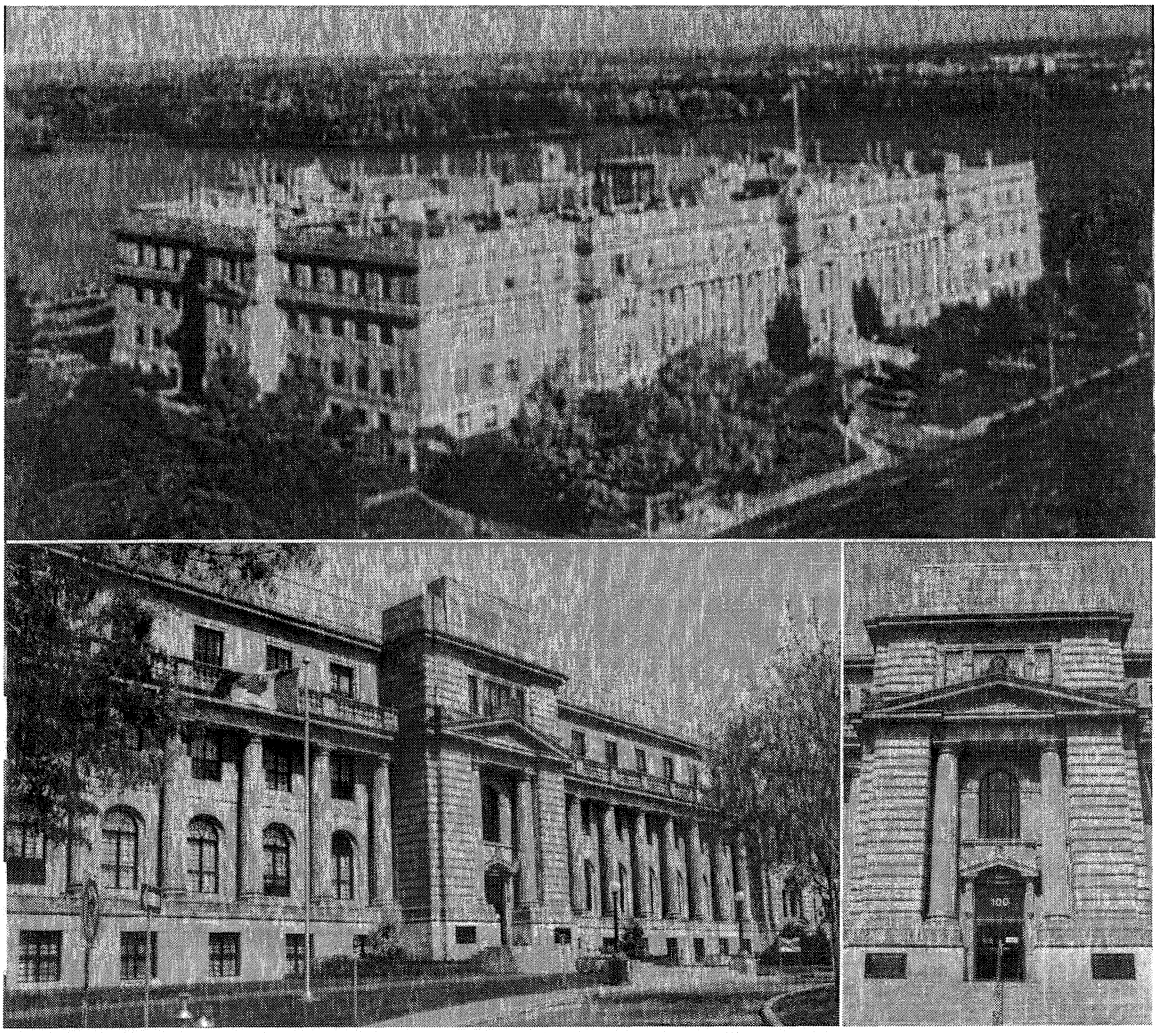

The National Research Council's Sussex Drive Laboratories, Ottawa, Ontario, Spring 2003.

List of Figures

Chapter 2: Molecular Imaging Technology

Chapter 3: Optically Timed Sub-Millimetre Mass Spectrometry

Chapter 4: Two-Fragment Correlation Experiments

Chapter 5: Time-Resolved Coulomb Explosion Imaging

Chapter 6: Imaging of Rotational Wave-Packet Dynamics

Chapter 1

Overview of Molecular Imaging

"Omnia mutantur, nos et mutamur in illis"
(All things change, and we change with them)
– Matthias Borbonius, *Deliciæ Poetarum Germanorum*, i. 685

1.1 The Structure of Molecules

The human environment is primarily a molecular one since molecules participate in virtually all terrestrial processes, both natural and man-made. They are so pervasive and fundamental to our common experience that all natural sciences can be described in molecular terms. Put simply, chemistry is the study of the mechanisms, rates, and products of interactions between molecules. Similarly, biochemistry is the study of how large molecules mediate fundamental processes in living organisms. In this context, biology represents our knowledge of the collective behaviour of extremely complex molecular systems. Whereas molecular interactions form the basis of each of these sciences, the study of the structure and internal dynamics of molecules is the province of chemical physics.

The composition and structure of matter has been a subject of scientific inquiry for nearly two and a half millennia. The earliest theory is that of Empedocles of Acragas (B.C. 495-435), who postulated that all matter consists of atomic elements (air, earth, fire, and water), combined in varying proportions, and held together by *philia* (Love) [Sar1993]. Numerous advances have refined our understanding of molecular structure, most notably Newton's mechanics [New1687], Mendeleev's formulation of the periodic table of elements [Men1869], Thomson's discovery of the electron [Tho1897], Rutherford's discovery of the atomic nucleus [Rut1911], the advent of

quantum mechanics [Pla1901], Bohr's planetary model of the atom [Boh1913], and Lewis' shared electron pair model of the chemical bond [Lew1916]. Nevertheless, our present model bears a fundamental resemblance to that of Empedocles i.e., a molecule consists of atoms (albeit of 114 possible varieties rather than four) coupled by chemical bonds.

Frequency Domain Spectroscopy

Our present knowledge of molecular structure is derived primarily from frequency-domain spectroscopy i.e., the study of periodic molecular motion. Its basis can be understood through analogy with Newtonian mechanics. Classically, a diatomic molecule is equivalent to two masses coupled by a spring. If the masses are known, the spring's force constant and length can be determined by measuring the system's respective vibrational and rotational frequencies [Ser1990]. Similarly, the bond strength and equilibrium length of a diatomic molecule can be determined from its vibrational and rotational spectra. For polyatomic molecules, additional stretching, bending, and torsional oscillations are possible. Consequently, the determination of molecular structure via spectroscopic means rapidly becomes more difficult as the number of constituent atoms increases. Nevertheless, by the mid-twentieth century, the structure of most small molecules had been determined using pre-laser techniques by pioneers such as Herzberg [Her1989, Her1991a, Her1991b]. With the invention of the laser in 1960 [Sch1958, Mai1960], the era of high-resolution spectroscopy began.

Spectroscopic studies influenced many fields of modern science. For example, the struggle to understand molecular spectra spurred the growth of quantum mechanics. Further, the ability to analyze the chemical compositions of stars and interstellar media revolutionized observational astronomy. Finally, numerous modern diagnostic technologies such as biomedical imaging and environmental monitoring are based largely on frequency domain spectroscopy.

Diffraction Techniques

Despite frequency domain spectroscopy's many successes, it is ill-suited for structural determinations of large molecules since their spectra are too complex. To address the problem of large molecules, a variety of diffraction techniques were developed concurrently with spectroscopy [Sto1968, Glu1972, Goo1981, Har1988, Kar2000]. In a diffraction experiment, a molecular sample is bombarded with a beam of particles (e.g. X-ray photons, electrons, or neutrons) whose de Broglie wavelength is shorter than bond lengths within the target. From the particle scattering pattern, information regarding the structure of the molecule can be derived. The earliest demonstrations of diffraction from solid targets were performed using X-rays in 1912 [Fri1912, von1912] and electrons in 1927 [Dav1927]. X-ray and electron diffraction from gas-phase molecules were first demonstrated in 1929 [Deb1929] and 1930 [Mar1930], respectively. During the 1950's, Brockhouse and Shull conducted pioneering neutron scattering experiments. Over the last century, diffraction techniques have been used to determine the structure of countless crystalline materials.

Our structural knowledge of biomolecules also stems largely from diffraction experiments. The structures of DNA [Wat1953], the first protein [Ken1958], and the first enzyme [Bla1965] were determined using X-ray diffraction. The introduction of the synchrotron as an X-ray source for diffraction measurements [Par1959] in the 1960's increased both the achievable flux and spatial resolution. Ever larger synchrotrons continue to be built, driven mainly by the need for improved molecular imaging. However, the structures of most large molecules cannot be determined using existing X-ray sources for two reasons. First, the X-ray diffraction process is so weak that even the most advanced synchrotrons are insufficient for structural determinations of single biomolecules. As a result, experiments are performed on crystalline samples whose long range ordering of replica molecules greatly amplifies the

diffracted signal. Unfortunately, the applicability of this approach is limited since the vast majority of large molecules cannot be crystallized. Second, even if a synchrotron of sufficient power could be constructed for high-resolution single molecule studies, its high X-ray flux would destroy most large molecules during the measurement process [Hen1995] unless the pulse is ultrashort [Neu2000].

Coulomb Explosion Imaging

Developed in 1979 [Kan1979], Coulomb explosion imaging is a non-diffractive technique that applies methods used in nuclear and elementary particle physics to the problem of molecular structure determination [Vag1989, Zaj1995, Lev1998]. In a Coulomb explosion imaging measurement, a molecular ion is accelerated to an extremely high (MeV) kinetic energy before impinging on an ultrathin (~100 Å) foil target. Many electrons are stripped from the molecular ion during its ~0.1 fs (1 fs = 10^{-15} s) passage through the foil. Upon its emergence, the highly charged molecular ion explodes due to Coulomb repulsion between its positive atomic cores. By determining the three-dimensional velocity of each fragment, the structure of the molecular ion prior to its passage through the foil can be inferred. Unfortunately, Coulomb explosion imaging is applicable only to small molecules due to technological constraints. Since the structure of most small molecules had been determined via frequency domain spectroscopy prior to the development of Coulomb explosion imaging, the technique's impact has been limited.

1.2 The Dynamics of Molecules

A fundamental result of quantum mechanics is that the structure of every molecule is continually changing. Moreover, a molecule's dynamical behaviour is as characteristic as the equilibrium structures it can assume and affects its participation in chemical reactions.

Consequently, it is essential to develop dynamical imaging techniques if we are to understand (and perhaps control) molecular processes fully.

Existing structural determination techniques are generally unsuitable for imaging molecular dynamics. Since a molecule's motion may be aperiodic during important dynamical processes, oscillation frequencies are poorly defined and frequency domain spectroscopy is of limited utility. Since molecular motion typically occurs on a femtosecond time scale, it proceeds far too quickly for imaging with conventional diffraction techniques.

Time Domain Spectroscopy

The development of time domain spectroscopy began in the late 1980's and represents the first time-resolved approach for observing molecular dynamics [Zew1994, Sun1997, Cas1998]. The technique employs the briefest man-made phenomena ever produced – ultrashort laser pulses. Currently, pulse durations of ~1 fs can be generated [Hen2001] that are to one second as six minutes are to the age of the universe. In analogy with a photographic camera, a femtosecond pulse can serve as an ultrafast shutter capable of "freezing" molecular motion in a dynamics experiment. In time domain spectroscopy, two femtosecond pulses are employed in a "pump-probe" experiment. The first (pump) pulse is tailored to initiate particular dynamical behaviour in a molecule that continues until the arrival of the second (probe) pulse. The probe pulse further excites the molecule and yields a spectrum from which the instantaneous molecular structure can be inferred. By varying the delay between the pump and probe pulses, the time evolution of the molecule's structure can (in principle) be observed.

Insight regarding the dynamics of small molecules garnered using time domain spectroscopy resulted in the award of the 1999 Nobel Prize in Chemistry to its pioneer, Ahmed Zewail [Zew1999]. Unfortunately, precise knowledge of molecular potential surfaces,

polarizabilities, dipole moments, and/or transition dipole moments is required in order to derive a molecule's structure correctly from its spectrum. Consequently, structures deduced for small molecules using time domain spectroscopy are typically open to interpretation while those of large molecules are virtually impossible to ascertain.

Non-Spectroscopic Imaging Techniques

Four new techniques for imaging molecular dynamics are currently under development: femtosecond X-ray diffraction [Bad1983, Ber1986, Ben1997, Cao1998, Neu2000], ultrafast electron diffraction [Wil1991, Wil1997, Dud2001, Ihe2001, Ihe2002], femtosecond electron self-diffraction, and time-resolved Coulomb explosion imaging [Che1999, Doo2000]. The four approaches are described in turn below and have the following common features:

(1) dynamics are observed by imaging a molecule's structure at a different times using a pump-probe method,

(2) a femtosecond laser pulse is used to initiate the molecular dynamics,

(3) a femtosecond laser pulse either serves as (or is used to generate) the probe pulse, and

(4) at each pump-probe delay, the probe pulse initiates a particle scattering (rather than spectroscopic) measurement from which structural information is derived.

Femtosecond X-ray Diffraction Imaging

Efforts are underway to increase the intensity of coherent pulsed X-ray sources. With sufficient intensity, high-resolution structural imaging of a single molecule using a single femtosecond X-ray probe pulse may be possible [Neu2000]. While such a high X-ray flux would make molecular crystallization unnecessary, it would also trigger the explosion of the molecule. Therefore, to obtain a clear structural image, the X-ray pulse duration must be sufficiently short to complete the scattering measurement before appreciable molecular deformation occurs. In

Chapter 5, we demonstrate that molecular deuterium (the third-lightest molecule) explodes on a time scale of just a few femtoseconds. At present, X-ray pulse durations are limited to a few hundred femtoseconds or more and intense sources are under discussion. Additional impediments to the realization of molecular imaging via ultrafast X-ray diffraction include the necessities of generating, collimating, and transporting X-ray pulses *in vacuo* and synchronizing them to ultrashort optical pump pulses with femtosecond precision [Ben1997].

Ultrafast Electron Diffraction Imaging

While ultrafast electron and X-ray diffraction techniques are conceptually similar [Ben1997], the charged nature of electrons gives rise to key differences. Due to Coulomb repulsion, molecular scattering probabilities are several orders of magnitude greater for electrons than for hard X-rays. As a result, electron diffraction techniques require much lower particle fluxes than equivalent X-ray scattering methods. Unfortunately, the lack of long-range molecular order in the gas phase results in very weak scattering signals in either case. Furthermore, electron-electron repulsion also limits the temporal resolution of ultrafast electron diffraction measurements. While an ultrashort optical pulse can produce a femtosecond electron burst via the photoelectric effect, Coulomb repulsion can drastically increase the electron pulse duration en route to the molecular interaction region. Consequently, ultrafast electron diffraction measurements involve a compromise between the pulse duration and the number of electrons per pulse [Wil1997]. To achieve picosecond temporal resolution in a state-of-the-art measurement, the number of electrons per pulse is limited to several thousand [Ihe2002]. Finally, pump-probe synchronization is particularly challenging in ultrafast electron diffraction measurements since the velocities of the optical pump and electronic probe pulses differ [Wil1993]. Despite the

considerable technical challenges involved, picosecond dynamical processes in several molecules have been observed using ultrafast electron diffraction imaging [Ihe2001].

Electron Self-Diffraction Imaging

During the course of this work, the concept for a novel molecular imaging technique was developed. In an electron self-diffraction imaging experiment, an intense femtosecond laser probe pulse is used to ionize a molecule. The strong laser field then dictates the motion of the liberated electron, accelerating it first away from then back toward the parent ion. The electron can then diffract from the parent ion during its re-encounter with it. Analysis of either the scattered electron or the recoiling parent ion momentum should then yield structural information regarding the molecule.

There are several advantages to using a molecule's own electron to determine its structure, relative to the ultrafast electron diffraction technique described above. Since only a single electron is involved, space charge effects do not degrade the time resolution of the measurement, which can be a femtosecond or less. Furthermore, the electron is localized in the vicinity of the parent ion upon its return. As a result, the effective electron current incident on the molecule can be many orders of magnitude greater than that achievable using an externally generated electron pulse. Finally, the synchronization of the pump and probe pulses is straightforward in an electron self-diffraction experiment since both can be produced by the same laser.

During the past year and a half, we have striven to perform the first unambiguous demonstration of electron self-diffraction imaging. While this has recently been achieved, our results are not described here.

Time-Resolved Coulomb Explosion Imaging

During the past decade, advances in ultrafast laser technology have given rise to ever shorter and more intense pulses. Currently, pulse durations as short as 650 attoseconds (1 as = 10^{-18} s) can be generated [Hen2001] and intense 5 fs pulses [Nis1997] can initiate molecular explosion. With such intense, ultrashort pulses, it should be possible to determine the structure of small molecules using an optical analogue of Coulomb explosion imaging [Sta1995, Ell1998, Con1999]. Moreover, the performance of laser-triggered Coulomb explosion imaging as the second step of a pump-probe experiment would constitute a novel, all-optical time-resolved technique for imaging molecular dynamics. The development of the time-resolved Coulomb explosion technique was the original motivation for this work. Chapter 5 summarizes our progress in using laser-triggered Coulomb explosion imaging to determine molecular structure. In Chapter 6, we use Coulomb explosion to image the rotational wave-packet dynamics of molecular nitrogen and oxygen.

1.3 Chapter Overview

The four non-spectroscopic approaches to molecular imaging described above can be categorized as follows. "Full scattering" techniques, such as ultrafast X-ray and electron diffraction, involve the scattering of an externally generated pulsed particle beam from a molecule. These methods require careful synchronization of the optical pump and scattering pulses, lack the excellent temporal resolution afforded by the shortest laser pulses, and are being developed elsewhere. In contrast, "half-scattering" techniques, such as electron self-diffraction and time-resolved Coulomb explosion imaging, involve the laser-initiated scattering of particles intrinsic to the molecule under study. For such methods, pump and probe pulses can originate

from the same laser. This greatly simplifies their synchronization and makes femtosecond temporal resolution readily achievable.

The desire to pioneer half-scattering approaches for molecular imaging has motivated this work. Our progress towards using molecules to measure themselves is presented as follows:

Chapter 2

Molecular imaging is a technology-intensive endeavour. The state-of-the-art technology we originally developed for the performance of laser Coulomb explosion imaging (but which enables all of the following experiments) is described in this chapter. In the field of molecular imaging, our experimental apparatus is unique in two respects. First, we employ an ultrathin (~40 μm thick) molecular beam that allows us to confine molecules to the high intensity region of our laser focal volume. Second, we employ a multiple hit, three-dimensional ion imaging detector. Consequently, particular emphasis is placed on these two aspects.

Chapter 3

A non-imaging experiment is described in which we use a femtosecond pump-probe technique to time molecular ion flight optically. In so doing, we demonstrate a nested mass spectrometric configuration that incorporates what is effectively the world's smallest time-of-flight mass spectrometer. The configuration is suitable for molecular dynamics experiments on neutral-free ensembles of molecular ions and could greatly reduce the size of portable mass analyzers.

Chapter 4

Our ability to identify correlations amongst the three-dimensional momenta of ion pairs is demonstrated in this chapter. This capacity enables us to isolate ions that originate from a common molecule and is a prerequisite for the performance of laser-initiated Coulomb explosion

imaging. Since they can be nearly background-free, correlation techniques can also facilitate studies of low probability phenomena. As an illustration, the results of a search for direct, simultaneous double ionization of molecular deuterium are presented.

Chapter 5

In this chapter, technical challenges to the realization of laser Coulomb explosion imaging are addressed. For the technique to yield a true image, the structure of a molecule must not change appreciably during electron removal. Therefore, multiple ionization must be rapid not only on the time scale of the neutral molecule's motion, but also on that of the Coulomb explosion process. Using the "molecular clock" concept, we have timed the delay between the first and second electron removals from molecular deuterium. The results show that the structures of all molecules remain approximately static during ionization by pulses with durations of 5 fs or less. The technique's prerequisites also include the ability to perform multiple particle correlation measurements and to determine molecular structures from the Coulomb explosion data. As an illustration of our current capabilities, experimentally obtained structural information for heavy water and sulphur dioxide are presented along with time-resolved measurements of molecular deuterium and sulphur dioxide.

Chapter 6

In this chapter, pump-probe experiments are described in which Coulomb explosion was used to observe the rotational wave-packet dynamics of diatomic molecules. A rotational wave packet was launched in either molecular nitrogen or oxygen by the femtosecond pump pulse. During the wave packet's evolution, distributions of molecular orientations were measured by exploding molecules using the intense probe pulse. In this manner, we have observed net wave-

packet alignment, dephasing, and a variety of revival behaviour. Our ability to produce aligned rotational wave packets ultimately enabled our demonstration of electron self-diffraction imaging.

1.4 References

[Bad1983] P. Bado, P.H. Berens, J.P. Bergsma, M.H. Coladonato, C.G. Dupuy, P.M. Edelsten, J.D. Kahn, K.R. Wilson, and D.R. Fredkin, *Laser Chem.* **3** 231 (1983).

[Ben1997] M. Ben-Nun, J. Cao, and K.R. Wilson, *J. Phys. Chem. A* **101** 8743 (1997).

[Ber1986] J.P. Bergsma, M.H. Coladonato, P.M. Edelsten, K.R. Wilson, and D.R. Fredkin, *J. Chem. Phys.* **84** 6151 (1986).

[Bla1965] C.C. Blake, D.F. Koenig, G.A. Mair, A.C. North, D.C. Phillips, and V.R. Sarma, *Nature* **206** 757 (1965).

[Boh1913] N. Bohr, *Philos. Mag.* **6(26)** 1 (1913).

[Cao1998] J. Cao and K.R. Wilson, *J. Phys. Chem. A* **102** 9523 (1998).

[Cas1998] A.W. Castleman Jr. and V. Sundström, eds., special issue on Ten Years of Femtochemistry, *J. Phys. Chem. A* **102** 4021 (1998).

[Che1999] S. Chelkowski, P.B. Corkum, and A.D. Bandrauk, *Phys. Rev. Lett.* **82** 3416 (1999).

[Con1999] E. Constant, H. Stapelfeldt, H. Sakai, and P.B. Corkum, *Comments At. Mol. Phys.* **1** 85 (1999).

[Dav1927] C. Davisson and L.H. Germer, *Phys. Rev.* **30** 705 (1927).

[Deb1929] P. Debye, L. Bewilogua, and F. Ehrhardt, *F. Phys. Z.* **30** 84 (1929).

[Doo2000] P.W. Dooley, V.R. Bhardwaj, and P.B. Corkum in *Proceedings of the International Conference on Lasers '99* (STS Press, McLean, VA, 2000), p.8.

[Dud2001] R.C. Dudek and P.M. Weber, *J. Phys. Chem. A* **105** 4167 (2001).

[Ell1998] Ch. Ellert, H. Stapelfeldt, E. Constant, H. Sakai, J. Wright, D.M. Rayner, and P.B. Corkum, *Phil. Trans. R. Soc. Lond. Ser. A* **356** 329 (1998).

[Fri1912] W. Friedrich, P. Knipping, and M. von Laue, *Sitzber. Ko"nig. Bayer. Akad. Wiss.* 303 (1912).

[Glu1972] J.P. Glusker and K.N. Trueblood, *Crystal Structure Analysis* (Oxford University Press, New York, NY, 1972).

[Goo1981] P. Goodman, ed., *Fifty Years of Electron Diffraction* (Reidel, Dordrecht, Netherlands, 1981).

[Har1988] I. Hargittai and M. Hargittai, eds., *Stereochemical Applications of Gas-Phase Electron Diffraction* (VCH, New York, NY, 1988).

[Hen1995] R. Henderson, *Q. Rev. Biophys.* **28** 171 (1995).

[Hen2001] M. Hentschel, R. Kienberger, Ch. Spielmann, G.A. Reider, N. Milosevic, T. Brabec, P. Corkum, U. Heinzmann, M. Drescher, and F. Krausz, *Nature* **414** 509 (2001).

[Her1989] G. Herzberg, *Molecular Spectra and Molecular Structure: Spectra of Diatomic Molecules*, 2nd ed. (Krieger Publishing, Melbourne, FL, 1989).

[Her1991a] G. Herzberg, *Molecular Spectra and Molecular Structure: Electronic Spectra and Electronic Structure of Polyatomic Molecules* (Krieger Publishing, Melbourne, FL, 1991).

[Her1991b] G. Herzberg, *Molecular Spectra and Molecular Structure: Infrared and Raman of Polyatomic Molecules* (Krieger Publishing, Melbourne, FL, 1991).

[Ihe2001] H. Ihee, V.A. Lobastov, U.M. Gomez, B.M. Goodson, R. Srinivasan, C.-Y. Ruan, and A.H. Zewail, *Science* **291** 458 (2001).

[Ihe2002] H. Ihee, B.M. Goodson, R. Srinivasan, V.A. Lobastov, and A.H. Zewail, *J. Phys. Chem. A* **106** 4087 (2002).

[Kan1979] E.P. Kanter, P.J. Cooney, D.S. Gemmell, K.O. Groeneveld, W.J. Pietsch, A.J. Ratkowski, Z. Vager, and B.J. Zabranski, *Phys. Rev. A* **20** 834 (1979).

[Kar2000] J. Karle, *Structural Chem.* **11** 91 (2000).

[Ken1958] J.C. Kendrew, G. Bodo, H.M. Dintzis, R.G. Parrish, H. Wyckoff, and D.C. Phillips, *Nature* **181** 662 (1958).

[Lev1998] J. Levin, H. Feldman, A. Baer, D. Ben-Hamu, O. Heber, D. Zajfman, and Z. Vager, *Phys. Rev. Lett.* **81** 3347 (1998).

[Lew1916] G.N. Lewis, *J. Am. Chem. Soc.* **38** 762 (1916).

[Mai1960] T.H. Maiman, *Nature* **187** 493 (1960).

[Mar1930] H. Mark and R. Wierl, *Naturwissenschaften* **18** 205 (1930).

[Men1869] D. Mendelejeff, *Z. Chem.* **12** 405 (1869).

[Neu2000] R. Neutze, R. Wouts, D. van der Spoel, E. Weckert, and J. Hajdu, *Nature* **406** 752 (2000).

[New1687] I. Newton, *Principia*, 1697.

[Nis1997] M. Nisoli, S. De Silvestri, O. Svelto, R. Szipöcs, K. Ferencz, Ch. Spielmann, S. Sartania, and F. Krausz, *Opt. Lett.* **22** 522 (1997).

[Par1959] L.G. Parratt, *Rev. Sci. Instrum.* **30** 297 (1959).

[Pla1901] M. Planck, *Ann. Phys. (Leipzig)* **4** 553 (1901).

[Rut1911] E. Rutherford, *Philos. Mag.* **6(21)** 669 (1911).

[Sar1993] G. Sarton, *Ancient Science through the Golden Age of Greece* (Dover Publications, New York, NY, 1993).

[Sch1958] A.L. Schawlow and C.H. Townes, *Phys. Rev.* **112** 1940 (1958).

[Ser1990] R.A. Serway, *Physics for Scientists & Engineers with Modern Physics* (Saunders College Publishing, Toronto, ON, 1990).

[Sta1995] H. Stapelfeldt, E. Constant, and P.B. Corkum, *Phys. Rev. Lett.* **74** 3780 (1995).

[Sto1968] E.G. Stout and L.H. Jensen, *X-Ray Structure Determination: A Practical Guide* (Macmillan, New York, NY, 1968).

[Sun1997] V. Sundström, ed., *Femtochemistry and Femtobiology: Ultrafast Reaction Dynamics at Atomic-Scale Resolution* (World Scientific, Singapore, 1997).

[Tho1897] J.J. Thomson, *Philos. Mag.* **44** 295 (1897).

[Vag1989] Z. Vager, R. Naaman, and E.P. Kanter, *Science* **244** 426 (1989).

[von1912] M. von Laue, *Sitzber. Ko"nig. Bayer. Akad. Wiss.* 363 (1912).

[Wat1953] J.D. Watson and F.H.C. Crick, *Nature* **171** 737 (1953).

[Wil1991] J.C. Williamson and A.H. Zewail, *Proc. Natl. Acad. Sci.* **88** 5021 (1991).

[Wil1993] J.C. Williamson, *Chem. Phys. Lett.* **209** 472 (1993).

[Wil1997] J.C. Williamson, J. Cao, H. Ihee, H. Frey, and A.H. Zewail, *Nature* **386** 159 (1997).

[Zaj1995] D. Zajfman and Z. Amitay, *Phys. Rev. A* **52** 839 (1995).

[Zew1994] A.H. Zewail, *Femtochemistry: Ultrafast Dynamics of the Chemical Bond* (World Scientific, Singapore, 1994).

[Zew1999] A.H. Zewail in *Les Prix Nobel* (Almqvist & Wiksell, Stockholm, Sweden, 1999), p. 110.

Chapter 2

Molecular Imaging Technology

The **P**osition- **a**nd **T**ime-**R**esolved **I**on **C**orrelation **K**it (PATRICK) apparatus is the state-of-the-art instrument constructed during this project for the performance of molecular imaging (Fig. 2.1). Its *f*/2 parabolic mirror and ultrathin molecular beam enable the application of intense laser fields to single gas-phase molecules. A high-resolution time-of-flight spectrometer and specialized detector are used to collect and analyze ions produced in the laser focus. In this manner, the three-dimensional initial velocities of up to sixteen ions per laser pulse can be determined. Through correlation analysis of the velocity data, ions that originate from a common parent molecule can be identified.

2.1 Femtosecond Laser System

A multi-gigawatt femtosecond laser system constructed by NRC staff was used in this work. The Kerr lens mode-locked Ti:sapphire oscillator is pumped by a 5 W argon ion laser

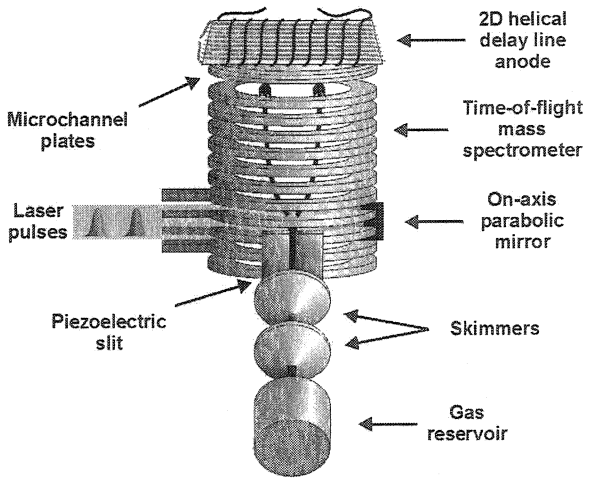

Fig. 2.1. Schematic representation of the PATRICK instrument. *The nozzle of an interchangeable reservoir produces a gas jet that is successively collimated by two beam skimmers and an adjustable slit. Ions are produced from the resulting ultrathin ribbonlike molecular beam using femtosecond laser pulses focused by a translatable parabolic mirror. A static, homogeneous electric field generated within the ring electrodes of a time-of-flight mass spectrometer accelerates the ions toward a helical delay line anode detector. The time and two-dimensional position of each ion impact are recorded. Initial three-dimensional ion velocities are then calculated from the data, from which molecular structural information can be derived.*

(Coherent Innova 310) and produces 20 fs, 15 nJ, 800 nm wavelength pulses at a repetition rate of 80 MHz. The use of a thin (4 mm) laser crystal and a fused silica prism pair results in a low third-order dispersion cavity [Hua1992]. A beam splitter divides the oscillator output into two trains of 7.5 nJ pulses, only one of which is relevant to this work. In the first stage of a chirped pulse amplification scheme [Str1985], negative dispersion is introduced to one of the trains, increasing its pulse durations to 100 ps. The pulse stretcher consists of a double-passed grating pair with an internal Newtonian telescope in a near-4*f* imaging arrangement [Mar1987]. The stretched train is passed to a regenerative amplifier consisting of a Brewster-cut Ti:sapphire crystal pumped by a 10 W frequency-doubled Nd:YLF laser (Positive Light Merlin), two curved end mirrors, a quarter wave plate, a polarizing beam splitter, and two Pockels cells operated at either zero- or quarter-wave voltages. The voltage of the input Pockels cell is set to reject the vast majority of 100 ps seed pulses and only a single pulse is permitted to circulate within the cavity at a given time. Once switched into the cavity, a pulse makes thirteen passes through the gain medium and acquires 1.7 mJ of energy before being switched out by the output Pockels cell. A double-passed grating pair is used to compress the 100 ps amplifier output and yields recompressed 39 fs, 900 μJ recompressed pulses with an M^2 value of 1.5. For experiments that require even shorter pulses, self-phase modulation in a hollow core fibre is performed [Nis1997]. Following pulse compression with chirped dielectric mirrors, the 100 μJ pulses have a minimum duration of 6 fs and an M^2 value of 1.1. For experiments that require a wavelength other than 800 nm, a commercial optical parametric amplifier (Quantronix TOPAS) is available. The OPA produces 60 fs, 200 μJ total (signal plus idler) energy pulses over a wavelength range of 1.15 μm to 2.6 μm.

2.2 Vacuum Chambers

The PATRICK apparatus consists of three interconnected stainless steel vacuum chambers (source, intermediate, and detector) designed and fabricated at the National Research Council (Fig. 2.2). The chambers are separated by 1 mm-diameter electroformed nickel skimmers (Beam Dynamics model 1) and are differentially pumped. The source and intermediate chambers are welded together via a coupling flange that supports a removable skimmer on the source chamber side. The intermediate and detector chambers are separable and coupled by a skimmer-bearing ConFlat gate valve used to isolate the detector chamber during source chamber

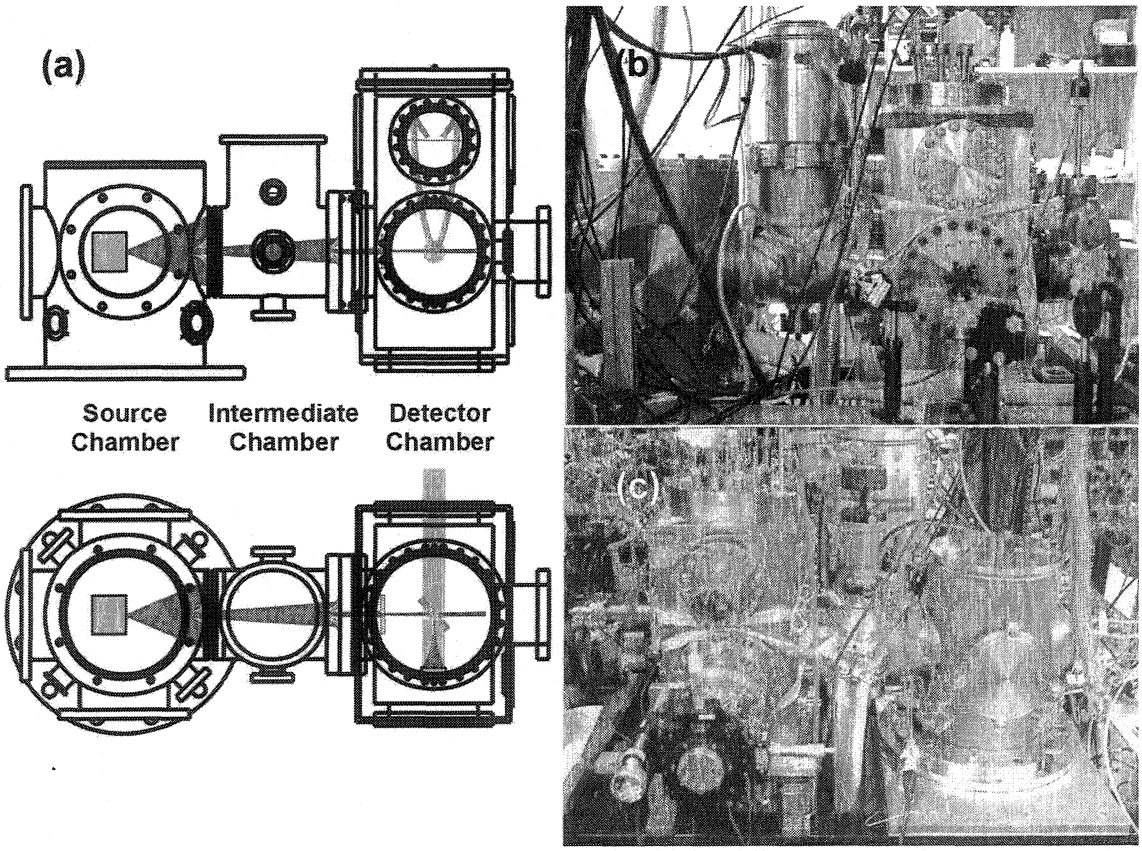

Fig. 2.2. The PATRICK instrument. *(a) Side (upper drawing) and top (lower drawing) views of the coupled source, intermediate, and detector chambers. The instrument's three orthogonal design axes are also shown. In the upper drawing, the molecular beam travels from left to right, the laser propagates normal to the page, and ions are accelerated upwards. (b) Photograph of apparatus equivalent to the upper drawing in (a). The laser beam enters at bottom right. (c) Reverse view of chambers. The parabolic mirror translator is shown at bottom left.*

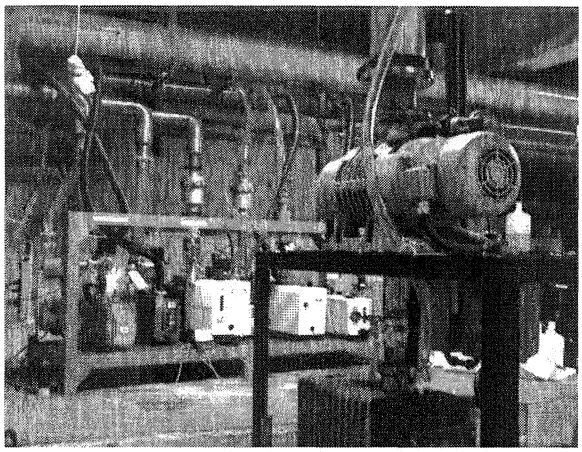

Fig. 2.3. Vacuum chamber backing pumps. *In the foreground are the rotary pump (bottom) and roots blower (middle) that back the source chamber's diffusion pump via a 6" diameter steel vacuum line (top). At back left are two rotary pumps that provide rough vacuum to the intermediate and detector chambers. A third rotary pump is used for gas manifold evacuation. Directly above the rotary pumps are vacuum lines consisting of short sections of reinforced hose and 4" diameter copper tubes. The copper lines exit at top left before running upward to the floor above.*

maintenance. The detector chamber is fixed to a tubular steel frame that supports all three chambers. The source and intermediate chambers are mounted to an aluminum plate with Teflon pads on its underside. The padded plate can be slid atop the steel frame when the intermediate and detector chambers are decoupled.

One or more mechanical pumps back each of the chambers' high and ultrahigh vacuum pumps. The rough vacuum pumps are located one floor beneath the laboratory to isolate the noise and heat they produce (Fig. 2.3). To minimize vibration, the vacuum lines consist of 4" O.D. copper tubes (or 6" O.D. stainless steel in the case of the source chamber) rigidly coupled to the building's concrete foundation with flexible reinforced hose sections or steel bellows at either end. Cooling water is supplied to the main vacuum pumps from a recirculating chilled water loop.

Source Chamber

The source chamber is cylindrical with a height of 15 inches, an outer diameter of 10.75 inches, and has an ultimate pressure of 9×10^{-8} mbar (Fig. 2.4). It is equipped with an O-ring-sealed top flange, three ISO NW160 side flanges, and four instrument ports (two ISO NW40 and two 2.75" ConFlat flanges). A 2000 L/s diffusion pump (BOC Edwards model Diffstak 250/2000M with Santovac 5 fluid) equipped with a manual butterfly valve is suspended from the

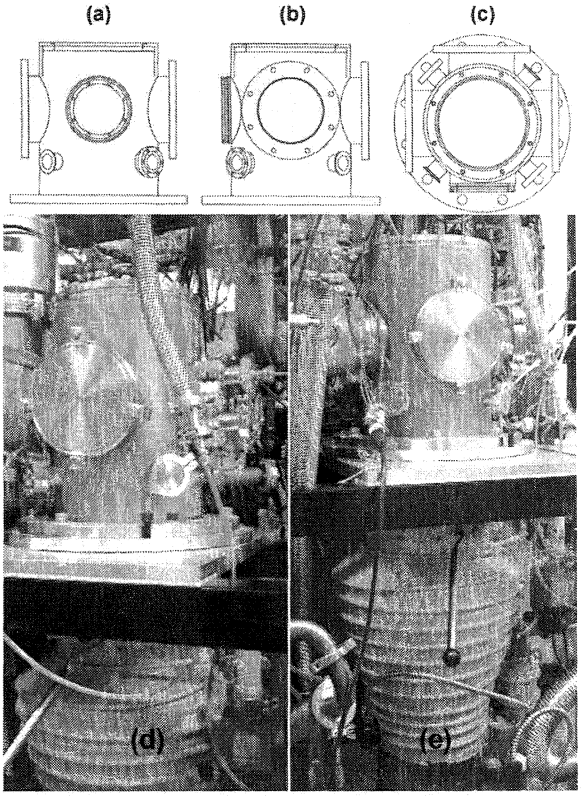

Fig. 2.4. The source chamber. *(a)-(b) Side and (c) top views are shown. The molecular beam propagates out of the page in (a), from right to left in (b), and from top to bottom in (c). (d) Photograph similar to (b) showing the gas input flange (right), the diffusion pump (bottom), and the intermediate chamber (left). The source and intermediate chambers are mounted upon a Teflon-padded aluminum plate (centre) that can be slid atop the apparatus' black tubular steel frame. (e) View of source chamber showing the diffusion pump and backing lines.*

bottom flange, backed by a roots blower and rotary pump, and provides chamber evacuation. An inverted magnetron cold cathode gauge and analogue convection transducer (MKS Instruments Series 903 and 907, respectively, with PDR 9000 readout) are used for pressure monitoring. The flange separating the source and intermediate chambers features three pins located at the vertices of an equilateral triangle centred on the molecular beam design axis of the PATRICK apparatus. The ISO flanges' Viton O-ring seals and the Kapton insulation of the skimmer heating elements limit the chamber's bake-out temperature to ~150 C.

Intermediate Chamber

The intermediate chamber is a tubular inverted "T" roughly 8.5 inches long and 11.75 inches high used exclusively for differential pumping of the apparatus (Fig. 2.5). A 550 L/s turbomolecular pump (Varian model V550) backed by a rotary pump is mounted upon the chamber's ISO NW160 top flange and provides an ultimate pressure of 1×10^{-8} mbar. An 8" ConFlat flange couples the chamber to the gate valve that separates it from the detector chamber. The chamber is also fitted with one ISO NW25 and three 2.75" ConFlat instrument ports. Pressure monitoring is performed using Bayard-Alpert ionization and thermocouple gauges

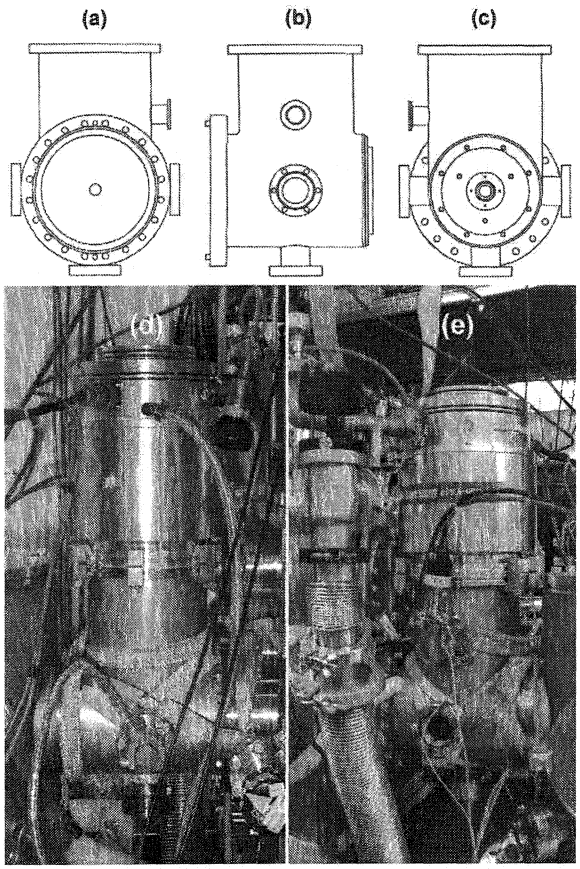

Fig. 2.5. The intermediate chamber. *(a)-(c) Side views of the chamber. The molecular beam propagates out of the page in (a), from right to left in (b), and into the page in (c). Facing outward in (a) and (c) are the source and intermediate skimmer mounting flanges, respectively. (d) Side view of chamber. The molecular beam propagates from left to right. The turbomolecular pump (top), source chamber (left) and gate valve leading to the detector chamber (bottom right) are also shown. (e) Side view of chamber similar to that in (b). The chamber's roughing line is shown in the foreground at left.*

(Varian models UHV-24 with thorium-iridium filament and 536, respectively, with Multi-Gauge controller). While the ionization gauge provides a continuous low-temperature bake-out, a halogen bake-out lamp has also been incorporated into the chamber. The thermocouple gauge heads and the Viton O-rings that seal the ISO flanges limit the maximum bake-out temperature.

Detector Chamber

The detector chamber is boxlike (Fig. 2.6) with interior dimensions of 12 inches (along the laser propagation direction) by 8 inches (along the molecular beam direction) by 17 inches (along the time-of-flight mass spectrometer axis). A 500 L/s turbomolecular pump (Edwards BOC model EXT501) backed by a rotary pump is mounted to the chamber's 8" ConFlat bottom flange and yields an ultimate pressure of 9×10^{-10} mbar. Opposite the side-mounted 8" ConFlat gate valve-coupling flange, inline with the molecular beam, is a 6" ConFlat flange to which a cryogenic beam trap can be attached. The laser propagation axis passes through the centre of two 8" ConFlat flanges. The first flange supports the BK7 glass laser input window (1.5 inch

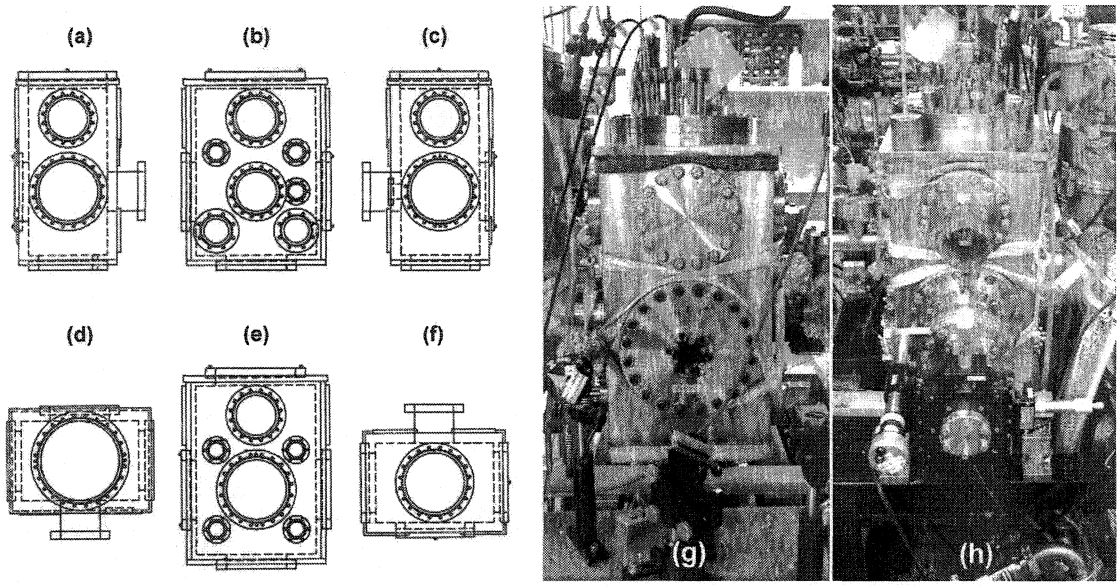

Fig. 2.6. The detector chamber. *(a)-(f) Various chamber views. The molecular beam propagation direction is noted in parentheses hereafter. (a) Laser input side (left to right). (b) Downstream side (out of page). (c) Mirror mount side (right to left). (d) Top view; spectrometer mounting flange (top to bottom). (e) Gate valve side (into page). (f) Bottom view; turbomolecular pump mounting flange (bottom to top). (g) View equivalent to (a). The laser beam is reflected through 90° by a mirror (bottom) before entering through the chamber's window (just below centre). The spectrometer and detector (mounted atop the spectrometer) are suspended within the chamber from the feedthrough flange at top. (h) View equivalent to (c). The turbomolecular pump and roughing lines (bottom), parabolic mirror translator (just below centre), spectrometer mounting flange (top) and intermediate chamber (right) are also shown.*

diameter, 2 mm thick) while the parabolic mirror's XYZ positioning stage is mounted to the second. The chamber's silver-coated 1 inch diameter, 50 mm focal length parabolic mirror and piezoelectric slit are described in subsequent sections. The time-of-flight mass spectrometer and ion detector are suspended from the chamber's 10" ConFlat top flange. The 8" and 10" flanges are each fitted with a pair of steel pins to ensure the precise alignment of mating flanges with the chamber's design axes. The chamber is also equipped with five 6" ConFlat, two 4.5" ConFlat, and seven 2.75" ConFlat flanges, as well as a pair of halogen bake-out lamps fastened to its floor. As in the intermediate chamber, the pressure is measured using Bayard-Alpert ionization and thermocouple gauges. The chamber's bake-out temperature is limited by the Viton O-ring used to seal the laser input window, Kapton-insulated wiring associated with the mass spectrometer

and piezoelectric slit, and the ultrahigh vacuum-compatible epoxy used to bond the piezoelectric crystal stack to the slit assembly.

Vacuum System Interlocks

A system of vacuum interlocks has been incorporated into the PATRICK instrument to protect its critical components in the event of various subsystem failures. One of three analogue interlock circuits is dedicated to each chamber (Fig. 2.7). Each circuit can be configured either to operate independently or to sense error conditions in its counterparts.

Each chamber's interlock circuit consists of a primary and a secondary loop. Primary loops monitor conditions that affect the start-up and safe operation of the diffusion and turbomolecular pumps. Secondary loops ensure that stable operation under high/ultrahigh vacuum conditions is maintained. Each loop consists of several relays connected in series. During normal operation, all relays are closed and current flows through each loop. Four criteria must be met to energize each primary loop:

(1) Electrical power must be supplied to its associated roughing pump(s). For the intermediate and detector circuits, this involves monitoring the status of the power bar to which the rotary pump is connected. For the source chamber, an integrated roots blower

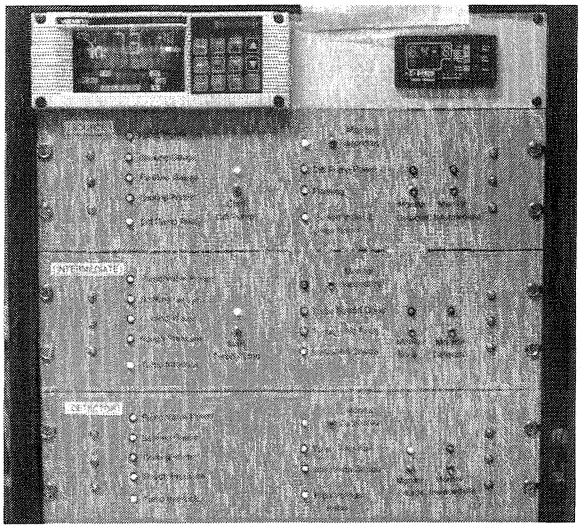

Fig. 2.7. Vacuum system interlock control panels. *Separate panels monitor each of the source (just above centre), intermediate (centre), and detector (bottom) chambers. Columns of LEDs (left) show the status of the relays within the primary loop of each circuit. Switches to enable each secondary loop are located above similar columns of secondary relay status indicators (centre). Additional switches (right) enable each circuit to monitor the status of the others. Also shown are the vacuum gauge readouts for the detector and source chambers (top right and top left, respectively).*

interlock is monitored which ensures that both the roots blower and its rotary pump are operating properly.

(2) The corresponding diffusion or turbomolecular pump's backing pressure must be below a specified threshold value. In each case, this involves monitoring a thermocouple pressure gauge.

(3) The pressure at the mouth of the corresponding diffusion or turbomolecular pump must be sufficient to allow it to be started. This involves monitoring the intrachamber analogue convection transducer (source chamber) and thermocouple gauges (intermediate and detector chambers).

(4) The flow of cooling water to the corresponding diffusion or turbomolecular pump must be adequate. This is determined by monitoring flow switches located in each pump's cooling water line.

Current flow within a circuit's primary loop closes a relay within the corresponding secondary loop and allows the associated diffusion or turbomolecular pump to be started. Once stable high or ultrahigh vacuum has been achieved in a chamber, throwing a switch on its interlock panel activates its secondary loop. The secondary loop ensures that the following conditions are maintained:

(1) The corresponding diffusion or turbomolecular pump must be operating. In the case of the diffusion pump, a current sensor is monitored to ensure that it is receiving power. Normal operation of the turbomolecular pumps is verified by monitoring relay outputs associated with their individual controllers.

(2) The pressure in the corresponding chamber must not exceed a specified threshold value in the high/ultrahigh vacuum regime. This is determined by monitoring the inverted

magnetron (source chamber) and Bayard-Alpert ionization gauges (intermediate and detector chambers).

When stable high/ultrahigh vacuum operation has been established in a chamber and its secondary loop has been activated, additional components may be powered on. These include the oven heating elements and the pulsed valve power supply (source chamber) as well as the time-of-flight spectrometer and ion detector high voltage supplies (detector chamber).

A subsystem failure causes a particular relay to open and results in the shutdown of various components. An error condition in the source chamber circuit triggers the shutdown of the diffusion pump as well as the oven or pulsed valve power supplies (if applicable). An intermediate chamber failure will cause its turbomolecular pump to be shut down. A fault in the detector chamber circuit will remove high voltages from the time-of-flight spectrometer and ion detector. The detector chamber's turbomolecular pump is internally protected against high input pressures and will automatically power down in such an instance. When an error condition occurs in a chamber monitored by another, both chambers shut down. Each ultrahigh vacuum gauge is configured to turn off automatically when its chamber pressure exceeds the safe operating threshold.

2.3 Molecular Beam

Molecular beams are routinely employed in laser-based studies of molecules since they can produce well-collimated gas-phase targets that are rotationally (and to a lesser extent, vibrationally) cold [Sco1988]. The PATRICK instrument produces a highly collimated beam with an effective transverse translational temperature of ~1 μK. This property enables our performance of high-resolution time-of-flight mass spectrometry since it represents a negligible spread of initial velocities along the spectrometer axis.

The PATRICK instrument produces an ultrathin ribbon-like molecular beam whose thickness can be readily adjusted. This capability is believed to be unique in studies of laser-molecule interactions. To date, molecular beams as thin as ~40 μm (roughly half the thickness of a human hair) have been produced.

The ultrathin nature of the PATRICK instrument's molecular beam provides two key benefits for high intensity laser experiments such as time-resolved Coulomb explosion imaging. First, molecules can be confined almost entirely to the highest intensity region of a tight laser focus. This can significantly reduce the quantity of ions produced at lower intensities that often represent unwanted background in such studies. Second, in conjunction with a tight laser focus, an ultrathin molecular beam yields an extremely small laser-molecule interaction volume that facilitates experiments on single gas-phase molecules. At a laser wavelength of 800 nm, interaction volumes as small as ~125 μm^3 can be achieved.

Molecular Beam Production

The components used to produce and collimate the molecular beam are shown schematically in Fig. 2.8. One of three interchangeable gas reservoirs (a continuous beam source, a pulsed valve, and an oven source) equipped with a replaceable nozzle is mounted within the source chamber and supplied by an external gas manifold. Gas emerging from the nozzle into the vacuum of the source chamber expands to form a molecular jet that impinges upon the first of

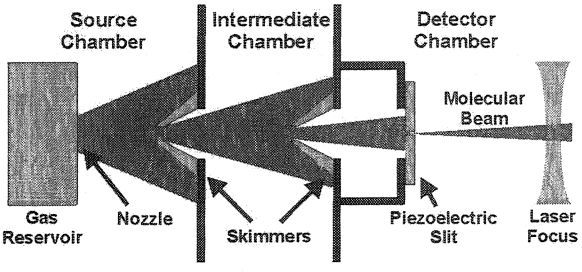

Fig. 2.8. Molecular beam collimation components. *Gas from a reservoir expands through a small nozzle into the high vacuum of the source chamber. Skimmers mounted in the source and intermediate chambers select the central portion of the molecular jet. The detector chamber's piezoelectric slit provides final collimation. The resulting molecular beam is a highly collimated ribbon of gas with a minimum thickness of ~40 μm in the laser focus.*

two 1 mm-diameter skimmers. The reservoir is mounted to the wall that separates the source and intermediate chambers using a system of three mounting rods, spacers, and a translatable "spider" mounting disc. This arrangement permits the adjustment of the nozzle-skimmer separation while ensuring that the reservoir's centre line remains coincident with a design axis of the apparatus. The source chamber's skimmer is affixed to a copper heater assembly that is thermally isolated from the chamber wall by a ceramic disc and contains two Kapton-insulated flexible ribbon heaters (Omegalux model KHLV-0502/10). Heating the skimmer reduces condensation of incident jet molecules (when required) and inhibits clogging during oven operation. The second skimmer is affixed to the translatable portion of the gate valve that separates the intermediate and detector chambers. Both skimmer mounts are designed to permit some freedom of positioning during aperture alignment. Final collimation of the molecular beam is performed by a piezoelectric slit affixed to a mounting plate assembly that can travel along four rods attached to the detector chamber wall. This arrangement preserves the slit's orientation and keeps the mounting plate assembly centred about a design axis of the apparatus during translation.

Continuous Beam Reservoir

The gas reservoir used to produce a continuous molecular beam is constructed of welded stainless steel (Fig. 2.9). The reservoir's body (a 0.5" O.D. tee) is small to facilitate evacuation and connects to an external gas manifold via the VCR fitting and a flexible bellows. The mount plate couples to the translatable spider used to position the reservoir accurately relative to the source chamber skimmer. The nozzle consists of a replaceable stainless steel foil pinhole (Melles Griot series 04PHP, unpainted) sealed to the mount plate via the pinhole clamp and a Viton O-ring. An O-ring-sealed 1" diameter window is mounted upstream from the nozzle and permits an alignment laser beam to pass through the reservoir.

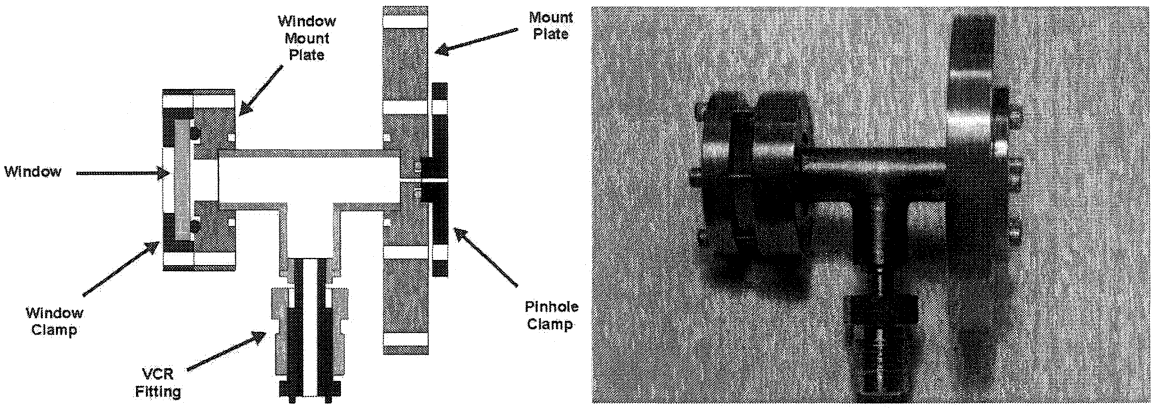

Fig. 2.9. Continuous beam gas reservoir. *Gas is supplied to the reservoir via the VCR fitting and escapes through the O-ring-sealed pinhole. The reservoir's mount plate couples to the same translatable spider used to mount the pulsed valve reservoir. The O-ring-sealed window behind the nozzle enables an alignment laser beam to traverse the reservoir.*

Pulsed Valve Reservoir

The translatable reservoir mounting system is also compatible with a pre-existing pulsed valve design (Fig. 2.10). The valve is constructed of stainless steel except where otherwise noted. Viton O-ring seals couple the valve body, front plate, and nozzle plate to form the gas reservoir. Gas from the external manifold is supplied to the valve via the intrachamber bellows and VCR fittings. The nozzle consists of a stainless steel foil pinhole permanently affixed to the nozzle plate's interior surface with a high vacuum-compatible epoxy (TorrSeal). Mounted to the front plate inside the valve, is a piezoelectric disc (Physik Instrumente model P-286.20) that supports a threaded stainless steel or brass plunger. In the valve's "closed" position, a small O-ring mounted at the end of the plunger is compressed against the nozzle plate, preventing the escape of gas.

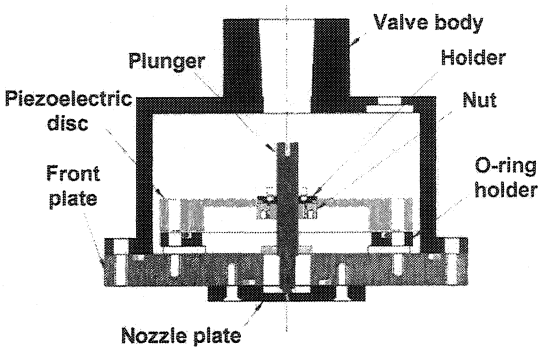

Fig. 2.10. Pulsed valve reservoir. *Gas from the external manifold is supplied to the reservoir via the fitting at top. The nozzle consists of a foil pinhole sealed by a small O-ring attached to the plunger. The application of a high voltage pulse to the piezoelectric disc draws back the plunger, emitting a ~100 μs burst of gas into the source chamber. High voltage is supplied to the piezoelectric disc via a feedthrough at top right. Viton O-rings seal the front plate to the valve body and nozzle plate.*

The application of a high voltage (~1700 V) pulse to the piezoelectric disc causes its centre to deflect upward, pulling the plunger back from the nozzle plate. This breaks the O-ring seal around the nozzle and a brief pulse issues from the valve. The plunger's tension must be carefully adjusted in accordance with the high voltage pulse to achieve the shortest valve opening time (~100 μs). Improper adjustment can cause the plunger to bounce after opening and thereby produce a second gas pulse. The maximum repetition rate at which the valve can be operated is limited to ~100 Hz by the mechanical resonance frequency of the disc-plunger-O-ring assembly as well as the high voltage pulse characteristics. Since this is less than the maximum repetition rate of the Ti:sapphire regenerative amplifier (500 Hz), our experiments are typically performed using the continuous beam source instead.

Oven Reservoir

An oven source with a maximum design temperature of 900 K is available for evaporation of solid samples (Fig. 2.11). The oven consists of a main chamber and a smaller, detachable nozzle section. A flexible Inconel-sheathed heating element (Thermocoax models SEI 15/100-100/2 CP15 (main) and SEI 15/100-100/2 CP15 (nozzle)) resides in the helical groove of each section's exterior and is held in place by a cylindrical sleeve of formed steel shim stock. A slightly larger coaxial steel sleeve serves as a radiation shield for each section. The main chamber's rear flange (a modified 1.33" ConFlat) is also shielded and can be removed for sample loading. The nozzle chamber extends outward from a 1.33" ConFlat flange and couples to the front of the main section via a copper gasket. A nozzle holder made from nickel-plated copper mounts to the front of the small chamber and compresses a removable stainless steel foil pinhole between its halves. A Pyrex rod mounted behind the main chamber and coaxial with the nozzle allows an alignment laser beam to pass through the entire length of the oven.

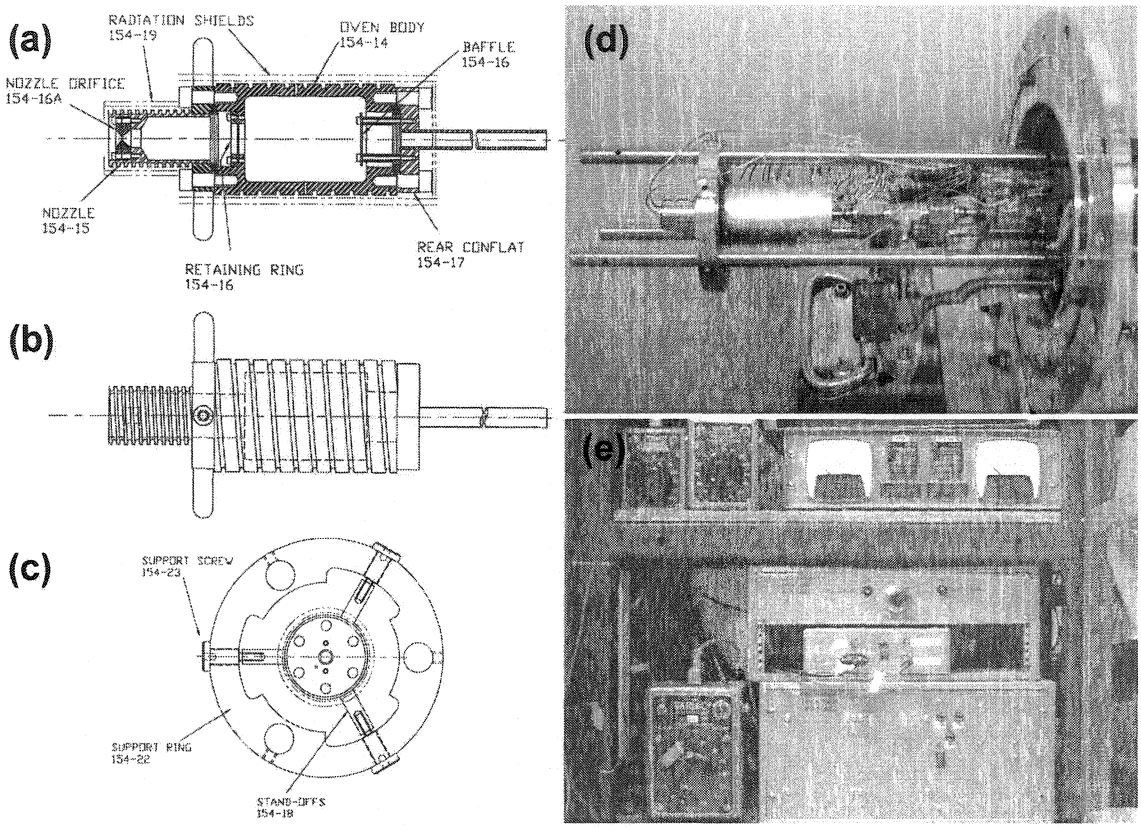

Fig. 2.11. Oven reservoir. *(a) Preheated buffer gas enters through the tube at right in this cross-sectional view. The baffle directs the gas over a sample boat (not shown) at the bottom of the main chamber. The buffered sample gas then enters the smaller chamber via a steel grid before exiting through the nozzle at left. (b) Exterior view of oven with radiation shields removed showing the two helical grooves that accommodate the oven's heater coils. (c) Axial view of oven showing its mounting pins and translatable spider. (d) Photograph of oven with radiation shields in place. The teed buffer gas supply network is directly behind the oven (right). Buffer gas enters through the bellows at the bottom of tee. To the right of the tee is a Pyrex rod that enables an alignment laser beam to be passed through the oven. The three mounting rods upon which the spider travels are also shown. (e) Photograph of oven temperature control electronics.*

The oven assembly is fixed to a translatable spider (Fig. 2.11c) that travels on three support rods affixed to the chamber's rear flange (Fig. 2.11d). The skimmer flange's three alignment pins key into recesses in the ends of the support rods, providing additional support and ensuring that the oven's axis coincides with those of the other molecular beam apertures.

During operation, a buffer gas is flowed from the external gas manifold into the oven's main section via a stainless steel bellows (heated by an Omegalux model KHLV-0502/10 element mounted in a copper heater assembly and monitored by a thermocouple) and the rear oven flange.

A D-shaped baffle directs the pre-heated incoming gas over the solid sample located at the bottom of the main section. The evaporated sample and buffer gas then enter the oven's second chamber (which is kept hotter than the main section to inhibit clogging) before exiting the nozzle. A wire grid secured by a retaining ring prevents solid particles from being swept into the second chamber.

The oven's temperature control electronics are shown in Fig. 2.11e. The temperature of each chamber is monitored by a stainless steel-sheathed type K thermocouple (Thermocoax model 2AB I10/1m/TI10/MF9 with extension 2AB25.DIN/5m) and regulated independently. The output of each thermocouple is passed to a PID temperature controller (Omega model CN76163-PV) and also read out by a panel display. Each controller maintains its set-point temperature by intermittently opening an external solid-state relay (Omega model SSR240DC25) to interrupt the supply of current to its respective heating element. A dedicated ammeter monitors the instantaneous current supplied to each loop by its Variac/transformer pair. The maximum ratings are 5A (14 V) and 7.1 A (39.3 V) for the main and nozzle heating circuits, respectively.

Piezoelectric Slit

The piezoelectric slit (Piezosystem Jena model PZS 1NV O-101-51, UHV-compatible option with model 12V40 power supply), its translatable mounting plate assembly, and four alignment rods are shown in Fig. 2.12. The slit's 22 mm-long stainless steel edges move symmetrically when a voltage (-10 V to 150 V) is applied to the single piezoelectric crystal stack. The voltage dependence of the slit's width d_s was calibrated in air using a microscope. The slit's room temperature response as a function of monitor voltage (which is a factor of 10 less than the actual applied voltage) and its parameterization are depicted in Fig. 2.13. The slit is normally closed (-0.1 V), has a maximum separation of ~250 μm (15 V), and exhibits significant hysteresis. For optimal reproducibility, the slit should be opened fully before reducing the

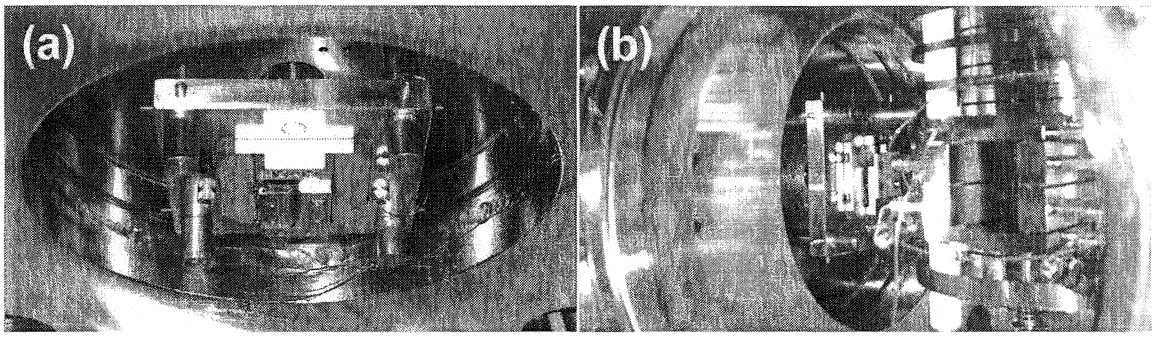

Fig. 2.12. Piezoelectric slit. *(a) Top view of the slit, its mounting plate, and four mounting rods. The dark semicircle at top is the partially obscured backside of the intermediate chamber skimmer. The molecular beam enters the detector chamber through the skimmer prior to being collimated by the slit. (b) Side view of the slit assembly. The laser beam input side of the time-of-flight mass spectrometer is also shown at right.*

voltage to achieve the desired width. Thereafter, the slit should be fully closed and reopened before resetting the width.

The piezoelectric slit's adjustable nature is of great practical benefit. For single molecule experiments (and those in which molecules are confined to the highest intensity region of the laser focus), narrow slit widths are required to achieve ultrathin molecular beams. In the PATRICK instrument, a 100 μm-diameter nozzle and a 29 μm slit separation produce a molecular beam that is just ~40 μm wide. Overlapping a tight *f*/2 laser focus with such an ultrathin beam at the outset of an experiment can be quite time-consuming. In such a case, opening the slit fully increases the molecular beam width by roughly an order of magnitude and

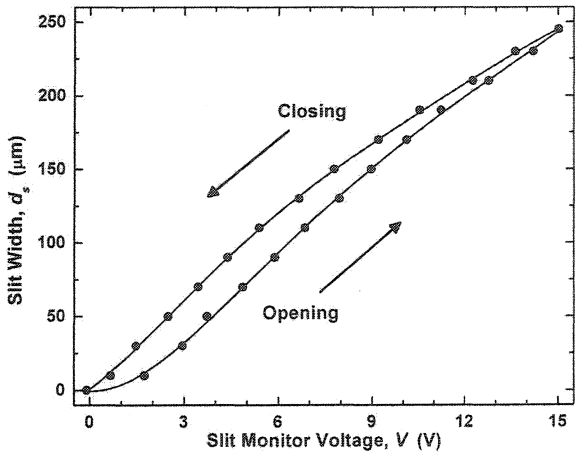

Fig. 2.13. Piezoelectric slit calibration curve. *The dependence of the piezoelectric slit width d_s on monitor voltage V is shown. The monitor voltage is a factor of 10 less than the actual voltage applied to the slit. Since the slit exhibits significant hysteresis, it should be fully opened or closed before setting its width. The respective lower and upper data were obtained while opening and closing the slit. The parameterized slit width is given by $d_s = -0.63006 - 0.37563V + 5.2879V^2 - 0.58477V^3 + 0.02766V^4 - 4.8232\times10^{-4}V^5$ (opening) and $d_s = 0.72430 + 16.151V + 2.4152V^2 - 0.04519V^3 + 0.03000V^4 - 7.0465\times10^{-4}V^5$ (closing).*

greatly expedites the overlap procedure. Thereafter, re-optimizing its overlap with successively narrower molecular beams will refine the focal spot's position. Finally, while to date only static voltages have been applied to the piezoelectric slit, it is possible to modulate the slit's width periodically using a time-dependent voltage. For instance, experiments can be conducted during which the slit (resonance frequency 450 Hz) is closed upon the arrival of every second laser pulse. Such an arrangement would permit the measurement of extraneous signals that originate from background gas to be interleaved with the measurement of interest.

Alignment of Molecular Beam Apertures

To achieve optimal molecular beam density and cooling in the laser-molecule interaction region, the axes of all beam apertures (Fig. 2.8) must coincide. The translatable spiders upon which the gas reservoir and piezoelectric slit are mounted remain precisely centred along a design axis of the apparatus. However, this is insufficient to ensure that the actual nozzle and slit themselves are centred. In the case of the nozzle, the commercially obtained pinhole may not be centred on its foil disc. Furthermore, each reservoir's nozzle mounting recess is slightly larger than the discs themselves. Similarly, the piezoelectric slit is not necessarily centred upon its commercially supplied substrate that in turn is somewhat smaller than its mounting plate assembly. As a result, some initial manual alignment of the molecular beam apertures was required. Aperture realignment must be performed whenever the nozzle is replaced.

Directing a laser beam along the intended molecular beam axis enables the alignment of its apertures. Windows mounted on the source chamber's upstream flange and the detector chamber's downstream flange permit the alignment laser beam to traverse the entire apparatus. Similarly, windows integrated into the continuous beam and oven gas reservoirs (upstream from their nozzles) also allow the passage of an alignment laser beam. The pulsed valve's plunger precludes the passage of a laser beam through it.

Diffraction of the alignment beam by the first narrow beam-limiting aperture (either the nozzle or the slit, depending on the laser propagation direction) produces a large, diffuse laser spot or fringe at the second limiting aperture and complicates the alignment process. Passing the laser beam through the wider of the limiting apertures first mitigates the effect of diffraction. Typically, the fully opened slit (~250 μm maximum width) will be the wider aperture, hence the laser beam should propagate through the slit, the skimmers, and finally the nozzle.

Modelling of the Molecular Beam

The molecular beam density in the laser-molecule interaction region has been modelled based on geometric considerations. The molecular beam is profiled as a function of displacement y from the molecular beam axis along the laser propagation axis (Fig. 2.14). Since the slit's width subtends a very small angle (i.e., less than 0.001°) with respect to the nozzle, the density of incoming molecules is essentially uniform across the slit. As a result, the beam density in the interaction region is simply proportional to the fraction of the nozzle from which molecules can pass unobstructed through the slit to the point of measurement.

Slit Operating Regimes

Inherent to the model is the concept of "critical slit width" d_s^{crit} i.e., the minimum width of the slit d_s for which the entire nozzle contributes to the on-axis beam density $\rho(y=0)$. The critical slit width represents the transition between the "underfilled" ($d_s > d_s^{crit}$) and "overfilled"

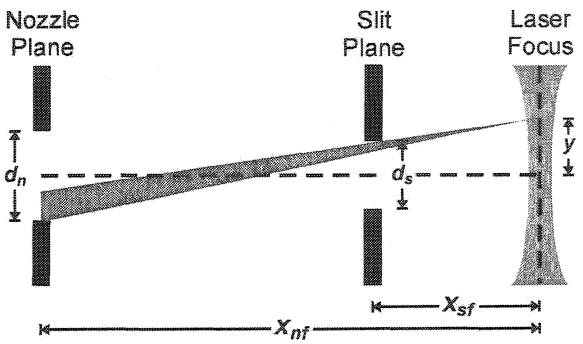

Fig. 2.14. Molecular beam parameter definitions. *The dimensions used in the geometric model of the molecular beam are shown, namely: the nozzle width d_n, the slit width d_s, the distance y of the observation point from the molecular beam axis, and the distances from the laser focus of the nozzle and slit planes (x_{nf} and x_{sf}, respectively).*

($d_s < d_s^{crit}$) operating regimes of the piezoelectric slit and is given by $d_s^{crit} = \frac{x_{sf}}{x_{nf}} d_n$ where x_{sf} and x_{nf} are the respective distances of the slit and nozzle from the laser focus and d_n is the width of the nozzle (Fig. 2.14). The variation of the relative molecular beam density $\rho(y)$ along the laser propagation axis can be qualitatively understood in each regime by tracing rays from points on the nozzle through the slit to an observation position $y = y'$ as follows.

In the underfilled slit regime ($d_s > d_s^{crit}$), the slit width is sufficient to permit the entire nozzle to contribute to the molecular beam not just on-axis (Fig. 2.15a) but also over a range of off-axis positions up to $y = y_{knee}$ (Fig. 2.15c). In the intervening "plateau" region $0 < y < y_{knee}$ (Fig. 2.15b), the beam density is a maximum $\rho(y) = 1$. Within the "vignetted" region $y_{knee} < y < y_{cut}$ (Fig. 2.15d), the area of the nozzle that contributes to the molecular beam is limited by the slit. Consequently, the vignetted beam density decreases monotonically with y. At $y = y_{cut}$ (Fig. 2.15e) and beyond, the beam density is zero since molecules from the nozzle are completely blocked by the slit's edge.

In the overfilled slit regime ($d_s < d_s^{crit}$), the slit permits only a fraction of the total nozzle area to contribute to the molecular beam on-axis (Fig. 2.15f), hence $\rho(0) < 1$. In analogy with the underfilled regime, a plateau region $0 < y < y_{knee}$ exists over which the contributing fractional area shifts from the centre of the nozzle towards its edge (Fig. 2.15g). At $y = y_{knee}$ (Fig. 2.15h), the contributing area reaches the side of the nozzle and additional vignetting by the slit edge begins. The fraction of the nozzle that contributes to the molecular beam (and hence the beam density) decreases with y over the vignetted region $y_{knee} < y < y_{cut}$ (Fig. 2.15i). As in the underfilled regime, the beam density is zero for $y \geq y_{cut}$ (Fig. 2.15j).

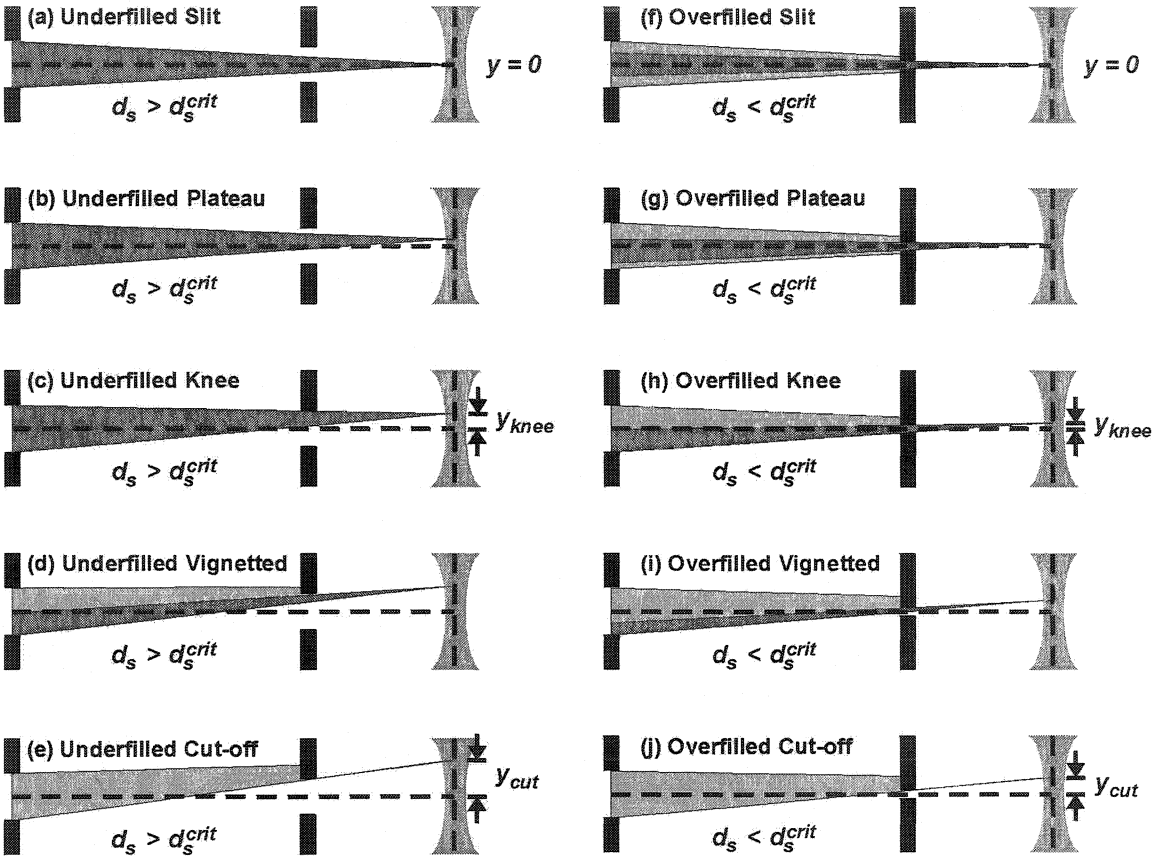

Fig. 2.15. Partial nozzle contributions to the molecular beam. *Depicted are the portions of the nozzle that contribute to the molecular beam at various observation points y within the underfilled (a)-(e) and overfilled (f)-(j) slit operating regimes. In each case, the heavily shaded portion contributes at y while the lightly shaded portion is blocked by the slit. The selected observation points are on-axis (a) and (f), within the plateau regions (b) and (g), at $y = y_{knee}$ (c) and (h), within the vignetted regions (d) and (i), and at $y = y_{cut}$ (e) and (j).*

Effect of Nozzle Shape

While both slit regimes are characterized by plateau and vignetted regions, the molecular beam density profile $\rho(y)$ within each region is determined by nozzle shape. Expressions for rectangular (where d_n represents nozzle width along y) and circular (where d_n represents nozzle diameter) nozzles are listed in Tables 2.1 and 2.2, respectively. Note that y_{knee} and y_{cut} are independent of nozzle shape and that y_{cut} is identical for both slit regimes. Molecular beam

profiles for $d_n = 100\ \mu m$ rectangular (dashed lines) and circular (solid lines) nozzles and a critical slit width of $d_s^{crit} = 29\ \mu m$ are plotted in Fig. 2.16 for several slit widths d_s.

A rectangular nozzle produces a trapezoidal beam density profile with a plateau region whose width is proportional to $\left|d_s - d_s^{crit}\right|$ (Table 2.1, Fig. 2.16). For $d_s = d_s^{crit}$, the width of the plateau region is zero and consequently the beam profile is triangular. The on-axis beam density $\rho(0)$ is equal to unity in the underfilled regime and d_s/d_s^{crit} in the overfilled regime. In both cases, the beam density varies linearly with y in the vignetted region with slope $\frac{\partial \rho}{\partial y} = \frac{1}{d_n} - \frac{1}{d_s^{crit}}$.

The beam density profile for a circular nozzle is more complicated (Table 2.2, Fig. 2.16) since the nozzle's height varies along its width. In the underfilled slit regime ($d_s < d_s^{crit}$), the beam density profile within the plateau region is independent of nozzle shape but the vignetted region's profile is not (Table 2.2). This is apparent in Fig. 2.16 for $d_s > 29\ \mu m$ where the trend is

Table 2.1: Model Results for Rectangular Nozzles

	Overfilled Slit $d_s < d_s^{crit}$	**Underfilled Slit** $d_s > d_s^{crit}$
Knee	$y_{knee} = \frac{d_n}{2}\left(\frac{d_s^{crit} - d_s}{d_n - d_s^{crit}}\right)$	$y_{cut} = \frac{d_n}{2}\left(\frac{d_s - d_s^{crit}}{d_n - d_s^{crit}}\right)$
Cut-off	$y_{cut} = \frac{d_n}{2}\left(\frac{d_s + d_s^{crit}}{d_n - d_s^{crit}}\right)$	$y_{cut} = \frac{d_n}{2}\left(\frac{d_s + d_s^{crit}}{d_n - d_s^{crit}}\right)$
On-axis Density	$\rho(0) = d_s/d_s^{crit}$	$\rho(0) = 1$
Off-axis Density	$\underline{For\ 0 \le y \le y_{knee}}$ $\rho(y) = \rho(0) = \frac{d_s}{d_s^{crit}}$ $\underline{For\ y_{knee} < y \le y_{cut}}$ $\rho(y) = \frac{1}{2}\left(\frac{d_s}{d_s^{crit}} + 1\right) + \left(\frac{1}{d_n} - \frac{1}{d_s^{crit}}\right)y$	$\underline{For\ 0 \le y \le y_{knee}}$ $\rho(y) = \rho(0) = 1$ $\underline{For\ y_{knee} < y \le y_{cut}}$ $\rho(y) = \frac{1}{2}\left(\frac{d_s}{d_s^{crit}} + 1\right) + \left(\frac{1}{d_n} - \frac{1}{d_s^{crit}}\right)y$
FWHM	$\Delta y = \frac{d_n d_s^{crit}}{d_n - d_s^{crit}}$	$\Delta y = \frac{d_n d_s}{d_n - d_s^{crit}}$

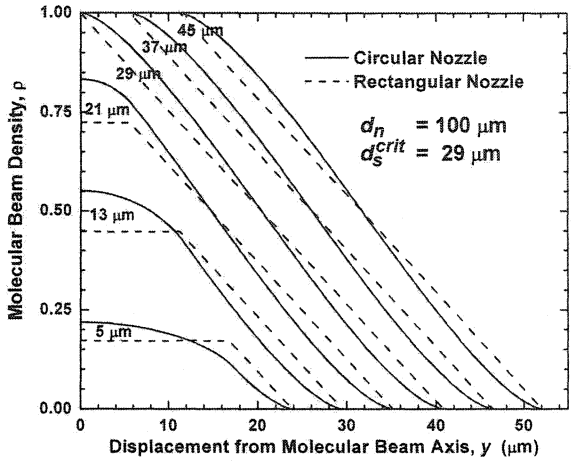

Fig. 2.16. Predicted molecular beam density profiles. *The predicted molecular beam density ρ as a function of off-axis distance y is depicted for both circular (solid lines) and rectangular (dashed lines) nozzles. Each profile is labelled by the slit width d_s used to calculate it. The nozzle and critical slit widths used (d_n = 100 μm and d_s^{crit} = 29 μm) correspond to the PATRICK instrument's actual values.*

linear for the rectangular nozzle and approximately sigmoidal for the circular one. This nozzle shape dependence can be understood via Fig. 2.17 in which circular and rectangular nozzles of

Table 2.2: Model Results for Circular Nozzles

	Overfilled Slit $d_s < d_s^{crit}$	**Underfilled Slit** $d_s > d_s^{crit}$
Knee	$y_{knee} = \frac{d_n}{2}\left(\frac{d_s^{crit} - d_s}{d_n - d_s^{crit}}\right)$	$y_{knee} = \frac{d_n}{2}\left(\frac{d_s - d_s^{crit}}{d_n - d_s^{crit}}\right)$
Cut-off	$y_{cut} = \frac{d_n}{2}\left(\frac{d_s + d_s^{crit}}{d_n - d_s^{crit}}\right)$	$y_{cut} = \frac{d_n}{2}\left(\frac{d_s + d_s^{crit}}{d_n - d_s^{crit}}\right)$
Definitions of σ & δ	$\sigma \equiv \frac{d_s}{d_s^{crit}} + 2\left(\frac{1}{d_n} - \frac{1}{d_s^{crit}}\right)y$ $\delta \equiv \frac{d_s}{d_s^{crit}} - 2\left(\frac{1}{d_n} - \frac{1}{d_s^{crit}}\right)y$	$\sigma \equiv \frac{d_s}{d_s^{crit}} + 2\left(\frac{1}{d_n} - \frac{1}{d_s^{crit}}\right)y$ $\delta \equiv \frac{d_s}{d_s^{crit}} - 2\left(\frac{1}{d_n} - \frac{1}{d_s^{crit}}\right)y$
On-axis Density	$\rho(0) = \frac{2}{\pi}\left[\frac{d_s}{d_s^{crit}}\sqrt{1-\left(\frac{d_s}{d_s^{crit}}\right)^2} + \sin^{-1}\left(\frac{d_s}{d_s^{crit}}\right)\right]$	$\rho(0) = 1$
Off-axis Density	*For* $0 \le y \le y_{knee}$ $\rho(y) = \frac{1}{\pi}\left[\sigma\sqrt{1-\sigma^2} + \sin^{-1}\sigma + \delta\sqrt{1-\delta^2} + \sin^{-1}\delta\right]$ *For* $y_{knee} < y \le y_{cut}$ $\rho(y) = \frac{1}{\pi}\left[\sigma\sqrt{1-\sigma^2} + \sin^{-1}\sigma\right] + \frac{1}{2}$	*For* $0 \le y \le y_{knee}$ $\rho(y) = 1$ *For* $y_{knee} < y \le y_{cut}$ $\rho(y) = \frac{1}{\pi}\left[\sigma\sqrt{1-\sigma^2} + \sin^{-1}\sigma\right] + \frac{1}{2}$

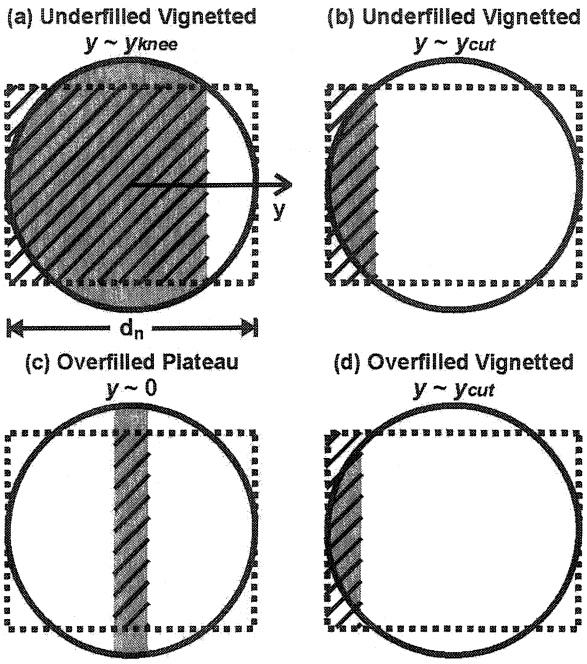

Fig. 2.17. Nozzle geometries. *The outlines of circular (solid line) and rectangular (dotted line) nozzles of widths d_n and equal areas are shown in each panel. The shaded and hatched areas indicate the respective portions of the circular and rectangular nozzles that contribute to the molecular beam at a given observation point y. The beam density at y is directly proportional to the contributing area of a nozzle. Consequently, the circular nozzle yields a higher beam density near $y = y_{knee}$ in the vignetted region of the underfilled slit regime (a) and also near the axis in the overfilled slit regime (c). Conversely, the rectangular nozzle always makes the larger contribution near $y = y_{cut}$ (b) and (d).*

equal areas and widths d_n are depicted. As noted above, the molecular beam density $\rho(y)$ is proportional to the area of the nozzle from which a ray can be traced through the slit to the measurement position y. The contributing nozzle areas for two values of y in the vignetted region ($y_{knee} < y < y_{cut}$) of the underfilled slit regime ($d_s > d_s^{crit}$) are shown in Figs. 2.17a and 2.17b. For $y \approx y_{knee}$ (Fig. 2.17a), the circular nozzle produces a higher beam density since its contributing area (shaded region) exceeds that of the rectangular nozzle (hatched area). At $y = \frac{d_n d_s}{2\left(d_n - d_s^{crit}\right)}$, exactly half of each nozzle contributes thus $\rho = 0.5$, irrespective of nozzle shape. For $y \approx y_{cut}$ (Fig. 2.17b), the circular nozzle makes the smaller contribution. The beam density profile produced by the circular nozzle in the overfilled slit regime ($d_s < d_s^{crit} = 29\,\mu\text{m}$ in Fig. 2.16) can be understood using the same approach. As Fig. 2.17c suggests, the circular nozzle produces a higher beam density both on-axis and over a range of y-values within the plateau region ($0 < y < y_{knee}$). In contrast to the rectangular nozzle case, the contributing height (and hence the contributing area) of the circular nozzle decreases as $y \to y_{knee}$. The relative circular

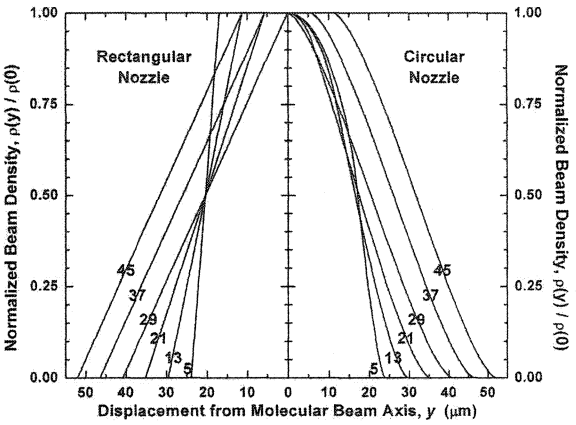

Fig. 2.18. Normalized predicted molecular beam density profiles. *Shown are the predicted beam density profiles of Fig. 2.16 normalized to their respective on-axis densities ρ(0). Results for rectangular nozzles are plotted at left; circular nozzle results are shown at right. Each profile is labelled by the slit width d_s (in μm) used to calculate it. For the rectangular nozzle, the profile FWHM decreases with d_s according to $\Delta y = d_n d_s / (d_n - d_s^{crit})$ in the underfilled slit regime. However, the FWHM has a uniform value of $\Delta y = d_n d_s^{crit} / (d_n - d_s^{crit})$ in the overfilled regime. For the circular nozzle, the FWHM also decreases with d_s in the underfilled regime but is only approximately constant in the overfilled regime.*

and rectangular beam densities at $y = y_{knee}$ depend on the slit width d_s, however the circular nozzle always makes the lesser contribution for $y \approx y_{cut}$ (Fig. 2.17d).

To illustrate the variation of molecular beam width, the beam density profiles depicted in Fig. 2.16 are shown in Fig. 2.18 with their heights normalized. In the underfilled slit regime ($d_s < d_s^{crit} = 29\,\mu m$ in Fig. 2.18), the molecular beam's full width at half-maximum (FWHM) is independent of nozzle shape and proportional to the slit width according to $\Delta y = \frac{d_n d_s}{d_n - d_s^{crit}}$. In the overfilled slit regime ($d_s < d_s^{crit} = 29\,\mu m$ in Fig. 2.18), however, the molecular beam's FWHM is independent of the slit width and proportional to the width of the nozzle according to $\Delta y = \frac{d_n d_s^{crit}}{d_n - d_s^{crit}} = d_n \left(\frac{x_{nf}}{x_{sf}} - 1 \right)^{-1}$. This result is exact for a rectangular nozzle and approximate in the circular case (Fig. 2.18).

Measurement of Molecular Beam Width

Two methods were used to measure the minimum beam width produced using a 100 μm diameter circular nozzle. In each case, 50 fs laser pulses (35 μJ pulse energy, 800 nm

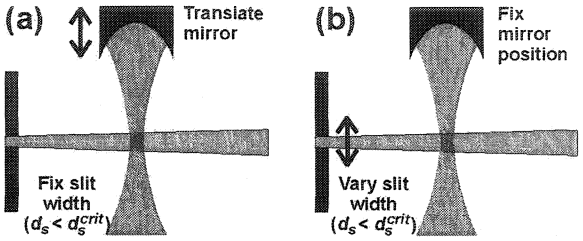

Fig. 2.19. Methods of molecular beam measurement. *Two techniques were used to determine the molecular beam width in the overfilled slit regime. (a) The ion yield for a fixed slit width was measured as the laser focus was scanned through the molecular beam. (b) The laser focus was positioned to coincide with the centre of the molecular beam. The ion yield was then measured as a function of slit width.*

wavelength) were focused using *f*/2 optics (10 μm confocal parameter) into a beam of xenon atoms within the time-of-flight mass spectrometer. Ions were detected with a microchannel plate pair and simple (non-imaging) anode and time-binned using a multichannel scaler (FAST ComTec GmbH model 7886A).

In the first approach (Fig. 2.19a), a narrow slit width ($d_s = 10\,\mu m$) was used to ensure that the measurement was conducted in the overfilled slit regime for which the molecular beam width is a minimum. The pressure in the continuous beam gas reservoir was 260 mbar (13 mbar Xe, balance He). The slit separation was held constant while the laser focus was scanned through the xenon beam by translating the intrachamber parabolic mirror. The resulting Xe^+ and Xe^{2+} yields as a function of mirror displacement y are depicted in Figs. 2.20a and 2.20b, respectively. Whereas the model predicts a 34 μm FWHM beam, widths of 106 μm FWHM for Xe^+ and 108 μm FWHM for Xe^{2+} are observed. To account for such a broad molecular beam, an effective source diameter of 300 μm must be input to the model. There are several aspects of the measurement that likely contribute to this discrepancy. First, the measured widths represent a convolution of the confocal parameter of the laser focus and the actual molecular beam width. Since the confocal parameter was roughly one-third of the expected molecular beam width, some broadening should be evident in the data. Second, the mirror is known to have been vibrating during the measurement and this should result in additional broadening. Finally, the observed

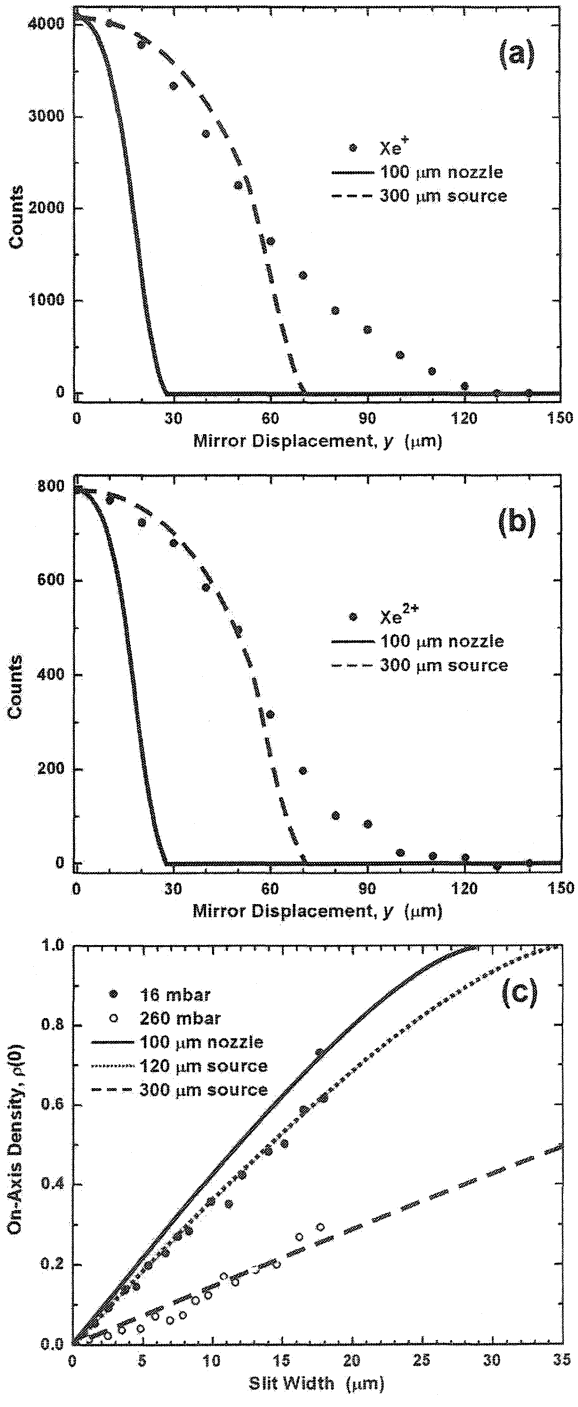

Fig. 2.20. Results of molecular beam measurement. *The Xe^+ and Xe^{2+} ion yields are depicted as a function of off-axis distance y in panels (a) and (b), respectively. The measured widths of 106 μm FWHM for Xe^+ and 108 μm FWHM for Xe^{2+} are consistent with an effective source width of 300 μm (dashed lines). A width of 108 μm FWHM was expected (solid lines). The reservoir pressure was 260 mbar. (c) The measured dependence of the Xe^{3+} ion yield as a function of slit width d_s is shown for reservoir pressures of 260 mbar (hollow circles) and 16 mbar (filled circles). The laser was focused into the centre of the molecular beam throughout the measurements. The predicted on-axis density profiles ρ(0) for the actual 100 μm diameter nozzle (solid line) are shown along with predictions for effective source sizes of 120 μm (dashed line) and 300 μm (dotted line). The results suggest that the analytical model is valid in the low-pressure limit, however the nozzle diameter d_n must be replaced by an empirically determined source size for high reservoir pressures.*

broadening may be due to a physical enlargement of the effective source diameter that depends upon the gas pressure behind the nozzle.

To address the above discrepancy, an alternate approach was used to determine the molecular beam width. During the second measurement (Fig. 2.19b), the mirror was positioned to achieve optimal overlap of the laser focus with the molecular beam. Thereafter, the mirror position was not changed. Instead, the on-axis beam density $\rho(0)$ (Table 2.2) was monitored as a function of slit width d_s. Since measurements were made in the overfilled slit regime $0 < d_s < d_s^{crit}$, the molecular beam width was essentially constant during the

measurement. This approach offers two advantages. First, the confocal parameter was largely irrelevant since the laser-molecule interaction volume was effectively held constant during the measurement. Second, mirror vibration would not affect the results since the mean mirror position remained constant. The normalized Xe^{3+} ion yields for gas reservoir pressures of 260 mbar (13 mbar Xe, balance He) and 16 mbar (pure Xe) are depicted in Fig. 2.20c. Also shown are the model's predictions for the actual 100 μm nozzle as well as effective source diameters of 120 μm and 300 μm. As in the first measurement, the result for a gas reservoir pressure of 260 mbar is consistent with an effective source diameter of 300 μm. The result for the lower (13 mbar) reservoir pressure, however, corresponds to a 120 μm effective source diameter, in good agreement with the actual nozzle diameter.

Therefore, the analytical model developed here can be applied to predict the spatial properties of ultrathin molecular beams accurately in the low-pressure limit. At higher reservoir pressures, the model should also prove useful provided that d_n is taken to be an empirically determined effective source size rather than the diameter of the actual nozzle.

2.4 Time-of-Flight Mass Spectrometer

The laser and molecular beams intersect within a high-resolution time-of-flight mass spectrometer. Ions produced in the laser-molecule interaction volume are accelerated towards the detector by the spectrometer's internal electric field.

In contrast to conventional Wiley-McLaren-type spectrometers that include both acceleration and field-free regions [Wil1955], the PATRICK instrument's spectrometer has no internal grids and employs a static, uniform field throughout. This single stage approach was adopted to prevent distortions in molecular images due to ion scattering from internal grids en route to the detector. Unlike multistage approaches, the spectrometer's design does not provide

space- or velocity-focusing of ions at the detector. However, these apparent drawbacks are generally negligible in the PATRICK instrument. Under typical experimental conditions (100 V/cm acceleration field, 2 μm focal spot diameter), the lack of space-focusing results in a ~100 ps (or less) distribution of arrival times for Xe^+ (and lighter ions). This uncertainty is a factor of ~5 less than the temporal resolution of the PATRICK instrument. Similarly, the tightly collimated molecular beam ensures that the lack of velocity-focusing yields a temporal uncertainty of ~50 ps for an effusive Xe beam.

The Electrode Stack

The time-of-flight mass spectrometer (Fig. 2.21) is cylindrical with an outer diameter of 140 mm, an inner diameter of 70 mm, and is effectively 240 mm in length. It consists of a stack of 17 nonmagnetic stainless steel ring electrodes (14 mm maximum thickness) separated by 11 mm-long alumina (Al_2O_3) spacers. The minimum separation between each pair of ring electrodes is 1.00 ± 0.01 mm. The electrode stack is held together by four steel support rods threaded into the top electrode. Each rod is insulated by a 255 mm-long alumina sleeve and has a threaded lower end featuring additional alumina spacers, a stainless steel spring, and two nuts. The spring prevents the breaking of the alumina spacers during electrode stack assembly and during chamber bake-out. A similar system of four additional alumina-insulated steel rods and alumina spacers is used to suspend (and electrically isolate) the electrode stack from the detector chamber's top (10" ConFlat) flange. While the ring electrodes are not identical, each has been designed to achieve a nearly homogeneous electric field within the spectrometer. The internal electric field structure was modelled using commercial software (SIMION) during the design and redesign phases of the spectrometer's development.

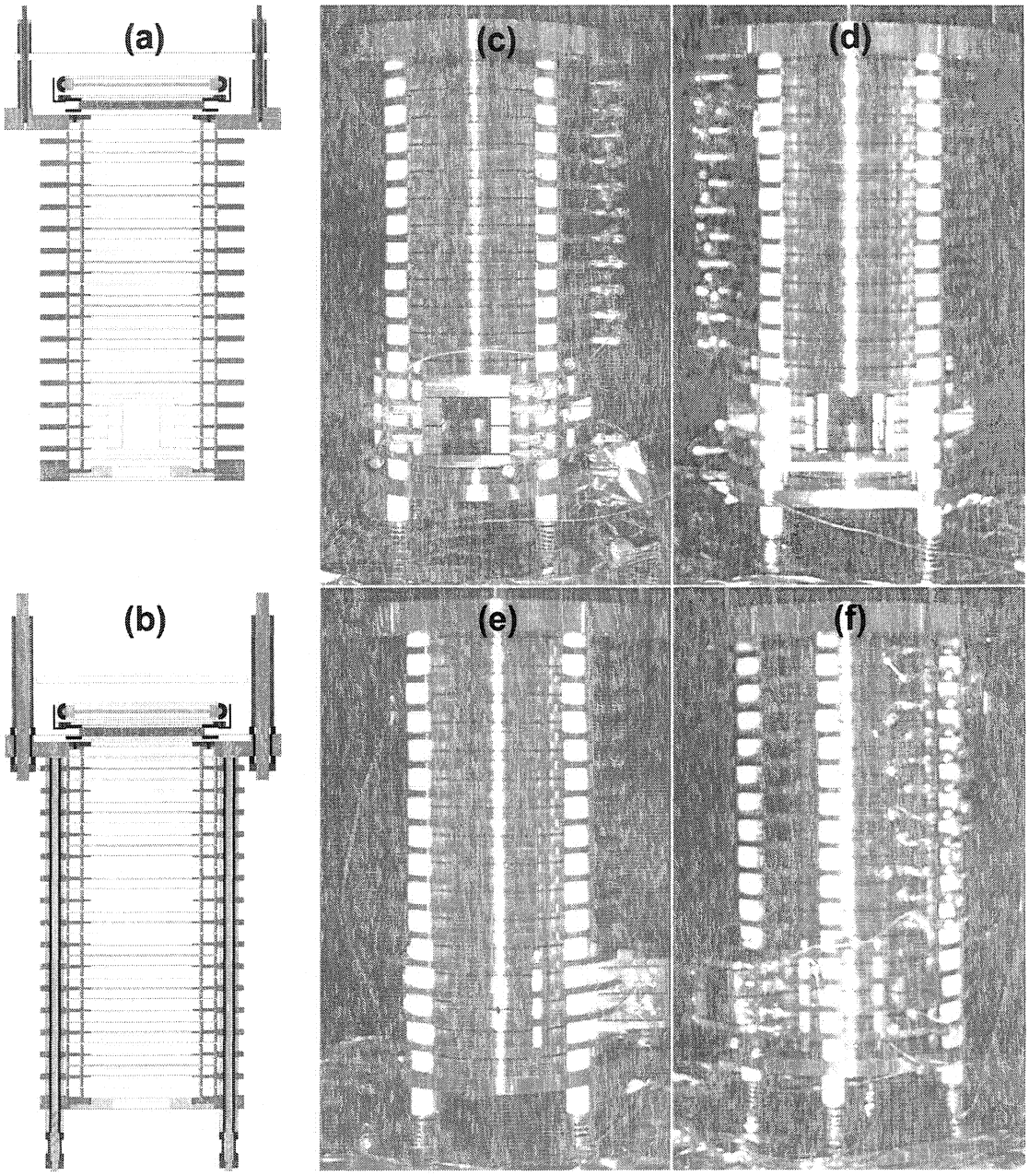

Geometries of Individual Electrodes

Both the top and bottom electrode rings incorporate removable steel grids. The grids inhibit external field penetration and provide essentially flat equipotential surfaces at either end of the spectrometer. The top grid does not appreciably distort molecular images since it is

Fig. 2.21. Time-of-flight mass spectrometer. *(a) Cross-sectional view of the spectrometer oriented as in (c). The cylindrical spectrometer is capped at each end by a steel grid and consists of 17 tiers of steel electrodes separated by precision alumina spacers (white areas in photographs). The delay line anode detector and its mounting assembly are shown at top. (b) Cross-sectional view of the spectrometer oriented as in (f). The electrode stack is suspended from the top electrode by four alumina-sleeved steel rods. Stack tension is maintained by a spring at the end of each rod that also prevents spacer breakage during bake-out. At top are the insulated support rods that suspend the entire spectrometer from the detector chamber's top flange. (c) Laser beam input side. The rectangular snout (lower middle) helps to maintain field uniformity within the spectrometer. (d) Mirror input side. The niche (lower middle) allows the parabolic mirror to be positioned within the electrode rings. (e) Molecular beam input side. The molecular beam enters through a 3 mm diameter hole (lower middle). (f) Rotated view. The laser beam enters at lower left. The molecular beam exit aperture is at lower right, amid the column of resistors used to bias the electrode stack.*

located but a few millimetres from the detector. The top electrode (190 mm outer diameter) is significantly larger than the rest in order to accommodate the two sets of support rods described above as well as the detector mounting assembly.

The eleven electrodes located directly beneath the top electrode are identical and cylindrically symmetric except for the four support rod clearance holes (Fig. 2.22a). A thin (1 mm) ledge projects inward from the centre of each electrode and defines an internal equipotential surface. In addition, each ring incorporates two concentric 14 mm thick guard rings to prevent external field penetration, and a pair of tapped holes to enable electrode biasing.

The four electrodes located directly above the bottom electrode form a subassembly designed to admit the collimated laser and molecular beams while maintaining the homogeneity of the spectrometer field (Fig. 2.22b-d). In the spectrometer's original embodiment, the four electrodes were identical to those of Fig. 2.22a except for four small (few mm diameter) holes that allowed the laser and molecular beams to enter and exit. While their small diameters ensured that the beam apertures would minimally degrade the internal field homogeneity, they required the use of an off-axis parabolic mirror to achieve tight (*f*/3) optical focusing. Unfortunately, off-axis parabolic reflectors are particularly sensitive to laser beam input angle and are physically incapable of producing high fidelity circularly polarized light within a laser focus. To address

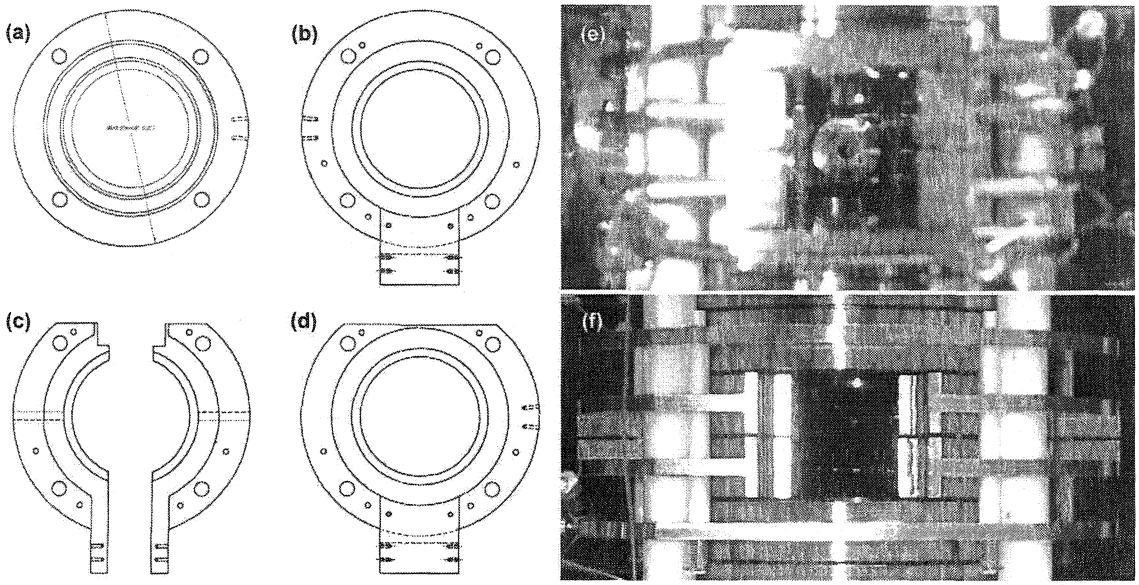

Fig. 2.22. Individual electrodes and spectrometer subassembly. *(a) Eleven of the spectrometer's 17 electrode tiers consist of specialized steel rings. Each ring has an internal diameter of 70 mm, an outer diameter of 140 mm, four 0.328" diameter holes to accommodate the steel support rods and their alumina sleeves, a concentric pair of 14 mm thick guard rings to prevent field penetration, and is separated from adjacent electrodes by 1 mm. (b)-(d) The spectrometer's subassembly consists of (b) an upper electrode, (c) two chiral pairs of half electrodes at its centre, and (d) a lower electrode. The subassembly features a rectangular snout that readily admits a 1" diameter laser beam while maintaining the homogeneity of the internal spectrometer field. The two middle electrodes are recessed to allow a 1" diameter, f/2 mirror to be positioned within the electrode rings. The subassembly's electrodes feature single, wide guard rings. The middle electrodes' guard rings are grooved to allow the molecular beam to pass through the spectrometer. (e) View of the spectrometer's subassembly in situ. The bright disc located at the centre of the snout is the parabolic mirror. (f) View of the recessed side of the spectrometer's subassembly.*

these shortcomings, the four-electrode subassembly was developed to make the spectrometer compatible with an on-axis parabolic mirror.

Six thin (0.124 inch diameter) alumina rods with retaining rings at either end hold the subassembly together. Each rod features three 11 mm long alumina spacers as well as a spring that permits subassembly expansion during bake-out. Rather than a small, converging input laser beam, the subassembly admits a larger (25 mm diameter), collimated beam en route to the on-axis parabolic mirror. To accommodate the larger input laser beam aperture while mitigating the effect of fringing fields, a rectangular "snout" was incorporated into the subassembly (Fig. 2.22e). The snout's upper and lower surfaces consist of plates that project 22 mm outward from the

subassembly's top (Fig. 2.22b) and bottom (Fig. 2.22d) electrode rings. The subassembly's central electrodes consist of two chiral pairs of half-rings (Fig. 2.22c) featuring 14 mm high extensions that comprise the snout's sides. Opposite the snout, the C-ring electrodes are recessed (Fig. 2.22f) to permit the introduction of the *f*/2 on-axis parabolic mirror (see below). To inhibit external field penetration further, spot-welded ultrathin (50 μm diameter) stainless steel wires (Goodfellow Corp. type FE225110) horizontally connect each C-ring electrode pair at either end of the snout and also span the mirror recess. The molecular beam enters and exits the subassembly via 1.5 mm radius channels machined into the innermost surfaces of the C-electrodes.

On-Axis Parabolic Mirror Mount

The on-axis parabolic mirror (silver-coated aluminum, 25 mm diameter, 50 mm focal length) is mounted in a holder affixed to the end of a 16 inch long vented steel tube (Fig. 2.23a) attached to an XYZ-translation stage (Vacuum Generators model VZXYZ0515; Fig. 2.6h).

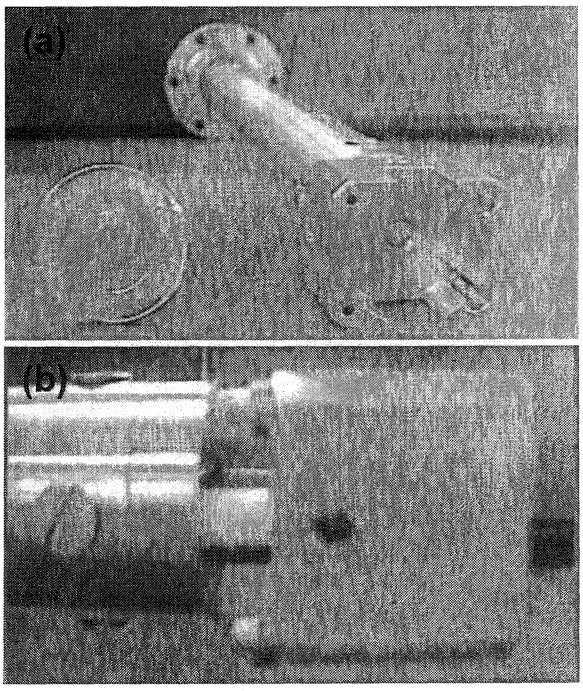

Fig. 2.23. Parabolic mirror mount. *(a) The rectangular mirror holder is designed to fit within the recessed portion of the spectrometer subassembly. The parabolic mirror is held in place by a set screw and two roll pins. The holder itself is mounted at the end of a 16" long vented steel tube welded to a non-rotatable 2-3/4" ConFlat flange. A two dollar coin (left) is included for scale. (b) Side view showing the four alumina spacers that electrically isolate the mirror holder from the mounting tube. A bolt (partially visible at centre) couples the holder to the mount tube's cap. The bolt is electrically isolated from the cap by an alumina washer and features a spring that prevents spacer breakage during bake-out. The screws at left secure the cap to the mounting tube. The two small screws threaded into the rear surface of the holder (top middle and bottom middle) enable the connection of wire leads used to apply and monitor the holder's bias voltage.*

During operation, the mirror is positioned within the recessed portion of the spectrometer's four-electrode subassembly. Both the mirror and its holder are referenced to the potential between the subassembly's central electrodes to prevent them from distorting the internal spectrometer field. The mirror holder is electrically isolated from the mounting tube by a system of alumina rods and washers (Fig. 2.23b). An incorporated stainless steel spring prevents breakage of the alumina rods during bake-out.

During its positioning, the mirror's voltage is measured *in situ* via a sense wire attached to the holder. Contact between the mirror holder and one of the subassembly's electrodes causes the mirror's potential to change. The magnitude and polarity of a voltage change indicate which of the electrodes is in contact with the holder. Flexible tantalum ribbons are spot-welded to each face of the mirror holder to ensure "soft" collisions between the mirror and the subassembly. The ribbons provide electrical contact with electrodes without introducing mechanical stress that could damage either the mirror or its translator.

The translator's 50 mm travel is sufficient to retract the mirror fully from its niche within the spectrometer's subassembly prior to the removal of the spectrometer from the chamber. The lowest four electrodes are slightly D-shaped (Figs. 2.22cdf) as a precaution against collisions with the mirror mount during spectrometer installation/removal.

Electrode Biasing

The electrode stack is electrically isolated from its surroundings to allow maximum flexibility when biasing the spectrometer. For ion collection, the spectrometer's top electrode is grounded externally and a positive acceleration voltage is applied to the bottom ring. Low (i.e., less than 100 V) acceleration voltages are produced using a commercial power supply or (for ripple-free operation) several batteries in series. A different supply (Stanford Research model PS350) is used to generate higher (100V-5 kV) voltages corresponding to a maximum

acceleration field of 208 V/cm. A homogeneous electric field is produced within the spectrometer by uniformly decreasing the potential of each electrode, from bottom to top. This is accomplished using a voltage divider network in which adjacent electrode pairs are connected in series by a single ultrahigh vacuum-compatible 10 MΩ resistor (diamond spiral thick film element on a heat-conducting ceramic substrate, IRC type CGH-1, uncoated). The resistors were tested and selected prior to installation to ensure a tolerance of ±0.3%. Since the resistors mount directly to the electrodes (Fig. 2.24a), only two vacuum feedthroughs are required to bias the spectrometer's seventeen electrode tiers. Each C-electrode within the spectrometer's subassembly is connected to its chiral counterpart via ultrathin steel wires as well as an additional Kapton-insulated copper one (Fig. 2.24b). The copper wires ensure that all C-electrodes remain biased in the event that the ultrathin wires break or detach from one end.

The parabolic mirror holder is biased using a resistor network connected in parallel with the electrode stack's voltage divider. All resistors are identical to those used to bias the spectrometer. From the accelerating voltage terminal to the ground connection, the second chain consists of two series resistors, two parallel pairs of resistors in series with each other, and 13 additional series resistors. The mirror holder bias connection is made between the parallel

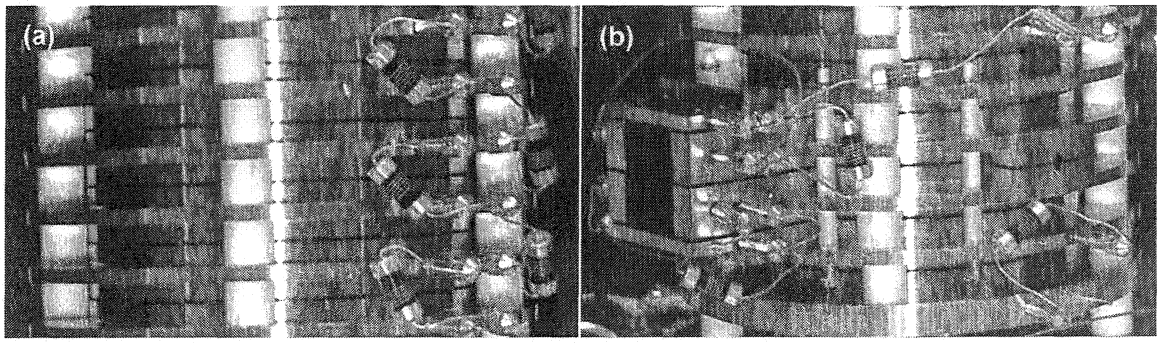

Fig. 2.24. Intrachamber resistor network. *(a) Each tier of the electrode stack is connected to its nearest neighbours by an ultrahigh vacuum compatible 10.00 MΩ resistor (right). (b) A single resistor also couples each tier of the spectrometer's subassembly. However, resistors are connected to only one side of the two half-ring electrode pairs at the subassembly's centre. Bias is supplied to the opposite sides by Kapton-coated copper wires (left) in addition to the ultrathin steel wires that connect each electrode pair.*

resistor pairs. This ensures that the mirror holder remains referenced to the potential at the centre of the spectrometer's subassembly as the accelerating voltage is varied.

Ion Mass Calibration and Resolution

In a uniform electric field of strength E, an ion with mass-to-charge ratio m/q and zero initial velocity along the field direction travels a distance D_{TOF} in a time given by $t_{TOF} = \sqrt{2mD_{TOF}/qE}$. This expression can be applied to the PATRICK instrument's time-of-flight mass spectrometer to predict the flight times of ions between the laser focus and detector. The expression is not exact since ions traverse an additional post-acceleration region a few millimetres wide between the top electrode and the detector. Nevertheless, to an excellent approximation, D_{TOF} can be taken to be the separation between the laser focus and the top electrode (≈200 mm). The electric field strength within the spectrometer is given by $E = V/L$ where V is the applied acceleration voltage and L = 240 mm is the distance between the centres of the top and bottom electrodes.

The essential first step when analyzing data obtained using the PATRICK instrument is the calibration of the ion time-of-flight spectrum. An expression of the form $m/q = A(t - t_0)^2$ is used to assign the correct mass-to-charge ratio to each peak in the spectrum. Here, t is the measured ion arrival time, t_0 represents delay between the triggering of timing electronics and the passage of the optical ionization pulse through the laser focus, and A is an empirical scale factor that is approximately equal to $\frac{V}{2LD_{TOF}}$. The calibration constants A and t_0 are determined via trial and error by assuming the mass-to-charge ratios m_1/q_1 and m_2/q_2 for two specific peaks. Solving the corresponding system of equations yields

$$A = \left(\frac{\sqrt{m_1/q_1} - \sqrt{m_2/q_2}}{t_1 - t_2} \right)^2$$

$$t_0 = \frac{\sqrt{m_1 q_2 / m_2 q_1}\, t_2 - t_1}{\sqrt{m_1 q_2 / m_2 q_1} - 1}$$

Inspection of the calculated mass-to-charge ratios $m_i / q_i = A(t_i - t_0)^2$ for other peaks in the spectrum (such as those due to background gas, e.g. H_2^+, H_2O^+, N_2^+, O_2^+) will then confirm or invalidate the hypothetical peak assignment. To illustrate this, a typical time-of-flight spectrum for the isotopes of Xe^+ is depicted in Fig. 2.25. The presumed mass assignment is clearly correct since it is consistent with the known natural isotopic abundances of xenon.

The conventional figure of merit for a mass spectrometer is the mass resolution $m/\Delta m$. A high-mass resolution spectrometer is capable of differentiating between ions with similar mass-to-charge ratios. The PATRICK instrument's time-of-flight spectrometer has a mass resolution of $m/\Delta m \approx 3750$ and therefore represents the state of the art.

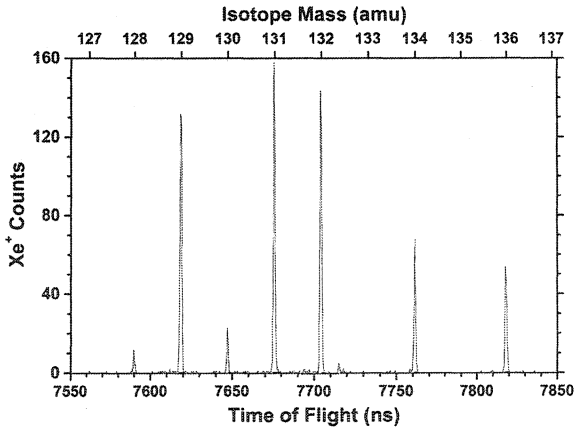

Fig. 2.25. Time-of-flight/mass spectrum of xenon isotopes. *The measured distribution of Xe^+ ions striking the non-imaging detector is depicted as a function of arrival time (bottom axis) and isotope mass (top axis). The corresponding mass calibration parameters are $A=2.3250\times10^{-6}$ amu·e^{-1}·ns^{-2} and $t_0=179.91$ ns. The widths of the isotope peaks correspond to an excellent mass resolution of $m/\Delta m \approx 3750$.*

2.5 Ion Detection

During the course of the project, two different ion detectors were used. Both are capable of recording the times and two-dimensional positions of multiple ion impacts per laser pulse.

Checkerboard Detector

The original detector consisted of a matched pair of microchannel plates (Galileo Corp. model Long-Life, 50.4 mm physical diameter, 40 mm quality diameter, 40:1 aspect ratio, imaging quality) and a "checkerboard" anode. The anode featured an 8×8 square array of independent electrode pads with a total active area of 841 mm^2 (29 mm × 29 mm). Each electrode pad was connected to a dedicated preamplifier, constant-fraction discriminator (LeCroy model 2735DC), and time-to-digital converter channel (LeCroy model 3377). Following each laser pulse, the arrival times of up to sixteen ions per electrode pad could be recorded.

While the checkerboard detector offered excellent (~1 ns) temporal resolution and multiple ion hit capability, two factors limited its suitability for the performance of molecular imaging. The detector's primary shortcoming stems from its relatively small number of electrode pads. Raw images obtained with the detector have poor spatial resolution since they contain only 64 pixels. While an interpolation algorithm could be used to improve the images' spatial resolution, such a procedure would consume excessive computer resources during data acquisition. The detector's highly parallel architecture poses a second difficulty since 64 time-to-digital converter channels must be continuously read-out during an experiment. This results in relatively slow data transfer between the time-to-digital converters and the acquisition computer (which limits the data acquisition rate) and large data sets, for which analysis can be onerous. A delay line anode that offers superior spatial resolution yet makes use of fewer time-to-digital converter channels eventually replaced the checkerboard detector.

2-D Helical Delay Line Anode Detector

Delay line anode detectors [Sob1988] became commercially available during the course of this project and are an emerging technology in laser-molecule experiments. Since only four (or five in the case of dispersive delay lines) time-to-digital converter channels are required to

acquire three-dimensional ion impact data with such detectors, the transfer, processing, and storage of data are streamlined. Moreover, the temporal and spatial resolutions of such detectors, as well as their abilities to detect multiple ions per laser pulse, are determined by the attached data acquisition electronics rather than detector architecture. Consequently, the characteristics of a delay line anode detector can be readily tailored to suit experimental requirements. The PATRICK instrument's detector offers ~62,000 spatial resolution elements (each with an area of 0.068 mm^2) that span the entire clear aperture of the time of flight spectrometer and a temporal resolution of 1 ns or better.

Ideal Delay Line Anode Detectors

The principle of the delay line anode is illustrated in Fig. 2.26. For simplicity, only a single delay line is shown. Upon colliding with the microchannel plate stack, an ion produces a short, localized burst of ~10^6 electrons that are collected by the delay line, i.e., within the dashed circle in Fig. 2.26a. The excess of electrons produces a pair of current pulses that propagate with a constant velocity toward opposite ends of the transmission line. The current pulses' respective arrival times, t_1 and t_2, at the ends of the delay line depend on the ion impact time t_{TOF} and position S according to

$$t_1 = t_{TOF} + \frac{\frac{1}{2}l - S}{v}$$
$$t_2 = t_{TOF} + \frac{\frac{1}{2}l + S}{v}$$

Here, l is the total length of the delay line, v is the current pulse velocity, and S is measured from the centre of the delay line. Solving the system of equations yields both the one-dimensional ion impact position and time. The impact position is proportional to the time difference t_1-t_2 and is

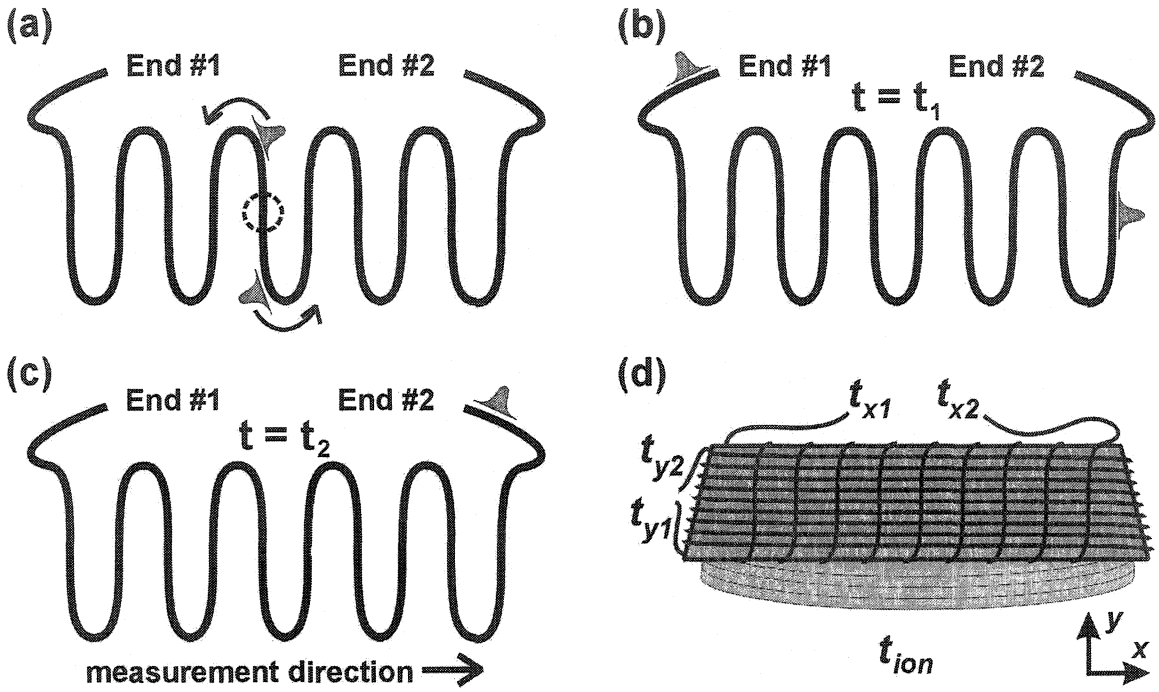

Fig. 2.26. Principle of delay line anode. *Panels (a)-(c) depict a single serpentine delay line. The same principle applies to each of the two orthogonal helical delay lines of the detector in panel (d). (a) An ion striking the microchannel plate stack at time t_{ion} produces ~10^6 free electrons, some of which accumulate at a specific location on the delay line (dashed circle). The excess of electrons gives rise to two current pulses travelling towards opposite ends of the delay line at constant speed. (b) The time t_1 at which the left-going pulse reaches the left end of the delay line is measured. (c) The time t_2 at which the right-going pulse reaches the right end of the delay line is measured. The one-dimensional displacement S of the ion impact from the centre of the delay line is proportional to the time difference t_1-t_2. The value of S can be calculated if the speed at which the pulses propagate along (or counter to) the measurement direction is known. Similarly, the ion impact time t_{ion} is proportional to t_1+t_2 and can be determined if the delay line's length (in the measurement direction) is also known. (d) A two-dimensional ion impact position (X,Y) can be determined using a pair of orthogonally wound, helical delay lines. Here, X and Y are proportional to t_{x1}-t_{x2} and t_{y1}-t_{y2}, respectively, and can be calculated if the effective propagation velocity for one delay line is known. If the delay lines are ideal (i.e., non-dispersive), t_{x1}+t_{x2}=t_{y1}+t_{y2} and t_{ion} can be calculated if the effective delay line lengths are known. Alternatively, t_{ion} can be measured directly at the microchannel plate stack.*

given by $S = \frac{v}{2}(t_1 - t_2)$. Conversely, the impact time depends on the time sum t_1+t_2 according to

$$t_{ion} = \frac{1}{2}\left((t_1 + t_2) - \frac{l}{v}\right).$$

Three-dimensional ion impact data can be obtained using a pair of delay lines oriented orthogonally with respect to one another. Each delay line can be either serpentine (as in Fig. 2.26a-c) or helical (as in the PATRICK instrument's detector; Fig. 2.26d). A generalization of

the above discussion yields the ion impact coordinates (X,Y) at time t_{ion} in terms of the current pulse arrival times t_{x1}, t_{x2}, t_{y1}, and t_{y2}:

$$X = \frac{v_x^{anode}}{2}\left(t_{x1} - t_{x2}\right)$$

$$Y = \frac{v_y^{anode}}{2}\left(t_{y1} - t_{y2}\right)$$

$$t_{ion} = \frac{1}{2}\left(\left(t_{x1} + t_{x2}\right) - \frac{l_x}{v_x^{anode}}\right) = \frac{1}{2}\left(\left(t_{y1} + t_{y2}\right) - \frac{l_y}{v_y^{anode}}\right)$$

Note that the subscripts x and y above refer to the parameters of the respective X- and Y-sensing delay lines. Thus, once the delay line lengths (l_x and l_y) and axial current propagation velocities (v_x^{anode} and v_y^{anode}) are known, the measurement of four experimental times (t_{x1}, t_{x2}, t_{y1}, and t_{y2}) is sufficient to characterize an ion impact completely. However, this holds only for ideal delay lines that do not exhibit current pulse velocity dispersion. When dispersive delay lines are used, the ion impact time t_{ion} can become uncertain since the strict equality of the respective lines' time sums will be relaxed, i.e., $t_{x1} + t_{x2} \approx t_{y1} + t_{y2}$. Measuring t_{ion} more directly (as the PATRICK instrument does) lifts this uncertainty.

RoentDek DLD-80 Detector Architecture, Mounting, and Biasing

The PATRICK instrument incorporates a commercial delay line anode detector (RoentDek GmbH model DLD-80) [Jag1998]. The detector consists of a matched microchannel plate pair (Galileo Corp. model Long-Life, 86 mm physical diameter, 75 mm quality diameter, 60:1 aspect ratio, detection quality) mounted in front of two flattened helical delay lines wound orthogonally about (and electrically isolated from) an aluminum plate (Fig. 2.27). The detector is suspended a few millimetres above the top grid of the time-of-flight mass spectrometer from a stainless steel mounting plate (Fig. 2.27d). The mounting plate is coupled to the spectrometer's top electrode by four steel rods and is electrically isolated from it by a system of alumina sleeves

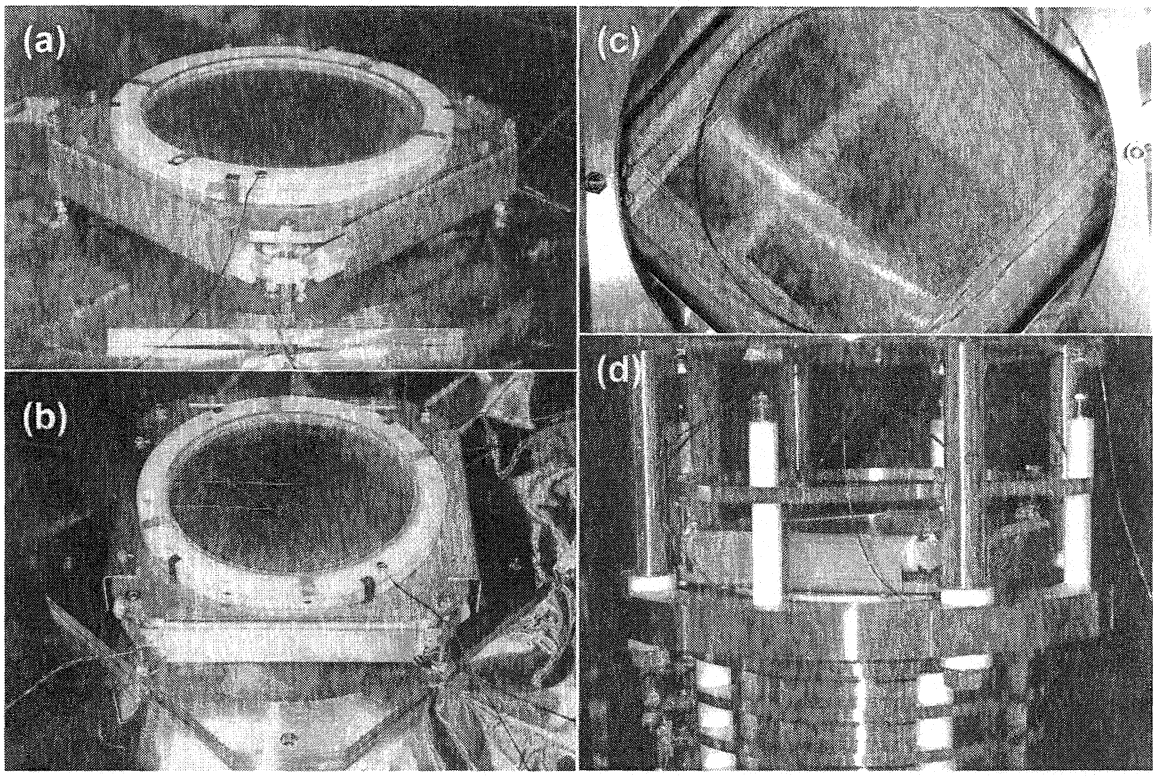

Fig. 2.27. 2-D helical delay line anode detector. *(a) Upside down view of the PATRICK instrument's detector (middle) and its mounting plate (beneath). The detector's pair of 86 mm diameter microchannel plates (not shown) are held between two alumina rings (white) atop the anode. The delay lines consist of nested flattened helices wound about half-round alumina spacers and a central aluminum plate. The white spacers are partially visible behind the detector's L-shaped guard plates. (b) Rotated upside down view of detector and mounting plate. (c) View of nested helices through hole in mounting plate. The delay lines are wound diagonally. (d) The detector assembly is shown mounted atop the time-of-flight mass spectrometer. The detector is suspended from the mounting plate such that its microchannel plate stack is just a few millimetres above the spectrometer's upper grid. Alumina sleeves and spacers (white) are used to isolate the detector assembly electrically from its four mounting rods and the spectrometer's top electrode.*

and spacers. A steel spring at the top of each rod prevents spacer breakage during chamber bake-out.

The detector is biased using a two-channel high voltage supply (RoentDek GmbH model NHQ 214M). One power supply channel is used exclusively for biasing the microchannel plate stack. A negative potential (typically -2000 V) is applied to the microchannel plate surface nearest the spectrometer. Since the spectrometer's top electrode is typically at ground potential, ions emerging from the spectrometer undergo a brief post-acceleration before impinging upon the

detector. The rear surface of the microchannel plate stack is also held at ground potential. The second power supply channel is connected to a network of potentiometers used to bias the delay lines as well as their aluminum back plate independently. The *Y*-sensing delay line has the smaller cross-sectional area and is nested within the *X*-sensing helix. To ensure that incident electrons are collected equally by the two helices, the inner coil is positively biased relative to the outer one. A higher positive voltage (typically +600 V) is applied to the inner aluminum plate to collect those electrons that pass through both delay lines without being collected.

Each delay line consists of two staggered copper wire spirals (of 2 mm pitch) separated by a uniform 1mm gap. One spiral of each pair is positively biased (+30 V) relative to its counterpart and acts as an electron collector. A current pulse propagating on a collector spiral is detected as a momentary change in the relative voltage between the windings at one end of the delay line. Pulses arriving at each of the ends are amplified and discriminated, before being clocked using a time-to-digital converter.

Although each delay line's collector helix has a pitch of 2 mm, ion impacts can be detected with sub-millimetre spatial resolution. The detector's ability to interpolate ion positions results from the dispersive nature of its delay lines. The various anode potentials are set to allow localized electron bursts originating from the microchannel plate stack to expand en route to the delay lines. Upon reaching a delay line, an electron cloud will span two or more turns of the collector helix and produce a similar number of current pulses on the line. Dispersion significantly broadens each sub-pulse until they overlap to form a counterpropagating pair of pulses on each delay line. The ion impact position determines the relative amplitudes of the various sub-pulses and hence the times at which their superpositions trigger the constant fraction discriminators at the ends of each delay line. Consequently, the detector's spatial resolution (~250 μm) is determined by the 500 ps bin size of the time-to-digital converter.

The use of dispersive delay lines also has implications for the detector's ability to resolve ion impacts temporally. As discussed above, the delay lines' current pulse time sums are only approximately equal ($t_{x1} + t_{x2} \approx t_{y1} + t_{y2}$) in the presence of dispersion. In such a case, a relatively poor time resolution (on the order of several nanoseconds) results if time sums are used to calculate the ion impact time t_{TOF}. Using a more direct method for determining t_{TOF} circumvents this difficulty. A single ion impact causes the emission of ~10^6 electrons from the microchannel plate stack and partially depletes its charge. In the PATRICK apparatus, the time t_{mcp} at which the transient charge depletion occurs is detected by monitoring the potential of the stack's output side. The physical ion impact time t_{TOF} can then be trivially obtained as $t_{mcp} = t_{TOF} + t_0$ (where t_0 is the offset time determined during mass calibration). While this direct timing approach requires an additional preamplifier, constant fraction discriminator, and time-to-digital converter channel, it improves the detector's temporal resolution to ~1 ns versus the time sum method.

Data Acquisition Electronics

Data acquisition is performed using commercial electronics (RoentDek GmbH model DLATR6 preamplifiers/constant fraction discriminators and a LeCroy model 3377 time-to-digital converter). The acquisition circuitry is activated prior to the passage of each laser pulse through the PATRICK apparatus. A TTL logic pulse from the Ti:sapphire regenerative amplifier's timing electronics serves as the start signal and triggers a commercial delay generator (Stanford Research model DG-535). The delay generator in turn activates the time-to-digital converter via a Phillips Scientific model 6915 constant fraction discriminator. Each time-to-digital converter channel can record a maximum of sixteen ion hits per laser pulse with 500 ps resolution. The recording of low mass-to-charge ratio ion hits can be suppressed by using the DG-535 unit to

delay the start of the time-to-digital converter. Once triggered, the time-to-digital converter records all ion hits that occur within a predetermined interval of up to 32 μs. When full, the time-to-digital converter's internal buffer is downloaded to the data acquisition computer.

Detector Calibration and Performance

Once installed, the detector was calibrated using a mercury arc lamp mounted at the bottom of the detector chamber (Fig. 2.28). A small percentage of the ultraviolet photons emitted by the lamp triggered electron avalanches within the microchannel plate stack via the photoelectric effect. By imaging such ultraviolet photon impacts (rather than laser-produced ions), detector calibration data was obtained *in situ* that was independent of the specific characteristics of the PATRICK apparatus' molecular beam, time-of-flight mass spectrometer, and laser focusing optics.

The mercury lamp was completely enclosed in a brass housing designed to conduct heat efficiently to the base of the chamber. Lamplight passed through a 1 cm diameter hole in the

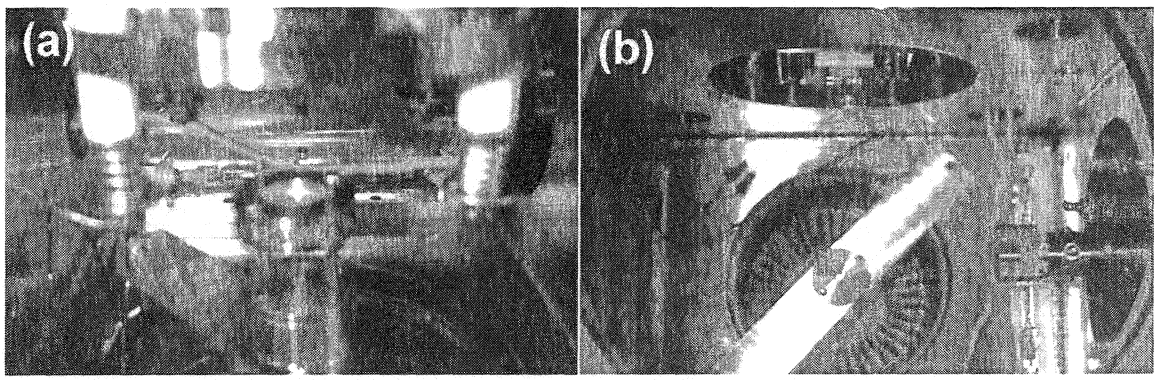

Fig. 2.28. Ultraviolet lamp assembly. *(a) The mercury arc lamp is shown in its thermally-conductive brass housing suspended over the turbomolecular pump port at the bottom of the detector chamber. Ultraviolet light passes upward through a 1 cm hole at the top of the housing. The light is diffused by a ground fused silica plate (centre) atop the housing before entering the time-of-flight spectrometer (top) en route to the detector (not shown). (b) View of the lamp assembly from above. The chamber's top flange (along with the spectrometer and detector) has been removed. The fan blades of the turbomolecular pump are visible beneath the lamp assembly. The piezoelectric slit (top), parabolic mirror and holder (right), and two halogen bake-out lamps (mounted to bottom of chamber on either side) are also shown.*

housing, upward through the mass spectrometer towards the detector. To improve the uniformity with which the detector was illuminated, a ground fused silica diffuser was mounted a few centimetres above the lamp housing.

During the first measurement, the microchannel plate stack was biased at an excessively high voltage (~2200 V) to generate electrons efficiently via thermal emission within the stack. Since the lamp was off during the measurement, the data consist exclusively of such dark counts. The data (Fig. 2.29a) are presented both in terms of the measured time differences on each delay line (t_{x1}-t_{x2} and t_{y1}-t_{y2}; top and right axes) and also as a spatial image (i.e., (X,Y); left and bottom axes). In either case, the data take the form of a rounded rectangle that results from the detector's

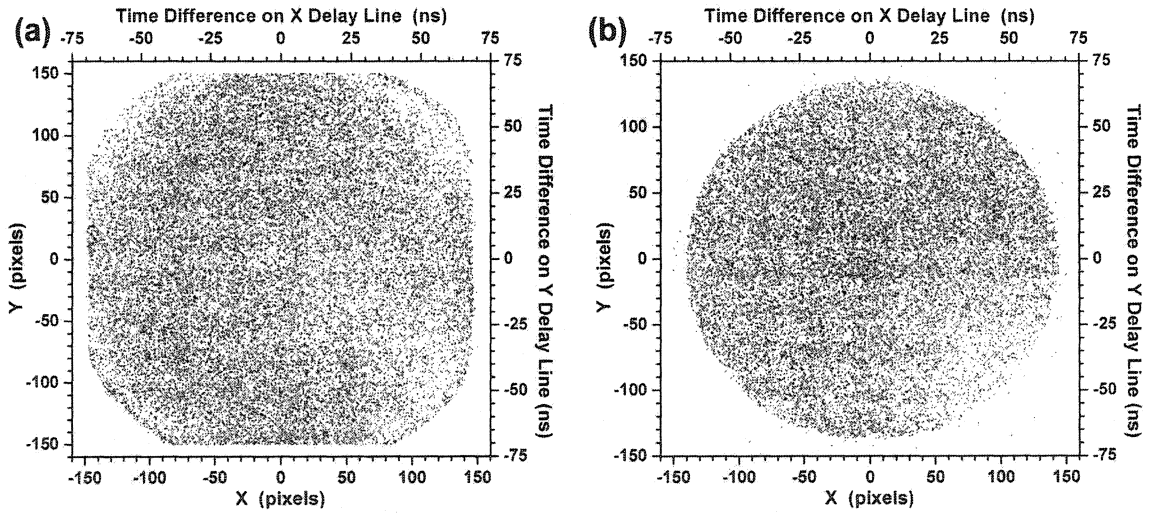

Fig. 2.29. Detector calibration data. *The distributions are plotted as functions of the time differences t_{x1}-t_{x2} (top axes) and t_{y1}-t_{y2} (right axes) and also in terms of spatial coordinates X (bottom axes) and Y (left axes) measured from the centre of the detector. The number of counts per pixel ranges from zero (white) to four (black). In real space, the pixels are rectangular with side lengths ΔX=255 μm and ΔY=267 μm. (a) Dark count distribution obtained using an excessive microchannel plate stack bias with the ultraviolet lamp off. The straight edges reflect the extent of the helical portions of the orthogonal delay lines. The rounded corners are due to the finite clear aperture of the microchannel plate stack. The distribution is essentially uniform with slightly fewer counts in the lower right quadrant and at large distances from the centre. (b) Ultraviolet photon impact distribution obtained using a typical microchannel plate bias voltage with the lamp on. The spectrometer partially masks the detector and only photons passing through its 70 mm diameter clear aperture are recorded. The data, however, are slightly elliptical. The distortion is due to the nested delay line geometry and can be completely removed via calibration. As in (a), the distribution is essentially uniform with slightly fewer counts recorded in the lower right quadrant.*

internal architecture. The rectangle's width and height reflect the dimensions of the respective *X*- and *Y*-sensing delay lines' helical sections. The rounding of the corners is due to the clear aperture (~82 mm diameter) of the microchannel plate stack mounted above the lines. The data show that emission/detection of thermally initiated electron bursts is approximately uniform across the detector. The uniformity of the image was optimized by carefully adjusting the thresholds of the four constant fraction discriminators attached to the ends of the delay lines. The measured emission/detection efficiency is somewhat lower near the microchannel plate edge (near the rounded corners in Fig. 2.29a), however. This observation is not likely due to the anode itself since microchannel plate stacks commonly exhibit decreased emissivities near their edge.

For the second measurement, the microchannel plate stack voltage was set to a typical operating value (~2000 V) and the mercury lamp was turned on. The data (Fig. 2.29b) take the form of a near-circular ellipse (due to ultraviolet photon impacts) with a few isolated counts just without (due to dark counts). The 70 mm diameter clear aperture of the mass spectrometer is smaller than the detector itself and gives rise to the ellipse. The slightly reduced detector response in the lower right quadrant was likely due to reduced microchannel plate emissivity there.

The nested delay line geometry gives rise to the elliptical nature of the data in Fig. 2.29b. Since current pulses propagate around the helices with identical velocities, the effective axial propagation velocity along the inner (*Y*-sensing) helix v_y^{anode} exceeds that of the outer (*X*-sensing) coil v_x^{anode}. Thus, for a circular detector mask (such as the spectrometer aperture), the maximum time difference for the *Y*-sensing delay line will be less than that of the *X*-sensing helix, i.e., $\left|t_{y1} - t_{y2}\right|_{\max} < \left|t_{x1} - t_{x2}\right|_{\max}$. The result is therefore an elliptical data set whose minor axis lies along the *y*-direction. As a first step towards obtaining an undistorted (circular) image, the effective anode pulse velocities v_x^{anode} and v_y^{anode} were determined using

$$v_x^{anode} = \frac{D_{TOF}}{\left|t_{x1} - t_{x2}\right|_{\max}} = 1.02\ mm/ns$$

$$v_y^{anode} = \frac{D_{TOF}}{\left|t_{y1} - t_{y2}\right|_{\max}} = 1.07\ mm/ns$$

where D_{TOF} = 70 mm is the diameter of the spectrometer's clear aperture. The pixelation of Fig. 2.29b stems from the discrete bin size of the time-to-digital converter (i.e., $\Delta t_{TDC} = 0.5\ ns$) used to record the anode pulse arrival times t_{x1}, t_{x2}, t_{y1}, and t_{y2}. While $t_{x1} - t_{x2}$ and $t_{y1} - t_{y2}$ are similarly quantized, the inequality of v_x^{anode} and v_y^{anode} gives rise to asymmetric spatial quantization. That is, the pixels of spatial images obtained with the PATRICK detector are rectangular with dimensions $dX = \frac{1}{2} v_x^{anode} d(t_{x1} - t_{x2}) = 255\,\mu m$ and $dY = \frac{1}{2} v_y^{anode} d(t_{y1} - t_{y2}) = 267\,\mu m$. By associating such dimensions with the pixels of images such as Fig. 2.29b, the distortion imposed by the nested delay lines can be completely removed.

The mercury lamp was also used to investigate the dependence of the time sums $t_{x1} + t_{x2}$ and $t_{y1} + t_{y2}$ on photon impact position (*X*,*Y*). Results for the *X*- and *Y*-sensing delay lines are depicted in Figs. 2.30a and 2.30b, respectively. Whereas the time sum for an ideal delay line is independent of impact position, the time sum varies linearly with impact coordinate for both the *X*- and *Y*-sensing helices. Since the trend is not an even function of position, this cannot be due to the dispersive nature of the delay lines. Rather, it is likely due to a slight tilt of the anode with respect to the microchannel plate stack. The vertical thickness of each data set stems from the helicity of the delay lines (since each turn of the *X*-sensing delay line, for example, extends over all *Y*-values). Note that the overall time sum variation for each delay line is less than 6 ns. This value is known hereafter as the "hit tolerances" Δt_x^{anode} and Δt_y^{anode} of the respective delay lines. Finally, by twice solving the time sum expression for an ideal delay line

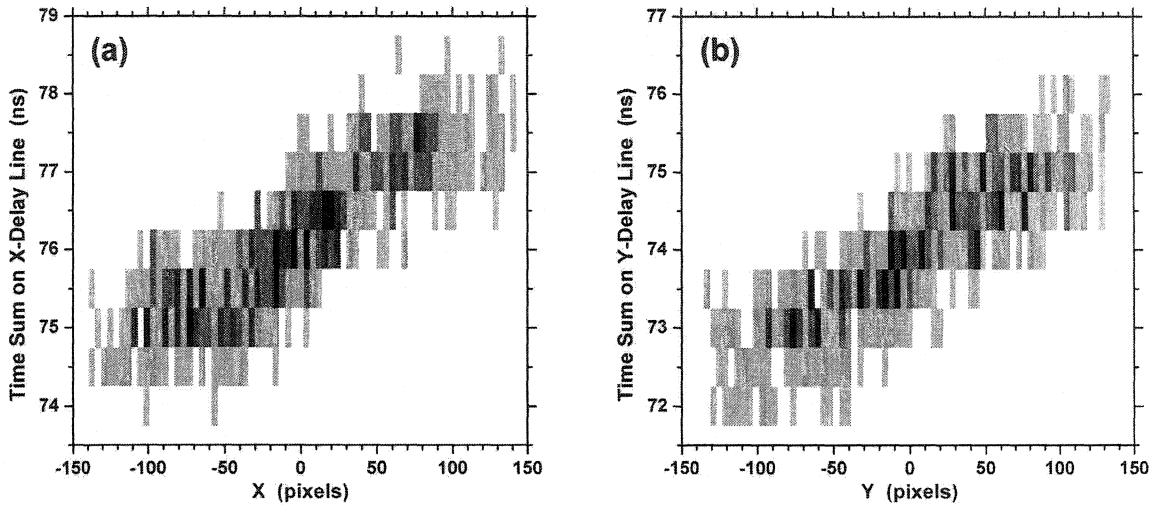

Fig. 2.30. Anode time sum data. *Using the ultraviolet photon impact data, the time sums (a) $t_{x1}+t_{x2}$ and (b) $t_{y1}+t_{y2}$ were calculated as a function of impact position for each delay line. Whereas the time sums should be independent of impact position for an ideal delay line, a linear dependence is observed for each of the actual delay lines. This effect is not due to dispersion (since the trend is not an even function of impact position) but likely results from a relative tilt between the microchannel plate stack and the anode wire planes. The vertical scatter of each data set originates from the helical nature of each delay line. The overall time sum uncertainty for each delay line is ~4 ns.*

(developed above) and replacing each time sum $t_{n1}+t_{n2}$ by the measured average $\langle t_{n1}+t_{n2}\rangle$, the effective length ($l_x$ and l_y) of each delay line was determined:

$$l_x = \left(\langle t_{x1}+t_{x2}\rangle - 2t_{mcp}\right)v_x^{anode}$$
$$l_y = \left(\langle t_{y1}+t_{y2}\rangle - 2t_{mcp}\right)v_y^{anode}$$

Note that l_x and l_y are effective (rather than actual) lengths since each delay line contains linear segments over which v_x^{anode} and v_y^{anode} do not apply (since they represent the anode pulse propagation velocities along the axes of the helices rather than along the delay lines themselves). The ion impact recognition section below details how knowledge of the hit tolerances Δt_x^{anode} and Δt_y^{anode} and the effective delay line lengths l_x and l_y is required for the correct characterization of ion impacts.

2.6 Primary Data Analysis

In this section, the set of fundamental data analysis steps common to virtually all experiments involving the PATRICK instrument are outlined. In all cases, individual ion impacts must be reconstructed by identifying quintuple coincidences amongst the raw timing data generated by the detector. The impact coordinates are then typically transformed to yield the initial three-dimensional velocity of each ion. To perform these functions (and others), a suite of specialized software tools has been developed.

Ion Impact Recognition

The raw data downloaded from the time-to-digital converter's buffer to the data acquisition computer lists the microchannel plate impact times t_{mcp} and anode pulse arrival times t_{x1}, t_{x2}, t_{y1}, and t_{y2} recorded after the passage of each laser pulse through the detector chamber. Two factors generally preclude the *a priori* ordering of raw timing data into quintuplets $(t_{mcp}, t_{x1}, t_{x2}, t_{y1}, t_{y2})$ representing actual ion impacts. First, more than one ion impact is typically recorded per laser pulse and the ordering of anode pulse arrival times may not be preserved at all four delay line ends. Second, the intrinsic pulse height distribution of the microchannel plate stack and the delay lines' dispersion prevent the anode's four constant fraction discriminators from being triggered with unit efficiency. As a result, one or more anode pulses may not be detected and clocked following each laser pulse.

The data acquisition software's most critical function is the unambiguous reconstruction of individual ion impacts from the raw timing data. Once downloaded, the timing data for each laser pulse is analyzed using an iterative algorithm that considers all possible $(t_{mcp}, t_{x1}, t_{x2}, t_{y1}, t_{y2})$ combinations in turn. To be classified as originating from an actual ion impact and retained, each

ordered quintuplet must satisfy three criteria. First, a quintuplet must satisfy a relation that reflects pulse propagation on the *X*-sensing delay line, namely

$$\left| t_{x1} + t_{x2} - 2t_{mcp} - \frac{l_x}{v_x^{anode}} \right| < \Delta t_x^{anode} .$$

Here, the time sum relation for an ideal delay line has been modified to reflect properties of the actual *X*-sensing delay line via the inclusion of the hit tolerance Δt_x^{anode}. To those quintuplets that satisfy the first criterion, an analogous constraint for the *Y*-sensing delay line is applied:

$$\left| t_{y1} + t_{y2} - 2t_{mcp} - \frac{l_y}{v_y^{anode}} \right| < \Delta t_y^{anode} .$$

Quintuplets that satisfy both requirements may in fact represent actual ion impacts and only the uniqueness of the impact coordinate assignments has yet to be verified. The third requirement is that neither of the first two criteria is satisfied more than once for a given impact time t_{mcp}. This ensures that only a single *X*-coordinate and a single *Y*-coordinate can be attributed to a given impact time t_{mcp}. While this constraint can (on very rare occasions) reject actual ion impacts, it is vital for preventing the assignment of incorrect coordinates to actual impacts and also excludes a range of potential artifacts from the data.

Those combinations $(t_{mcp}, t_{x1}, t_{x2}, t_{y1}, t_{y2})$ that satisfy all three criteria represent unambiguously assigned ion impacts and are retained for storage to a data file. Quintuplets that satisfy the three constraints above are not directly stored. Instead, the impact time t_{mcp} and the time differences $t_{x1} - t_{x2}$ and $t_{y1} - t_{y2}$ (which are proportional to the two-dimensional impact position) for each ion impact are recorded. More importantly, files are structured such that all of the data elements $(t_{mcp}, t_{x1} - t_{x2}, t_{y1} - t_{y2})$ within a given line were produced following the same laser pulse. By segregating the data in this manner, correlations (if any) between individual ion impacts are preserved.

Reference Frames and Spatial Origin Determination

In a molecular imaging experiment, there are two reference frames of interest: (1) the laboratory frame (X,Y,Z) in which measurements are performed, and (2) the molecular centre of mass frame (x,y,z) (i.e., the molecular beam frame) in which structure and dynamics are viewed.

The axes of the laboratory coordinate system are chosen to correspond with the design axes of the PATRICK instrument. The molecular beam propagates along the negative X-direction, the laser propagates along the Y-axis, and ions are accelerated in the positive Z-direction. The delay line detector is mounted such that its measurement axes lie along the X- and Y-directions. For simplicity, the origin of the laboratory frame is chosen to lie directly beneath the geometric centre of the detector, at the level of the laser focus. Consequently, the impact coordinates (X,Y) and flight time t_{TOF} of an ion in the laboratory frame are

$$\begin{aligned} X &= \tfrac{1}{2} v_x^{anode} \left(t_{x1} - t_{x2}\right) \\ Y &= \tfrac{1}{2} v_y^{anode} \left(t_{y1} - t_{y2}\right) . \\ t_{TOF} &= t_{mcp} - t_0 \end{aligned}$$

The laser focus will not generally be located beneath the centre of the detector due to the translatable nature of the parabolic mirror. Since background gas has zero mean velocity, the X- and Y-coordinates of the laser focus can be determined by singly ionizing background gas within the chamber. In such a measurement, the coordinates of the laser focus correspond to the centre of the ion impact distribution. This is illustrated using background water vapour (H_2O^+) in Fig. 2.31a where the focal coordinates (in pixels) are (2,-6).

The situation is more complicated when a molecular beam is used. The coordinate transformation from the molecular beam frame to the laboratory frame is given by

$$\begin{aligned} X &= x - |v_{mb}| t \\ Y &= y \\ Z &= z \end{aligned}$$

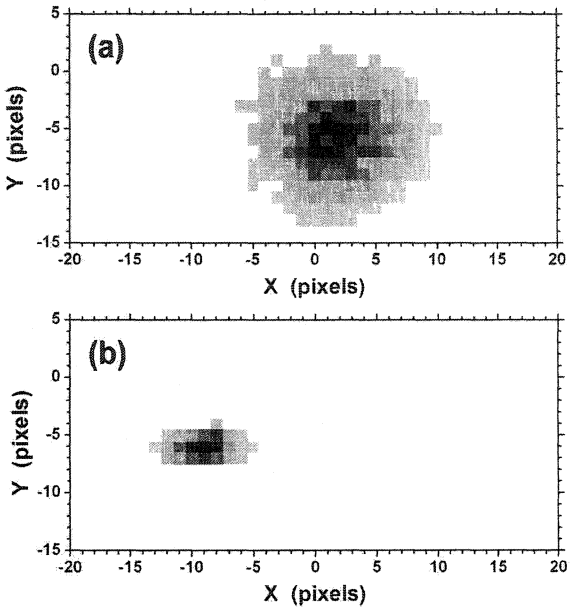

Fig. 2.31. Spatial origins of ion impact distributions. *(a) The H_2O^+ ion impact distribution resulting from ionization of background water vapour is shown. Since the mean velocity of background gas is zero, the centre of the distribution (2,-6) is located directly above the laser focus. (b) The N_2^+ distribution obtained following ionization of a molecular beam sample is depicted. The distribution's origin (-9,-6) is displaced in the –X-direction due to the nonzero mean velocity of the beam v_{mb}=734 m/s. The relative origin shift is a function of ion mass-to-charge ratio m/q, spectrometer voltage V, and gas reservoir pressure.*

where v_{mb} is the mean molecular speed within the beam. Therefore, the centre of the ion impact distribution (X_0,Y_0) depends on the molecular beam velocity and the ion flight time t_{TOF} as well as the position of the laser focus. This is illustrated in Fig. 2.31b, where the mirror position is identical to that of Fig. 2.31a, yet the N_2^+ distribution is shifted downstream to (-9,-6). Based on the measured ion flight time t_{TOF} = 3.8485 μs, the calculated molecular beam velocity is v_{mb} = 734 m/s. The dependence of (X_0,Y_0) upon ion flight time t_{TOF} implies that it will differ for each ion species and spectrometer's acceleration field.

In order to calculate quantities in the molecular frame, the spatial origins (X_0,Y_0) must be determined for each applicable species of ion. To make such determinations precisely, a robust algorithm was developed. Using Fig. 2.31a as an example, the number of ion impacts are histogrammed as a function of both X-coordinate ($H(X)$; Fig. 2.32a) and Y-coordinate ($H(Y)$; Fig. 2.32b). A nonlinear fitness function is then computed once for each coordinate using the corresponding histogram. Two fitness functions that have proven effective are:

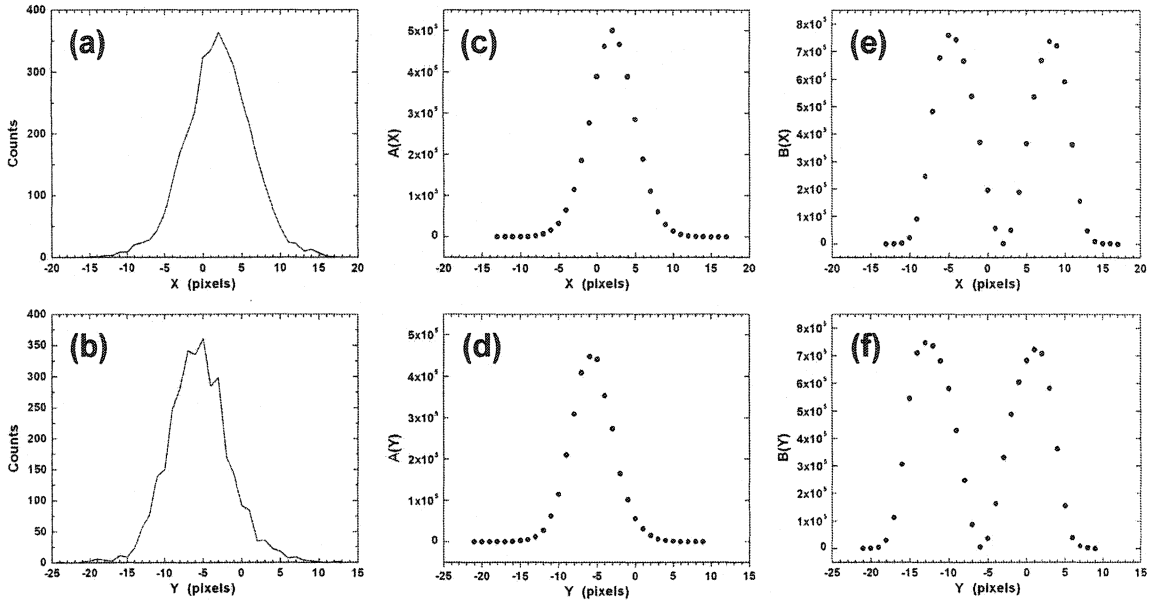

Fig. 2.32. Spatial origin determination. *Histograms of the X- and Y-coordinates (i.e. H(X) and H(Y)) of the H_2O^+ impact distribution of Fig. 2.31a are shown in (a) and (b), respectively. The one-dimensional origin (X_0 or Y_0) of each histogram can be determined using one of the fitness functions A and B. The functions A(X), A(Y), B(X), and B(Y) for the histogrammed data are plotted in (c)-(f), respectively. The spatial origin (X_0,Y_0)=(2,-6) corresponds to maxima in A and minima in B.*

$$A(X) = \sum_{\delta=0}^{\chi} H(X+\delta)H(X-\delta)$$

$$B(X) = \sum_{\delta=0}^{\chi} [H(X+\delta) - H(X-\delta)]^2$$

The functions $A(X)$, $A(Y)$, $B(X)$, and $B(Y)$ are plotted in Figs. 2.32c-f, respectively, for χ=15. Note that maxima occur in $A(X)$ and $A(Y)$ at $(X,Y)=(X_0,Y_0)=(2,-6)$ whereas $B(X)$ and $B(Y)$ take on minimum values. Although in this example the histograms $H(X)$ and $H(Y)$ are relatively simple, Gaussian-like functions, both A and B also yield correct results for double-peaked histograms.

Three-Dimensional Velocity Determination

The PATRICK instrument's ability to determine three-dimensional ion velocities is essential for the performance of molecular imaging via time-resolved Coulomb explosion. For self-diffraction imaging, a two-dimensional velocity measurement is likely sufficient. Of interest

are the ion velocity components in the molecular frame (v_x,v_y,v_z) immediately following ionization:

$$v_x = \frac{X - X_0}{t_{mcp} - t_0} dX$$

$$v_y = \frac{Y - Y_0}{t_{mcp} - t_0} dY$$

$$v_z = \frac{D_{TOF}}{t_{mcp} - t_0} - \frac{qV}{2mL}\left(t_{mcp} - t_0\right)$$

Here, (X,Y) are the laboratory frame ion impact coordinates measured in pixels, (X_0,Y_0) is the spatial origin for the ion with mass-to-charge ratio m/q, dX and dY are the respective X and Y pixel sizes, t_{mcp} is the microchannel plate impact time, D_{TOF} is the laser focus-detector separation, L and V are the mass spectrometer's length and accelerating voltage, and t_0 is the time offset determined via mass calibration of the time-of-flight spectrum.

2.7 Acknowledgements

Upon my arrival at the National Research Council in January, 1998, the PATRICK instrument was in a very early stage of development and its construction was overseen by post-doctoral fellow Christoph Ellert. At that time, only the detector chamber had been received from the NRC machine shops. Dr. Ellert and I jointly debugged the checkerboard detector that was then in place. While Dr. Ellert developed data acquisition software, I took charge of the construction, outfitting, and debugging of the source and intermediate chambers as well as the oven source and its temperature regulation system.

Following Dr. Ellert's departure in August, 1998, I assumed primary responsibility for the overall development and maintenance of the PATRICK instrument. I undertook the design of the vacuum chamber interlocks, the continuous gas source and mounting system, the source skimmer heater assembly, the piezoelectric slit mounting system, the spectrometer subassembly,

the parabolic mirror mount, and the helical delay line anode detector mounting assembly. I also redesigned the mass spectrometer (to accommodate the on-axis parabolic mirror and the helical delay line anode) and the gate valve separating the intermediate and detector chambers.

From July, 1999 to December 2000, post-doctoral fellow Ravi Bhardwaj assisted with the helical delay line anode detector feasibility study, molecular beam line alignment, and general chamber development. From 2001 onward, I was aided by post-doctoral fellow Igor Litvinyuk. Dr. Litvinyuk assisted in the installation, debugging, and calibration of the helical delay line anode and developed its data acquisition software. By 2002, the PATRICK instrument was fully operational and it was made available to three additional users who were assisted by Dr. Litvinyuk and me. During the preparation of this thesis, I began to transfer responsibility for the PATRICK instrument's maintenance and future development to others.

Numerous additional NRC staff members have made valuable contributions to the development of the PATRICK apparatus. Dr. Paul Corkum conceived of the instrument and offered invaluable advice throughout its evolution. The laser system was constructed and maintained by research officer Dr. David Villeneuve with the assistance of technical officer Bert Avery, post-doctoral fellow Manjusha Mehendale, and doctoral candidate François Légaré. The source, intermediate, and detector vacuum chambers, their mounting frame, the oven source, the time-of-flight mass spectrometer, and the checkerboard detector were initially designed by Dr. Ellert, technical officer John Parsons, and research officer David Rayner and fabricated by NRC machine shop staff. Timely assistance and roughing pump maintenance was provided by technical officer David Joines and Mr. Avery. Undergraduate student Chad Silverman assisted with the construction of the oven temperature control system and the vacuum chamber interlocks.

2.8 References

[Hua1992] C.-P. Huang, M.T. Asaki, S. Backus, M.M. Murnane, H.C. Kapteyn, and H. Nathel, *Opt. Lett.* **17** 1289 (1992).

[Jag1998] O. Jagutzki, V. Mergel, K. Ullmann-Pfleger, L. Spielberger, U. Meyer, R. Dörner, and H. Schmidt-Böcking, *Proc. SPIE* **3438** 322 (1998).

[Mar1987] O.E. Martinez, *IEEE J. Quantum Electron.* **23** 59 (1987).

[Nis1997] M. Nisoli, S. De Silvestri, O. Svelto, R. Szipöcs, K. Ferencz, Ch. Spielmann, S. Sartania, and F. Krausz, *Opt. Lett.* **22** 522 (1997).

[Sco1988] G. Scoles, *Atomic and Molecular Beam Methods* (Oxford University Press, New York, 1988).

[Sob1988] S.E. Sobottka and M.B. Williams, *IEEE Trans. Nucl. Sci.* **35** 348 (1988).

[Str1985] D. Strickland and G. Mourou, *Opt. Commun.* **56** 219 (1985).

[Wil1955] W.C. Wiley and I.H. McLaren, *Rev. Sci. Instrum.* **26** 1150 (1955).

Chapter 3
Optically Timed Sub-Millimetre Mass Spectrometry

The first set of experiments performed using the PATRICK instrument is detailed in this chapter. A simple, nonimaging detector was employed since these experiments preceded the installation of the helical delay line anode. Three novel mass spectrometric concepts are demonstrated: the optical timing of ion flight, the use of Coulomb explosion for ion detection, and the nested double time-of-flight mass spectrometer.

These experiments demonstrate that using intense femtosecond laser pulses to time ion flight optically can lead to the world's smallest time-of-flight mass spectrometer. Following laser ionization in the presence of a static electric field, a molecular ion is detected downstream by further ionizing it with a second laser pulse. The relative positions of the two laser foci determine the ion flight distance while the time separation of the laser pulses fixes the ion flight time. The masses of CS_2^+ and $C_6H_6^+$ isotopes are resolved after a flight distance of just 360 μm using either double ionization or Coulomb explosion detection.

This chapter is structured as follows. The benefits of femtosecond laser pulses to mass spectrometry as well as the optical timing concept are summarized in §3.1. The experimental configuration is described in §3.2. In §3.3, experimental results are presented for both ion detection schemes (double ionization and Coulomb explosion). The feasibility of actual optically timed miniature mass spectrometers, the advantages of Coulomb explosion detection, and the potential applications of the nested mass spectrometric configuration are discussed in §3.4.

3.1 Femtosecond Laser Pulses and Mass Spectrometry

Femtosecond pulses have been of interest in mass spectrometry primarily for their proposed ability to ionize molecules with little or no fragmentation [Led1997]. Recent research, however, calls this prospect into question [Han2000]. For organic molecules of intermediate size, at least, it appears that femtosecond pulses and electron impact methods produce similar fragmentation behaviour [Han2000]. Nevertheless, femtosecond pulses offer additional benefits of considerable importance for mass analysis, namely:

(1) Like electron beam ionization, strong-field ionization using femtosecond laser pulses is nonresonant and universal. Unlike electron beam methods, strong-field ionization can be highly efficient (~100%) and localized to a focal spot diameter of ~1 μm due to the nonlinearity of the light/matter interaction. Therefore, such pulses are well suited for miniature time-of-flight mass spectrometers whose mass resolution is determined by the ratio of the ion flight distance to the length of the ionization region along the flight direction. Miniature mass analyzers are of particular interest for applications such as spacecraft life-support, pollution monitoring, and explosives detection [Bad2000].

(2) Intense femtosecond pulses can further ionize molecular ions. Depending on the pulse intensity, this can be controlled to remove one or more additional electrons and can lead to Coulomb explosion [Hat1988, Str1992, Pur1994, Iva1996, Han2001]. Such localized post-ionization provides an optical method for detecting ions with high spatial resolution.

(3) The time separation between two ultrashort pulses can be controlled with femtosecond precision. Hence, a dramatic improvement in the measurement of ion flight times can be achieved using optical rather than electronic timing. This eliminates the principal barrier to the realization of miniature time-of-flight mass spectrometers.

(4) When used as a detection scheme, Coulomb explosion produces numerous ionic fragments that impinge upon a detector. This results in significant amplification of ion signal over parent ion detection. In contrast to conventional time-of-flight detection methods, this amplification increases with the size of the molecule.

In the experiments described below, a nested time-of-flight mass spectrometer that incorporates an optically timed miniature mass analysis stage is demonstrated. In so doing, it is shown that considerable miniaturization of mass spectrometers is possible. In addition, the feasibility of using Coulomb explosion to enhance the detection efficiency of such miniature devices is illustrated.

The optically timed approach involves focusing two temporally separated femtosecond pulses to positions that are less than 500 μm apart in the presence of a uniform, static electric field (Fig. 3.1). The pump pulse singly ionizes a gaseous sample while the delayed pulse probes the molecular ions for the presence of a specific mass. This approach enables mass analysis to be performed on a sub-millimetre scale.

The pump pulse is focused into a molecular beam and produces singly charged ions. The ions, moving with constant velocity v_{mb} in the molecular beam direction, are accelerated perpendicular to the beam by a uniform electric field. The probe laser focus is positioned to

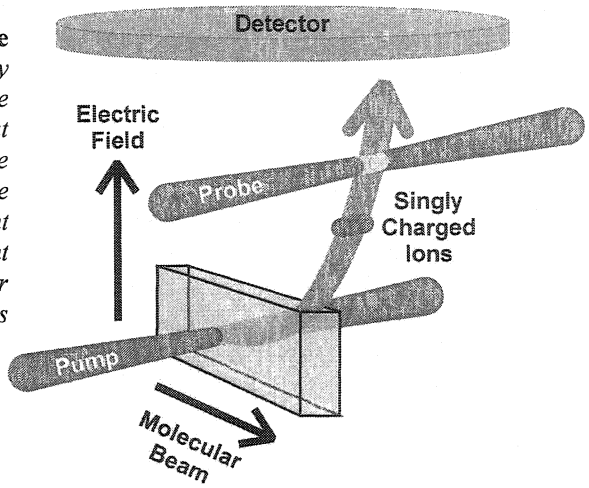

Fig. 3.1. Concept of optically timed miniature mass spectrometry. *The focused pump pulse singly ionizes molecules within the molecular beam. The cations are accelerated by a uniform electric field out of the beam along a parabolic trajectory. A more intense probe pulse is focused at a location along the trajectory and further ionizes any molecules present within its focal volume upon its arrival. Subsequent detection of multiply charged molecular ions (or fragments thereof) indicates that molecules of mass* $m = eE\tau^2/2\Delta z$ *are present in the molecular beam.*

intersect the parabolic ion trajectories, outside of the molecular beam (Fig. 3.1). En route to the probe focus, the ions separate spatially according to their masses. Consequently, different masses pass through the probe focus at different times. When the intense probe pulse arrives, it further ionizes or fragments any ions present. Subsequent detection of highly charged molecular ions or fragments indicates that a specific mass $m = eE\tau^2/2\Delta z$ was present in the sample, where e is the unit of elementary charge, E is the external electric field strength, Δz is the focal spot separation along the electric field direction, and τ is the pump-probe delay.

The cation mass probed in the second focal spot can be scanned by varying either the pump-probe delay, the spatial separation of the laser foci, or the accelerating electric field. Results obtained via the second and third approaches are presented in §3.3.

3.2 Experimental Configuration

The molecular beam was produced using the continuous gas reservoir whose 100 μm diameter nozzle was backed by 40 mbar of gas. In the interaction region, the ribbonlike molecular beam was 40 μm thick along the laser propagation direction and 1.5 mm wide. The mean velocity of molecules within the beam was measured to be $v_{mb} = 550$ m/s. The respective operating pressures within the source, intermediate, and detector chambers were 7×10^{-5} mbar, 1×10^{-8} mbar, and 2×10^{-9} mbar.

The optical configuration is depicted in Fig. 3.2. A half-wave plate/cube polarizer combination was used to divide the Ti:sapphire regenerative amplifier's output (800 nm wavelength, 500 μJ pulse energy, 50 fs duration, 500 Hz repetition rate) into pump and probe pulses. In order to obtain pump-probe delays of $\sim 10^{-7}$ s, a delay line consisting of a pair of 2 m focal length spherical mirrors placed 4 m from two flat dielectric mirrors was constructed. The probe beam was focused at the input of the delay line and followed a bowtie path (56 m total

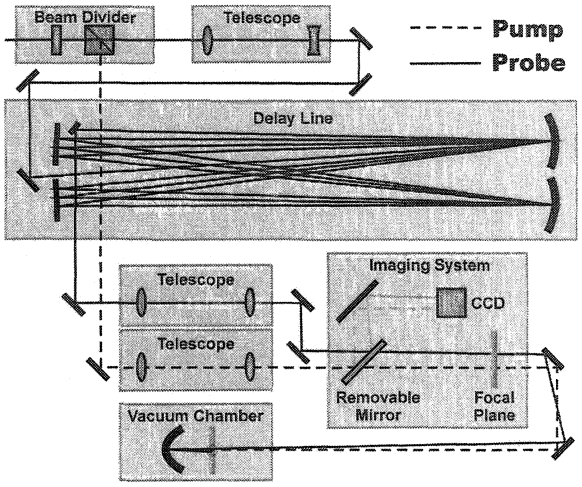

Fig. 3.2. Optical configuration. *Output from the Ti:sapphire regenerative amplifier was divided into pump and probe pulses. The probe pulse was focused at the input of the optical delay line by a telescope and refocused after each round trip by spherical mirrors. Both pulses were focused in a common vertical plane before entering the vacuum chamber. The relative separation of the external foci was determined by temporarily inserting a mirror to shift them onto a CCD camera. Without the removable mirror in place, the intrachamber parabolic mirror imaged the external foci into/onto the edge of the molecular beam with a demagnification of ~41:1.*

length) as the concave mirrors repeatedly imaged the input focal spot onto the flat mirrors. The overall pump-probe delay was 203 ns.

The pump and probe pulses were focused to ~8 μm diameter spots by the detector chamber's parabolic mirror. The probe focus was positioned 110 μm (i.e., 550 m/s × 203 ns) downstream along the molecular beam direction from the pump focus (i.e., $x = 110\ \mu m$) and 360 μm closer to the detector ($\Delta z = 360\ \mu m$). An imaging system (magnification ~41:1) was used to monitor the relative positions of the two foci during their adjustment (Fig. 3.2).

The dimensions of the pump and probe focal spots exceeded the diffraction limit since each pulse was obliquely incident upon the parabolic mirror. Oblique incidence was required to separate the pump and probe focal spots but gave rise to considerable comatic aberration. The degree of aberration increased with the numerical aperture of each beam as well as the separation of the two foci (Fig. 3.3). For a given numerical aperture, the actual focal spot dimensions are given by the convolution of the raytraced intensity distribution (Fig. 3.3) with the diffraction limited intensity profile. For $\Delta z = 360\ \mu m$, the optimal numerical aperture is ~*f*/3.3. Consequently, the diameters of the pump and probe beams were adjusted to achieve *f*/3.3 focusing.

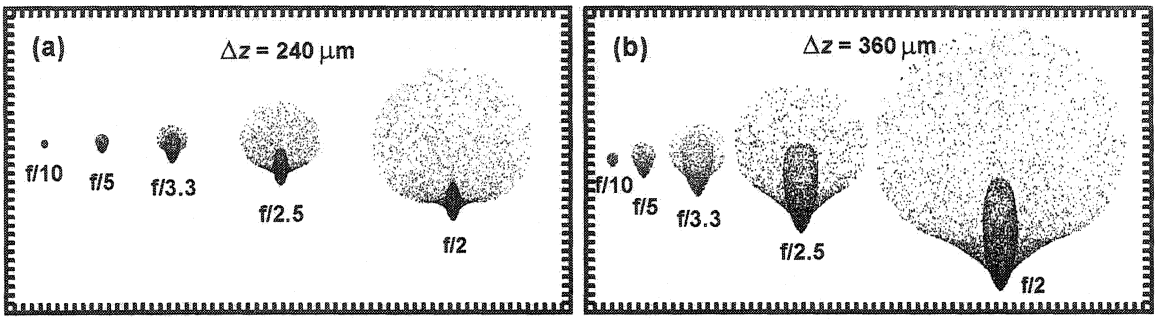

Fig. 3.3. Raytraced probe focal spots. *Raytraced optical intensity distributions in the focal plane of the probe pulse are depicted as a function of numerical aperture for pump-probe separations of (a) Δz = 240 μm and (b) Δz = 360 μm. The tick separation on each axis corresponds to a distance of 1 μm in the focal plane. In each case, the pump pulse propagates along the parabolic mirror's axis while the probe pulse is obliquely incident. Comatic aberration gives rise to scallop-shaped focal spots. The degree of aberration increases with numeral aperture and pump-probe separation Δz.*

Positioning of the foci relative to the molecular beam was achieved by translating the parabolic mirror. The pump focus was placed within the molecular beam while the probe focus was positioned on its edge. Given the universality of femtosecond laser ionization, probing is best performed in a region devoid of background gas. During the experiments, a gas density ratio of ~20:1 between the pump and probe foci was achieved.

Ions generated within the pump focal volume were accelerated by the uniform (~125 V/cm) electric field produced by the PATRICK instrument's time-of-flight mass spectrometer (mass resolution $m/\Delta m = 3750$). This arrangement represented a nested configuration in which the miniature all-optical mass analyzer resided within the PATRICK instrument's mass spectrometer. Ions were detected using a microchannel plate stack in combination with a conical anode. The ion signal was amplified, discriminated, and time-binned using a multichannel scaler (FastComTec model 7886A) with 500 ps temporal resolution.

3.3 Results

Mass analysis of CS_2 and C_6H_6 over a distance of just 360 μm was demonstrated using two different ion detection schemes. In each instance, a 30 μJ (~1 × 10^{14} W/cm^2) pump pulse

produced singly charged molecular ions. In the first approach, a 50 μJ (~1.7×10^{14} W/cm^2) probe pulse was used to ionize the molecular cations and the production of doubly charged molecular ions was monitored. In the second approach, a more energetic 60 μJ (~2×10^{14} W/cm^2) probe pulse was used to Coulomb explode the molecular cations.

Doubly Ionized Molecular Ion Detection

The universality of femtosecond ionization is both an asset and a liability. The pump pulse energy (30 μJ) was chosen to generate cations efficiently without excessive dication production. There are three possible sources of dications and these are readily identified using the PATRICK instrument's mass spectrometer: direct double ionization by the pump pulse, direct double ionization by the probe pulse of molecules near the edge of the molecular beam, and consecutive ionization by the pump and probe pulses. These three processes are shown in Fig. 3.4 for CS_2. Three triplets of peaks are in evidence, one for each production mechanism. The triplet corresponding to CS_2^{2+} produced by the pump pulse alone arrived first while that generated by the probe pulse alone arrived last. The temporal separation of the "pump only" and the "probe only" triplets corresponds to the pump-probe delay (203 ns).

The peaks of each triplet correspond to the isotopes of CS_2 ($^{76}CS_2$, $^{77}CS_2$, and $^{78}CS_2$). The

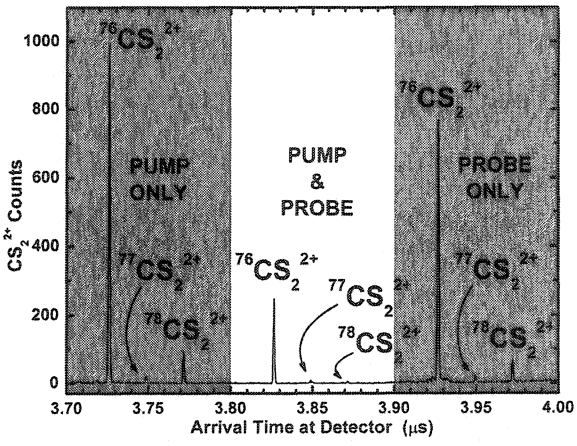

Fig. 3.4. CS_2^{2+} time-of-flight spectrum. *The spectrum of arrival times of CS_2^{2+} ions at the detector consists of three triplets of peaks. Each peak within a triplet corresponds to a different isotope. The outer triplets (shaded regions) result from double ionization by either the pump pulse (leftmost triplet) or probe pulse (rightmost triplet), reflect natural isotopic abundances, and are separated by the pump-probe delay. The central triplet stems from consecutive one-electron removals in each of the pump and probe foci. Relative peak heights within the central triplet depend on focal spot separation and acceleration field.*

relative peak heights within the "pump only" and "probe only" triplets reflect the natural isotopic abundances of CS_2. The central triplet is produced by the pump and probe pulses jointly and is therefore the signal of interest. However, the relative peak heights within this "pump-probe" triplet are different. This is because the accelerating voltage was chosen to place $^{76}CS_2^+$ at the centre of the second focus upon the arrival of the probe pulse. Hence, the $^{77}CS_2^{2+}$ and $^{78}CS_2^{2+}$ peaks are suppressed.

Experimental Confirmation of Mass Equation

Two methods were employed to verify that the central triplet of Fig. 3.4 obeyed the mass equation $m = eE\tau^2/2\Delta z$. In so doing, it was confirmed that the two foci effectively constitute a miniature time-of-flight mass spectrometer.

In the first approach, the separation of the pump and probe foci Δz was varied (Fig. 3.5). At each focal spot separation, the optimal electric field strength E at which the $^{76}CS_2^{2+}$ peak maximized was noted. The variation of optimal field strength with focal spot separation was

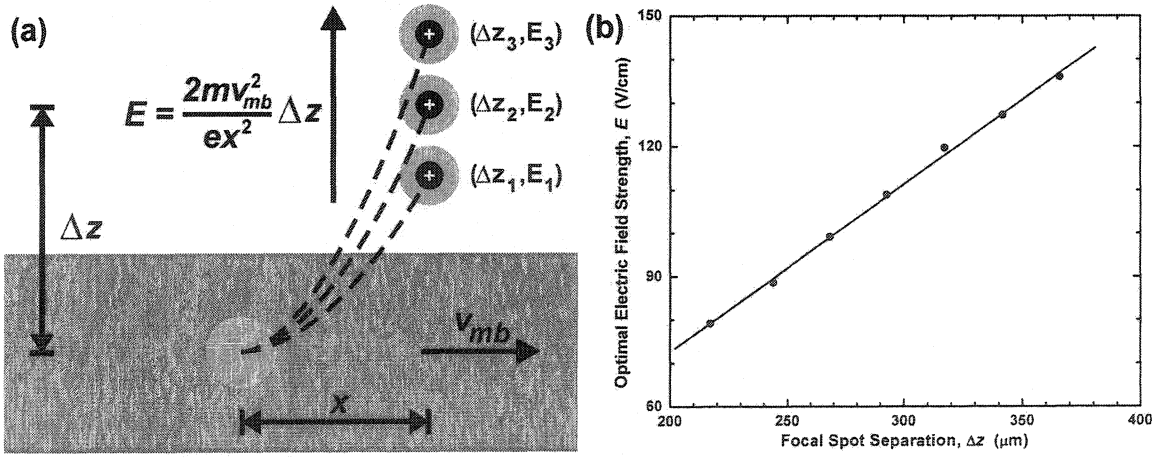

Fig. 3.5. Optimal electric field strength versus focal spot separation. *(a) For a given focal spot separation Δz_i, an ion of mass m and charge e produced in the pump focus will be located at the centre of the second focus upon the probe pulse's arrival if the electric field strength is optimal, i.e., $E = E_i$. The optimal field strength is expected to vary linearly with focal spot separation with slope $2mv_{mb}^2/ex^2$, where $v_{mb} = 550$ m/s and $x = 110$ μm. (b) The electric field strength E at which the central triplet's $^{76}CS_2^{2+}$ peak (Fig. 3.4) maximizes is depicted as a function of focal spot separation Δz. The observed slope of 0.388 ± 0.008 V·cm^{-1}·μm^{-1} agrees with the expected value of 0.396 V·cm^{-1}·μm^{-1}.*

observed to be linear with a slope of 0.388 ± 0.008 V · cm^{-1} · μm^{-1}. This is in agreement with the mass equation's prediction of $2mv_{mb}^2/ex^2 = 0.396$ V · cm^{-1} · μm^{-1} (where $x = 110$ μm is the focal spot separation along the molecular beam direction and $v_{mb} = 550$ m/s).

In the second approach, the focal spot separation was fixed ($\Delta z = 360$ μm) while the accelerating field was varied. The pump-probe signals for the isotopes of CS_2^{2+} are depicted in Fig. 3.6a as a function of acceleration voltage. The relative heights of the isotope peaks approximate the natural abundances of CS_2. The voltage at which each isotope signal maximizes is unique and is consistent with the predictions of the mass equation $m = eE\tau^2/2\Delta z$. This was also the case for the isotopes of $C_6H_6^{2+}$ (Fig. 3.6b). This represents a further demonstration of the principle of optically timed mass spectrometry after an ion flight distance of just 360 μm.

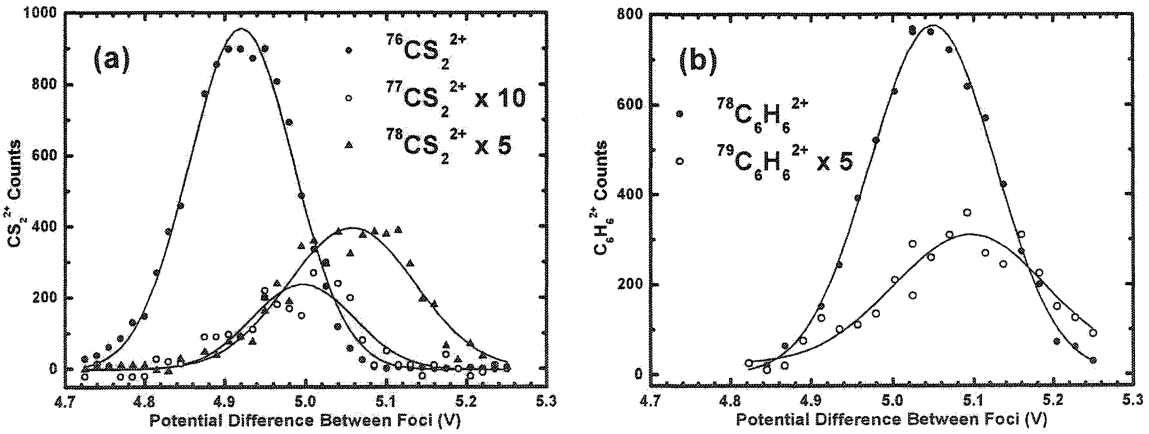

Fig. 3.6. Doubly ionized molecular ion detection data. *(a) Integrated $^{76}CS_2^{2+}$ (filled circles), $^{77}CS_2^{2+}$ (hollow circles), and $^{78}CS_2^{2+}$ (triangles) signals for the central triplet of Fig. 3 as a function of potential difference between foci are shown. For clarity, the magnitudes of the $^{77}CS_2^{2+}$ and $^{78}CS_2^{2+}$ signals have been increased by factors of 10 and 5, respectively. Gaussians fit to each data set have centres consistent with the mass equation $m = eE\tau^2/2\Delta z$ and heights reflecting relative isotopic abundances. (b) Results for $^{78}C_6H_6^{2+}$ (filled circles) and $^{79}C_6H_6^{2+}$ (hollow circles; plotted with a 5× magnitude enhancement) are consistent with both the mass equation and expected isotopic abundances.*

Mass Resolution of Miniature Mass Spectrometer

The data presented in Fig. 3.6 imply a mass resolution of $m/\Delta m \approx 40$ for the optically timed mass analyzer. The achievable mass resolution is determined by the diameters of the foci relative to the ion flight distance. Since the pump and probe beams impinged upon the parabolic mirror at an angle, comatic aberration produced focal spot diameters ~2 times larger than the diffraction limit for the given focusing conditions. Using diffraction-limited $f/1$ foci would yield a mass resolution of $m/\Delta m \approx 320$. Alternatively, the ion flight distance could be reduced to $\Delta z \approx 45$ μm without loss of mass resolution. In either case, the required pulse energies would be reduced by a factor of ~64. An additional improvement in mass resolution should result if the acceleration field structure was modified to achieve space focusing.

Coulomb Explosion Detection

A second ion detection scheme was demonstrated in which a more intense probe pulse removed many electrons from the molecular cation, initiating fragmentation. This is in contrast to the previous scheme in which a single electron was removed in the probe focus.

Fig. 3.7a depicts the time-of-flight spectrum of CS_2 obtained by subtracting "pump pulse only" and "probe pulse only" spectra from that produced by the pump and probe pulses in concert. As a result, it reflects only those ions produced via single ionization in the pump focus and subsequent multiple ionization in the probe focus. Numerous fragments (C^+, C^{2+}, S^+, S^{2+}, S^{3+}, and CS^+) were observed. Coulomb explosion of the highly charged parent ions imparts large kinetic energies (on the order of tens of eV) to the fragments. As a result, the fragment peaks in Fig. 3.7a are considerably broader than that corresponding to unexploded CS_2^{2+}.

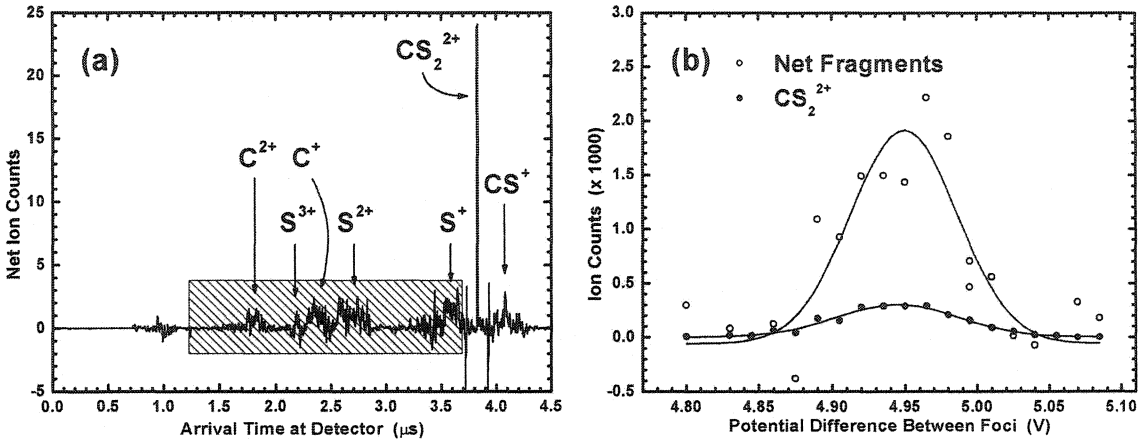

Fig. 3.7. Coulomb explosion detection data. *(a) Net spectrum of detector arrival times for the dication and charged fragments of CS_2. The spectrum was obtained by subtracting the individual arrival time spectra for the pump and probe pulses used alone from that produced using the two pulses concurrently. The integration window for fragment signal measurement is also shown (hatched region). (b) Integrated CS_2 fragment (hollow circles) and CS_2^{2+} (filled circles) signals as a function of potential difference between foci are shown. The peak voltages of the two signals effectively coincide, thereby demonstrating the validity of Coulomb explosion detection. The net fragment counts are many times greater than the unenhanced CS_2^{2+} signal, due in part to the amplification inherent to Coulomb explosion detection.*

The net monatomic fragment signal (indicated by the hatched region in Fig. 3.7a) as a function of ion acceleration voltage is shown in Fig. 3.7b. For comparison, the voltage dependence of the concurrently recorded $^{76}CS_2^{2+}$ is also shown. Note that Fig. 3.7b is the Coulomb explosion analogue of Fig. 3.6. Both the net fragment and $^{76}CS_2^{2+}$ signals maximize at the same voltage (Fig. 3.7b) and yield the correct mass for the $^{76}CS_2$ parent molecule. The net fragment data contains more scatter than its unexploded counterpart due to the spectral subtraction procedure used to isolate the net fragment signal.

Finally, the magnitude of the net fragment peak was ~6 times greater than the maximum $^{76}CS_2^{2+}$ signal. This was due in part to the ion signal amplification (i.e., the production of multiple fragments per molecule) inherent to Coulomb explosion detection. For larger polyatomic molecules, the degree of amplification should increase substantially.

3.4 Discussion

Using the optically timed approach, it should be possible to construct a relatively simple miniature mass spectrometer. Miniaturization greatly relaxes requirements for power sources, vacuum, and detection electronics. In the demonstration described above, the potential difference between pump and probe foci was only ~5 V. For a pair of closely spaced (~1 mm) electrodes, a household battery can provide an equivalent acceleration field.

While the PATRICK instrument's mass spectrometer requires a high vacuum environment to preclude ion collisions with background gas, only rough vacuum is required for the sub-millimetre flight distances of a miniature device. Therefore, an actual device could be made highly portable if a rudimentary pump is used to provide evacuation. A further requirement for such a device is that the initial velocity of molecules in the pump focus towards the detector be minimal. This constraint was satisfied in the above demonstrations using a molecular beam but could be met in a miniature device by placing the pump focus on the axis of an effusive molecular jet.

Pulse intensity is the critical parameter in strong field ionization. To implement the optically timed approach, respective pump and probe intensities of $\sim 1 \times 10^{14}$ W/cm^2 and $\sim 2 \times 10^{14}$ W/cm^2 are required [Han2001]. Commercially available 10 fs oscillators operate at a peak intracavity power of $\sim 5 \times 10^6$ W and often incorporate intracavity foci. Therefore, it should be possible to attain an intracavity intensity of $\sim 5 \times 10^{14}$ W/cm^2 and perform mass spectrometry at 10^8 Hz using relatively simple lasers.

The use of two synchronized laser oscillators would eliminate the need for a long optical delay line and make the optical configuration quite simple and compact (Fig. 3.2). Such a modification would yield additional benefits including a readily variable pump-probe delay, an elimination of probe pulse attenuation and beam aberration (previously due to multiple reflections

within the delay line), and an enhancement of probe pulse pointing stability (previously degraded by mirror vibrations and air currents within the delay line).

Pump and probe pulses could in principle be delivered to a miniature device via optical fibres and focused by microlenses mounted on the fibre tips. Using diffraction limited *f*/1 focusing, 1 μJ pulses from commercially available compact fibre-based laser systems would be more than adequate to implement Coulomb explosion detection. Thus, there are numerous options for the lasers required to perform optically timed mass spectrometry.

During the Coulomb explosion process, numerous ionic fragments are produced per molecule. Since highly charged fragments can be produced [Pur1994], the number of free electrons can be even larger. For large polyatomic molecules, these inherent amplifications of detectable particles could be large [Pur1994] and make concurrent detection of electrons and fragments feasible using a pair of simple electrodes and a current amplifier. Consequently, Coulomb explosion detection represents one of the most important potential applications of femtosecond mass spectrometry.

In addition to enabling the performance of compact mass spectrometry, the optically timed approach provides the basis for a sub-millimetre scale mass selector with potential applications in ion physics. This is demonstrated in Fig. 3.4 where an appropriate choice of experimental parameters enhanced the central triplet's $^{76}CS_2^{2+}$ signal relative to the $^{77}CS_2^{2+}$ and $^{78}CS_2^{2+}$ peaks. Experiments on ion ensembles devoid of neutrals are typically performed using a tandem mass spectrometer that incorporates separate stages for ion production, selection, and post-interaction analysis [deH1996]. By using the two foci for ion production and selection, all three of these functions have been demonstrated within the PATRICK instrument's time-of-flight spectrometer. In so doing, the commonly used tandem spectrometric configuration was reduced to a more compact, nested one.

The nested spectrometric configuration could have many scientific applications. These include:

(1) *Vibrational state-selective ion studies.* The narrower bandwidth of a picosecond pump pulse would allow the preparation of molecular ions in a specific vibrational state. This would enable state-selective studies to be performed in the nested configuration without a noticeable degradation of mass resolution. The synchronization of a tunable picosecond pump laser with a femtosecond probe laser can be achieved with a jitter of ~1 ps using commercially available technology. Note that this represents a precision of ~1:10^5 with respect to a 100 ns pump-probe delay.

(2) *Studies of molecular ion dynamics.* A picosecond pump laser can prepare an ensemble of mass-selected molecular ions in the vibrational ground state. Femtosecond pump-probe dynamics experiments could then be performed in the downstream focus. Used in this manner, the nested configuration ensures that the ensemble under study is devoid of neutrals and consists solely of ions with a common charge-to-mass ratio.

(3) *Measurement of transient ion lifetimes.* In conventional measurements, transient ion lifetimes are determined from the structure of their mass peaks where the resolution is on the order of the flight time. Since the optically timed approach enables the performance of mass analysis over sub-millimetre distances with nanosecond flight times, the accuracy of transient lifetime measurements could be enhanced using the nested configuration.

3.5 Conclusions

An optical approach to mass analysis using femtosecond laser pulses that enables the miniaturization of time-of-flight mass spectrometers has been presented. For large molecules, Coulomb explosion detection can greatly enhance the sensitivity of such devices. Finally, a

nested spectrometric configuration in which ion production, mass selection, and post-interaction analysis are performed within a single mass spectrometer has been demonstrated.

3.6 Acknowledgements

The author constructed the optical configuration described in this chapter and analyzed the experimental data. Data collection was performed in collaboration with post-doctoral fellow Ravi Bhardwaj. A manuscript summarizing this work has been accepted for publication in Analytical Chemistry [Doo2003]. We proposed that both the Canadian Institute for Photonic Innovations and the National Research Council patent this concept but they declined for lack of an industrial partner.

3.7 References

[Bad2000] E.R. Badman and R.G. Cooks, *J. Mass Spectrom.* **35** 659 (2000).

[deH1996] E. de Hoffmann, *J. Mass Spectrom.* **31** 129 (1996).

[Doo2003] P.W. Dooley, V.R. Bhardwaj, D.M. Rayner, and P.B. Corkum, accepted for publication in *Analytical Chemistry.*

[Han2000] S. Hankin, D. Villeneuve, P.B. Corkum, and D.M. Rayner, *Phys. Rev. Lett.* **84** 5082 (2000).

[Han2001] S. M. Hankin, D. M. Villeneuve, P. B. Corkum, and D. M. Rayner, *Phys. Rev.A* **64** 013405 (2001).

[Hat1988] P.A. Hatherly, L.J. Frasinski, and K. Codling, *Chem. Phys. Lett.* **149** 477 (1988).

[Iva1996] M. Yu Ivanov, T. Seideman, and P. B. Corkum, *Phys. Rev. A* **54** 1541 (1996).

[Led1997] K.W.D. Ledingham and R.P. Singhal, *Int. J. Mass Spectrom. Ion. Process.* **163** 149 (1997).

[Pur1994] J. Purnell, E.M. Snyder, S. Wei, and A.W. Castleman Jr., *Chem. Phys. Lett.* **229** 333 (1994).

[Str1992] D. T. Strickland, Y. Beaudoin, P. Dietrich, and P.B. Corkum, *Phys. Rev. Lett.* **68** 2755 (1992).

Chapter 4
Two-Fragment Correlation Experiments

The ability to measure three-dimensional ion velocities is a prerequisite for molecular imaging using half-scattering techniques. Electron self-diffraction imaging involves a single high-resolution velocity measurement for each molecular ion. Time-resolved Coulomb explosion imaging entails the simultaneous measurement of all molecular fragment velocities.

In this chapter, the PATRICK instrument's ability to measure and correlate three-dimensional ion velocities is demonstrated. As a specific example, the intense-field dissociation of molecular deuterium is used throughout. Uncorrelated D^+ velocity distributions are presented in §4.1 for both linearly and circularly polarized laser pulses. The extent to which the timing electronics limit multiple ion detection is discussed in §4.2. In §4.3, the correlated D^+ velocity distribution measured for the circularly polarized case is compared with numerically simulated data. The use of the D^+ correlation technique as a probe for "shake-off" double ionization of D_2 is described in §4.4.

4.1 Uncorrelated Velocity Measurements

A 40 μm thick molecular beam was produced within the PATRICK instrument by placing 28 mbar of D_2 behind the continuous gas reservoir's 100 μm diameter nozzle. Molecules within the beam were dissociated by single 45 fs pulses from the Ti:sapphire regenerative amplifier. A quarter-wave plate was used to select the polarization state of the laser pulses. The peak focal intensity was $\sim 1 \times 10^{15}$ W/cm^2. An 83 V/cm spectrometer field accelerated the resulting D^+ fragments toward the helical delay line anode detector. The detector impact time and

position of each D^+ ion was determined and used to calculate its initial three-dimensional velocity.

D^+ Velocity Distributions

Fig. 4.1 depicts the three-dimensional D^+ velocity distribution obtained using laser pulses linearly polarized along the spectrometer axis. The data are plotted in terms of the Cartesian velocity components (v_x,v_y,v_z) defined in §2.6. As before, the molecular beam propagates along the -*X*-direction, laser pulses propagate along the +*Y*-direction en route to the parabolic mirror,

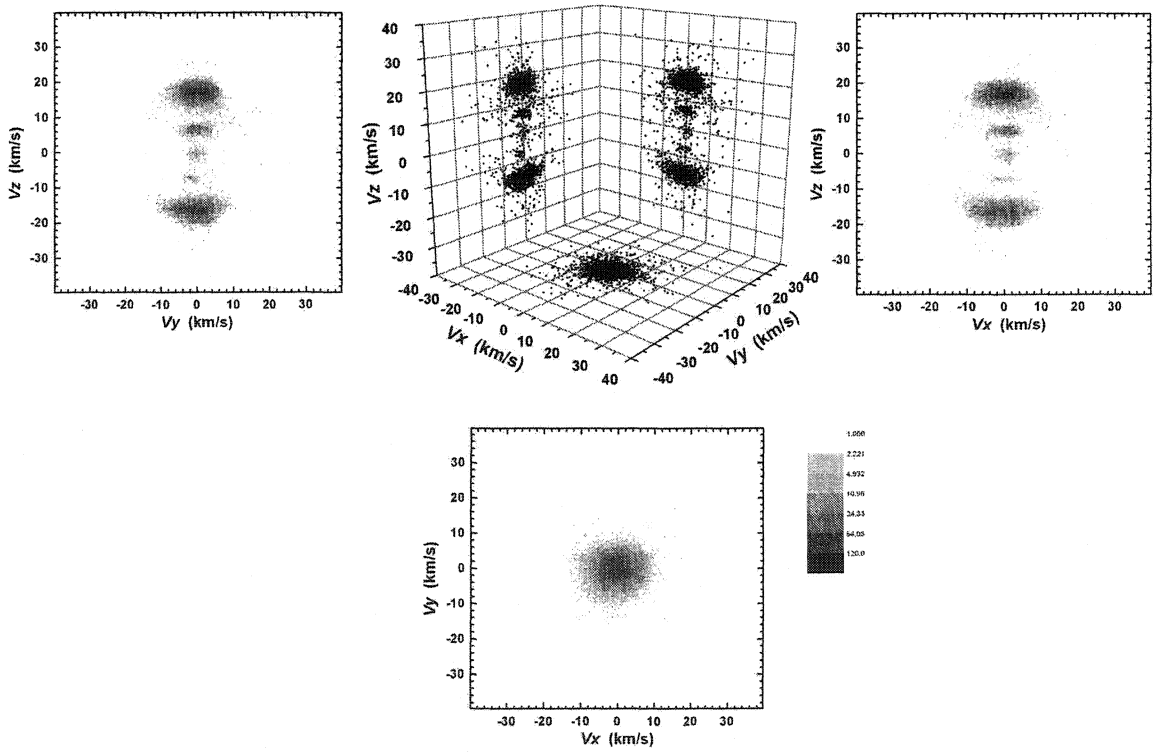

Fig. 4.1. Uncorrelated D^+ velocity distribution (linear polarization). *A representation of the three-dimensional velocity distribution of D^+ fragments arising from the strong field ionization of D_2 with linearly polarized pulses is shown. The data are plotted as two-dimensional projections of the Cartesian velocity components (v_x,v_y,v_z) onto the three coordinate planes. The X-Y and X-Z planes are parallel to the detector and polarization planes, respectively. In the corner cube plot (top centre), each black dot represents the projection of a single D^+ velocity onto a particular coordinate plane. The three intensity maps reflect the actual distribution of counts within each coordinate plane projection using a logarithmic intensity scale. D^+ fragments were preferentially ejected along the laser polarization direction (Z-axis). The clustering of the data indicates that three dissociation channels are active (i.e., low-energy ($v \approx 0$), bond softening ($v \approx 7$ km/s), and enhanced ionization ($v \approx 17$ km/s) channels).*

and the spectrometer acceleration field is along the +Z-direction. The angular distribution of the measured D^+ ion velocities about the laser polarization axis (*Y*-axis) is Gaussian (27° full angular width at half maximum). This is consistent with both theoretical [Zuo1993, Sei1995, Tal1998, DeW2000, Ton2002] and experimental [Con1996, Ell1999, Lit2003] observations that the nonresonant ionization rate for diatomic molecular ions aligned parallel to the polarization axis exceeds that for perpendicularly oriented ones. (The first experimental test of the theoretical alignment-dependent ionization rates for neutral molecules was performed within the PATRICK instrument. The results were obtained using the methodology of Chapter 6 and are described elsewhere [Lit2003].) The data's radial dependence reflects three active molecular dissociation channels: a low velocity ($v \approx 0$) $D_2 \rightarrow D^+ + D$ channel, a slightly higher velocity (~7 km/s) $D_2 \rightarrow D^+ + D$ bond softening channel [Han1975, Zav1990], and a high velocity (~17 km/s) $D_2 \rightarrow D^+ + D^+$ enhanced ionization channel [Cod1989, Sei1995, Zuo1995, Con1996].

Fig. 4.2 depicts the three-dimensional velocity distribution obtained using circularly polarized pulses. In analogy with the linear case, molecules whose axes lie within the plane of polarization ionize more efficiently than those oriented normal to it. Consequently, the velocity data are effectively confined to the polarization (i.e., *X*-*Z*) plane. The out-of-plane angular distribution is Gaussian whose full width at half maximum of 33° is comparable to the 27° angular width observed in the linear case. The relative clustering of data along the *X*=*Z* direction suggests that the laser polarization was slightly elliptical. The radial dependence of the data is consistent with the $v \approx 0$, bond softening, and enhanced ionization dissociation channels observed in the linear case.

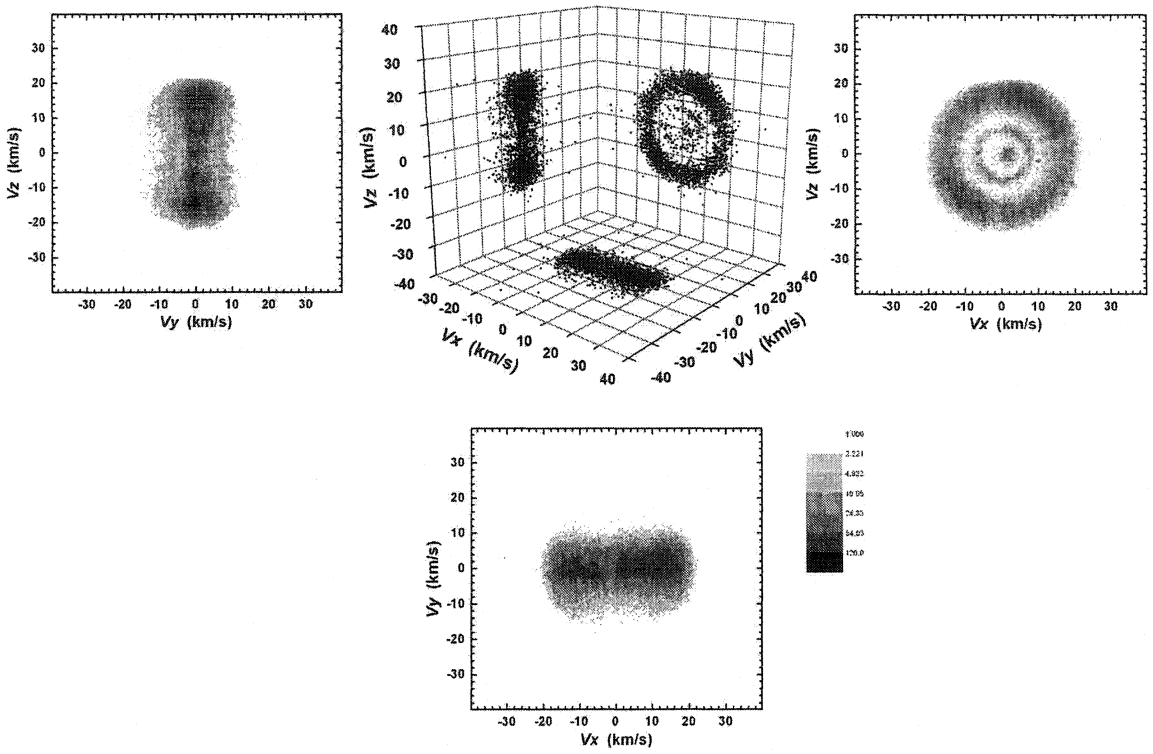

Fig. 4.2. Uncorrelated D^+ velocity distribution (circular polarization). *Depicted are two-dimensional projections of the D^+ fragment velocity distribution resulting from strong field ionization of D_2 using circularly polarized light. A low-energy dissociation channel is observed near v = 0. The bond softening ($v \approx 7$ km/s) and enhanced ionization ($v \approx 17$ km/s) channels produce concentric toroidal D^+ distributions oriented parallel to the polarization (i.e., X-Z) plane. An excess of counts along v_x=v_z suggests a slightly elliptical polarization state whose major axis was oriented along the X=Z direction.*

D^+ Kinetic Energy Spectra

The kinetic energy spectra derived from the measured velocity distributions (Figs. 4.1 and 4.2) are depicted in Fig. 4.3. The spectra for the linearly polarized (Fig. 4.3a) and circularly polarized (Fig. 4.3b) cases are nearly identical. Both spectra feature low-energy dissociation (< 0.1 eV), bond softening (~0.5 eV), and enhanced ionization (~3 eV) peaks. However, a high-energy tail (~5-10 eV) is also present in the linearly polarized data. This additional feature is due to a single nonresonant ionization step that launches a vibrational wave packet in D_2^+ [Nii2002], followed by a laser-driven recollision between the parent ion and the liberated electron [Cor1993]. The recollision cross section is a maximum for a linearly polarized pulse, decreases

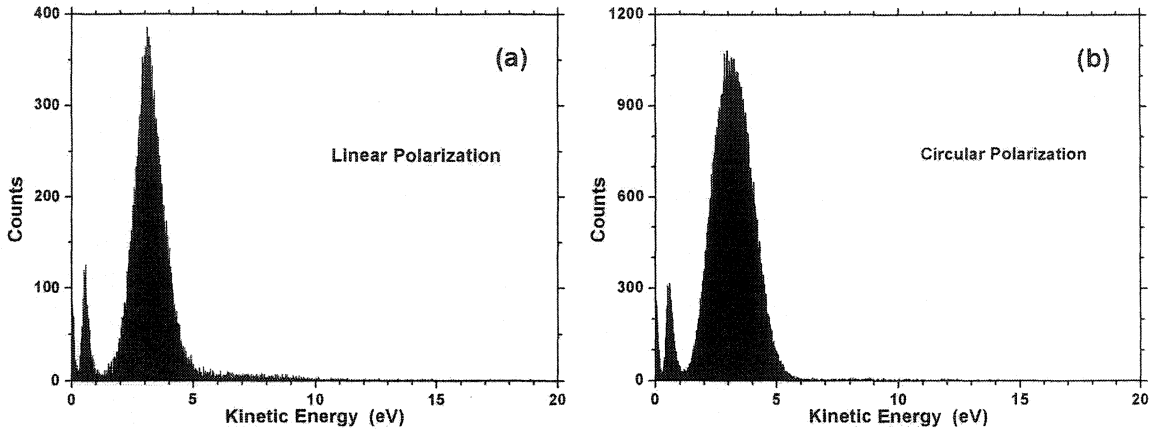

Fig. 4.3. Uncorrelated D^+ kinetic energy distributions. *The kinetic energy spectra corresponding to the D^+ velocity distributions obtained using (a) linearly and (b) circularly polarized laser pulses are shown. Both spectra feature low-energy dissociation (< 0.1 eV), bond softening (~1 eV), and enhanced ionization (~3 eV) peaks. A high-energy tail (~5-10 eV) due to electron recollision double ionization of D_2 is observed in the linear case.*

rapidly with increasing ellipticity, and is zero in the circularly polarized case. An inelastic recollision (such as $D_2^+ + e^- \rightarrow 2D^+ + 2e^-$ or $D_2^+ + e^- \rightarrow \left(D_2^+\right)^* + e^- \rightarrow 2D^+ + 2e^-$) that removes the remaining electron from D_2^+ will initiate its Coulomb explosion. In such a case, the bare molecular ion's Coulomb potential energy is equipartitioned between the D^+ nuclei and contributes to a high kinetic energy tail, such as that of Fig. 4.3a. Whereas inelastic recollisions can give rise to the observed high-energy tail (as well as high harmonic generation [Cor1993]), elastic recollisions form the basis of the electron self-diffraction approach to molecular imaging.

4.2 Detector Dead Time Effects

The PATRICK instrument's detection efficiency is independent of ion velocity and mass-to-charge ratio only when a single ion is produced per laser pulse. When two or more ions strike the detector in rapid succession, impact data may not be recorded for one or more of the ions. While such instances are typically quite rare for low density atomic beams, they can be common in Coulomb explosion experiments involving molecules that contain two or more identical atoms, molecules that produce many fragments, and those in which multiple molecules are exploded per

laser pulse. In correlation experiments that require the detection of all molecular fragments, such occurrences can significantly limit the rate at which useful data are acquired and introduce a degree of bias to the overall data set. In a time-resolved Coulomb explosion imaging experiment, this bias can be manifested as distorted branching ratios for specific Coulomb explosion channels, or as ranges of undetectable molecular orientations, bond angles, or bond lengths. By understanding the sources and consequences of the PATRICK instrument's nonuniform detection efficiency, one can design experiments that mitigate or eliminate its impact and more correctly interpret the experimental data. Proper interpretation of data is especially important in experiments that yield a "negative" result, such as the search for shake-off double ionization of D_2 described in §4.4.

There are two reasons that certain ion impacts might not be recorded when they occur in rapid succession. First, the data acquisition software (§2.6) rejects raw data that cannot be unambiguously assigned to quintuplets $(t_{mcp},t_{x1},t_{x2},t_{y1},t_{y2})$. Second, and more importantly, the pulse pair resolution (or dead time t_{dead}) of the PATRICK instrument's five constant fraction discriminators is nonzero. When activated by a current pulse, each discriminator becomes unresponsive for a period of $t_{dead} = 16\,\text{ns}$. A second current pulse arriving during that interval will fail to trigger the discriminator and the ion impact that gave rise to it will not be recorded. Constant fraction discriminators are connected to the microchannel plate holder as well as to the ends of the *X*- and *Y*-sensing delay lines. The practical consequences of the discriminator dead time on the measured ion impact time (t_{mcp}) and the anode pulse arrival times ($t_{x1},t_{x2},t_{y1},t_{y2}$) differ and are discussed in turn below.

Effect of Microchannel Plate Discriminator Dead Time

The spectrum of D^+ impact times t_{mcp} corresponding to the circularly polarized case's velocity distribution (Fig. 4.2) is shown in Fig. 4.4a. If the microchannel plate discriminator were

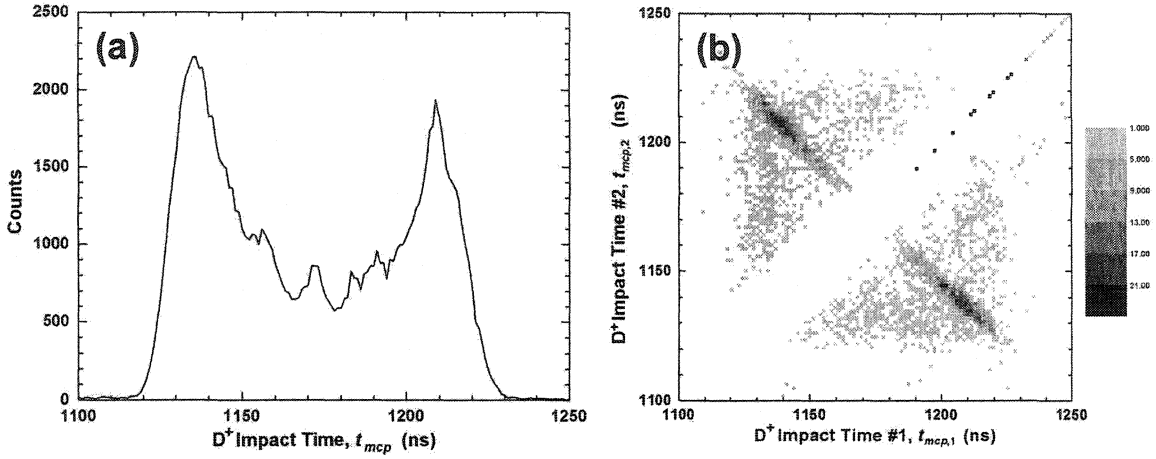

Fig. 4.4. D^+ impact time spectrum and correlation map (circular polarization). *(a) The measured spectrum of D^+ arrival times at the detector for the circularly polarized case (Fig. 4.2) is shown. (b) The correlation map corresponding to the impact time spectrum in (a) is depicted. The impact times ($t_{mcp,1}$ and $t_{mcp,2}$) of all possible D^+ pairs obtained for each laser pulse are plotted versus each other in the map. Each constituent of the broad diagonal streak (top left to bottom right) is due to a D^+ pair that originates from a single D_2 molecule. D^+ pairs that originate from two different molecules yield the map's diffuse scatter. The narrow self-correlation line (bottom left to top right) arises when a single D^+ ion's impact time is plotted against itself. The dead time of the microchannel plate discriminator results in a lack of data on either side of the self-correlation line.*

ideal (i.e., for $t_{dead} = 0$), the spectrum would be nearly symmetric about $t_{mcp} = 1172\,\text{ns}$. However, the actual discriminator's nonzero dead time results in an additional suppression of the later peak (near $t_{mcp} = 1209\,\text{ns}$). In this case, peak suppression can occur when two or more D_2 molecules are dissociated in the laser focus by a given optical pulse. Note that this scenario is statistically inevitable, even in the low molecular beam density limit. Assume that D^+ fragments from one molecule contribute to each of the peaks at $t_{mcp} = 1135\,\text{ns}$ and $t_{mcp} = 1209\,\text{ns}$. The probability of D^+ fragments arriving within a given time interval is roughly proportional to the corresponding area beneath the curve of Fig. 4.4a. Thus, the likelihood of D^+ fragments from other molecules arriving during the interval $1193\,\text{ns} < t_{mcp} < 1209\,\text{ns}$ is greater than that between $1119\,\text{ns} < t_{mcp} < 1135\,\text{ns}$ and a relative suppression of the later peak results.

The effect of the microchannel plate discriminator's dead time is even more apparent in the correlation map (Fig. 4.4b) corresponding to the D^+ impact time spectrum (Fig. 4.4a). The

map was produced by forming all possible pairs of D^+ ions recorded for each laser pulse and plotting their impact times in the form $(t_{mcp,1}, t_{mcp,2})$. The broad diagonal streak (top left to bottom right) corresponds to correlated D^+ pairs that originated from a single D_2 molecule. The diffuse off-diagonal scatter represents so-called "false" correlations and is due to D^+ ions that originated from different molecules. The narrow diagonal line (bottom left to top right) is a self-correlation artifact that results from plotting each D^+ ion's arrival time against itself. The diagonal "dead zone" which extends to either side of the self-correlation line is devoid of both true and false correlations. This is a direct consequence of the microchannel plate discriminator's dead time. The horizontal and vertical half widths of the dead zone are equal to $t_{dead} = 16$ ns.

The dead time of the microchannel plate discriminator precludes the detection of certain D^+ pairs that originate from the same D_2 molecule (Fig. 4.5). D^+ ions from a molecule oriented parallel to the detector would strike the microchannel plate simultaneously (Fig. 4.5a), generating only a single current pulse at the associated discriminator. Consequently, the data acquisition software would not record one of the D^+ impacts. If each impact were to trigger all four delay line discriminators, neither D^+ strike would be recorded since the impact position associated with the single impact time would be ambiguous. For a near-parallel D_2 molecule, the discriminator dead time precludes the detection of the second D^+ fragment if it strikes the microchannel plate less than $t_{dead} = 16$ ns after the first fragment (Fig. 4.5b). The impact times of both D^+ fragments

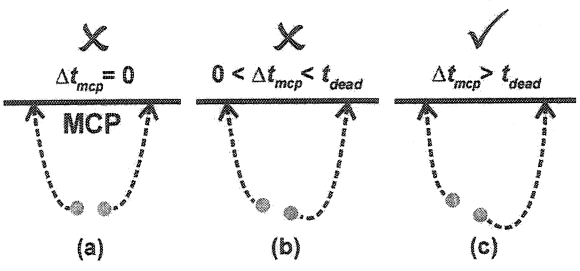

Fig. 4.5. Effect of microchannel plate discriminator dead time. *If the impact time difference Δt_{mcp} for a pair of ions does not exceed t_{dead} = 16 ns, the second ion will not trigger the microchannel plate discriminator. This precludes double ion detection when both fragments have a common mass-to-charge ratio and originate from a molecule oriented (a) parallel or (b) nearly parallel to the detector. (c) With sufficient molecular tilt, double ion detection becomes possible.*

can only be discriminated when a D_2 molecule's tilt toward the detector yields a D^+ impact time separation Δt_{mcp} that exceeds t_{dead} (Fig. 4.5c).

Effect of Delay Line Discriminator Dead Time

The practical implication of the delay line discriminators' dead time can be understood in a similar manner. The effect of this dead time only applies to certain D_2 molecules tilted somewhat more toward the detector than in the previous discussion (Fig. 4.6a). Following the Coulomb explosion of a D_2 molecule, the first D^+ ion to strike the microchannel plate produces a localized excess of electrons (Fig. 4.6b) that gives rise to a pair of counterpropagating current pulses (Fig. 4.6c) on each delay line. The process is repeated at a different location upon the arrival of the second D^+ ion (Fig. 4.6d). In order to determine the impact positions of both D^+ ions, the time separation of each similarly propagating current pulse pair (Fig. 4.6e) must exceed $t_{dead} = 16$ ns at all four delay line discriminators. Consequently, there exists a set of oblique D_2 orientations for which correlated D^+ pairs are undetectable.

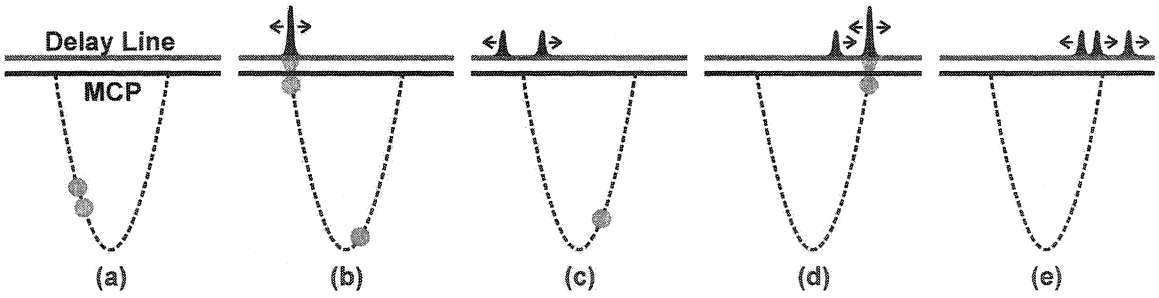

Fig. 4.6. Effect of delay line discriminator dead time. *(a) An obliquely oriented molecule fragments and the first ion impact leads to a localized concentration of charge on each delay line, as in (b). (c) A pair of current pulses propagate away from the impact location as the second ion approaches the detector. The impact of the second ion in (d) produces a second pair of counterpropagating current pulses on each delay line, as in (e). Since a discriminator is located at the ends of each delay line, the separations of all four current pulse pairs must exceed $t_{dead} = 16$ ns in order to reconstruct the impact positions of both ions.*

Simulation of D_2 Coulomb Explosion Data

Simulation software was developed by the author to confirm that experimental data obtained using the PATRICK instrument are consistent with the principles outlined in §2.5, §2.6, and §4.2. Simulated data for the Coulomb explosion of D_2 were calculated as follows and are presented in §4.3.

An ensemble of initial three-dimensional D^+ velocities was generated in spherical coordinates via a Monte Carlo approach. The ensemble's kinetic energy and angular distributions were constrained to resemble those of the experimental D^+ data obtained using circularly polarized pulses (Figs. 4.2 and 4.3a). Only the enhanced ionization channel of D_2 was simulated, hence the ensemble's kinetic energy distribution was Gaussian with a 3.14 eV peak energy and a full width at half maximum of 2.0 eV. The angle of each D^+ fragment's velocity within the polarization (i.e, *X-Z*) plane was randomly determined. The distribution of out-of-plane angles was Gaussian with a full angular width at half maximum of 33°. A correlated partner with opposite three-dimensional velocity was also generated for each D^+ ion in the ensemble.

The detector impact position and time (X,Y,t_{TOF}) for each D^+ ion were then calculated after simulating its propagation in an 83 V/cm spectrometer field. The time offset $t_0 = 145.96$ ns and spatial origin $(X_0,Y_0) = (8.93,-4.95)$ derived from the experimental data were used as inputs to the simulation.

The effects of the discriminators' dead time on the impact data were then simulated. Only those correlated D^+ ion pairs whose five associated current pulse pairs were each separated by greater than $t_{dead} = 16$ ns were retained.

The discrete 0.5 ns bin width of the time-to-digital converter channels was simulated by rounding each D^+ ion's current pulse arrival times $(t_{mcp},t_{x1},t_{x2},t_{y1},t_{y2})$ upward to the nearest half nanosecond. Using these discrete values, the detector impact position and time (X,Y,t_{TOF}) were

recalculated for each D^+ ion. The simulated three-dimensional velocity distribution was then calculated using this "pixelated" D^+ data set for comparison with the experimentally acquired data. A simulated data set was also generated for an ideal discriminator (i.e., $t_{dead} = 0$).

4.3 Correlated Velocity Measurements

In the centre-of-mass frame of a Coulomb exploded molecule, conservation of momentum requires that the electronic and ionic fragment momenta sum to zero. To a good approximation, the net momentum of the ionic fragments is also zero. Using the PATRICK instrument, this can be exploited to identify ionic fragments that originate from a particular molecule. The ability to identify such correlated fragment momenta is a prerequisite for time-resolved Coulomb explosion imaging.

Selection of Correlated D^+ Pairs

Fig. 4.7 illustrates the manner in which correlated D^+ pairs were identified amongst the velocity distribution obtained using circularly polarized light (Fig. 4.2). The total kinetic energy $E_1 + E_2$ versus the net momentum $|\mathbf{p}_1 + \mathbf{p}_2|$ for consecutive D^+ pairs within the experimental data set are depicted in Fig. 4.7a. D^+ pairs produced via the enhanced ionization channel are centred about $E_1 + E_2 = 6\,\text{eV}$. D^+ pairs that originated from a common D_2 molecule appear at low total momentum (i.e., $|\mathbf{p}_1 + \mathbf{p}_2| < 10$ atomic units; 1 atomic unit of momentum = 1.993×10^{-24} kg·m/s) whereas all other pairs represent false correlations. Fig. 4.7b depicts the subset of correlated D^+ pairs whose net momentum is less than 10 atomic units. The momentum spread within the correlated data set (Fig. 4.7b) arises from the ionization-induced recoil experienced by the D_2^{2+} ion (~4 atomic units), the distribution of longitudinal speeds within the molecular beam (~2

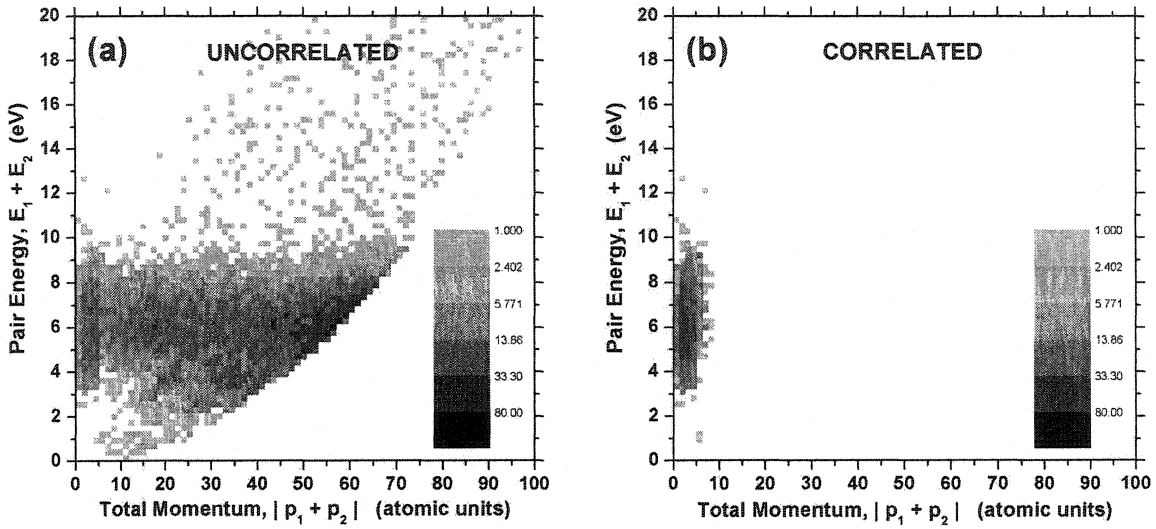

Fig. 4.7. D^+ pair energy versus net momentum (circular polarization). *The data obtained using circularly polarized light are represented according to the total energy and momentum of D^+ ion pairs. (a) The entire data set is shown. An ion pair that originates from a single D_2 molecule exhibits near-zero total momentum. A pair of ions that exhibits high total momentum originated from two different molecules and represents a false coincidence. (b) The subset of ion pairs that originated from single D_2 molecules was isolated by discarding data whose total pair momentum exceeded 10 atomic units. The retained correlated data set is shown.*

atomic units), the pixelation of the impact data introduced by the time-to-digital converter's 0.5 ns bin width (~1 atomic unit), and space charge effects.

Comparision of Experimental and Simulated D^+ Data

D^+ Impact Time Spectra

The measured and simulated D^+ data for the circularly polarized case are plotted as a function of microchannel plate impact time t_{mcp} in Figs. 4.8a and 4.8b, respectively. Fig. 4.8a depicts the measured D^+ impact time spectra for both the uncorrelated data (whose velocity distribution is shown in Fig. 4.2; upper spectrum) and the correlated data (shown in Fig. 4.7b; lower spectrum). Fig. 4.8b shows the predicted impact time spectra for correlated D^+ pairs for both ideal ($t_{dead} = 0$; upper spectrum) and actual ($t_{dead} = 16$ ns; lower spectrum) constant fraction discriminators.

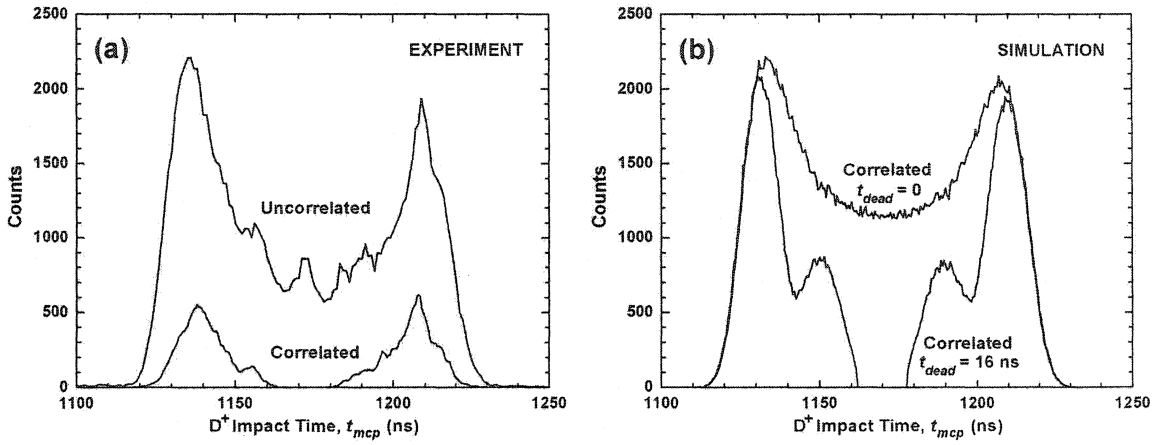

Fig. 4.8. Measured and simulated D^+ impact time spectra (circular polarization). *(a) D^+ impact time spectra recorded using circularly polarized pulses are depicted for the uncorrelated (upper plot) and correlated (lower plot) data sets. (b) Simulated D^+ impact time spectra are shown for discriminator dead times of t_{dead} = 0 (upper plot) and t_{dead} = 16 ns (lower plot). The dead zones due to the microchannel plate discriminator (near $t_{mcp} \approx 1172$ ns) and delay line discriminators (near $t_{mcp} \approx 1145$ ns and $t_{mcp} \approx 1200$ ns) are clearly evident in the correlated measured and simulated t_{dead} = 16 ns spectra.*

The uncorrelated measured spectrum (Fig. 4.8a; upper plot) strongly resembles the simulated "ideal discriminator" (i.e., $t_{dead} = 0$) spectrum (Fig. 4.8b; upper plot). The main discrepancy is near $t_{mcp} = 1172$ ns where there are fewer counts in the measured spectrum than in the simulated one. This is a consequence of the nonzero dead time of the actual discriminators.

The effects of nonzero discriminator dead times are apparent in both the correlated measured spectrum (Fig. 4.8a; lower plot) and its simulated $t_{dead} = 16$ ns counterpart (Fig. 4.8b; lower plot). No correlated D^+ impacts occur in the vicinity of $t_{mcp} = 1172$ ns in either case. Since the fragments of D_2 molecules oriented roughly parallel to the detector should arrive at $t_{mcp} \approx 1172$ ns, the absence of such counts is a consequence of the microchannel plate discriminator dead time (§4.2). Similarly, a dearth of counts is observed near $t_{mcp} \approx 1145$ ns and $t_{mcp} \approx 1200$ ns in both spectra. These features result from the delay line discriminators' inability to detect both fragments from certain obliquely oriented D_2 molecules.

The width of the simulated $t_{dead} = 16$ ns spectrum's central "dead zone" is exactly $t_{dead} = 16$ ns (Fig. 4.8b; lower plot). The number of counts increases steeply thereafter, since it is assumed that the hypothetical microchannel plate discriminator switches from an inactive to an active state instantaneously. In the correlated measured spectrum (Fig. 4.8a; lower plot), the central dead zone is also 16 ns wide, yet the number of counts increases gradually just beyond it. This suggests that the switching time of the actual discriminator is on the order of several nanoseconds.

The PATRICK instrument's single ion detection efficiency (in the absence of discriminator dead time effects) ε can be estimated using Fig. 4.8. The height of the peak near $t_{mcp} = 1135$ ns is roughly proportional to ε in the uncorrelated spectrum and ε^2 in the correlated one. Since the simulated data assume perfect detection efficiency (i.e., $\varepsilon = 1$), the peak's height is nearly equal in both the $t_{dead} = 0$ and $t_{dead} = 16$ ns spectra (Fig. 4.8b). The ratio of the peak's height in the correlated and uncorrelated measured spectra (Fig. 4.8a) suggests an actual single ion detection efficiency of $\varepsilon \approx 0.23$.

D^+ Velocity Distributions

The three-dimensional D^+ velocity distribution for the correlated measured data set (Fig. 4.9) bears a strong qualitative resemblance to its simulated $t_{dead} = 16$ ns counterpart (Fig. 4.10). In both cases, the microchannel plate discriminator's dead time precludes the detection of correlated D^+ pairs whose parent D_2 molecules were roughly parallel to the detector (i.e., *X*-*Y*) plane. Similarly, the delay line discriminators' dead time gives rise to two opposed conical dead zones in each distribution. Each conical dead zone is coaxial with the acceleration axis of the time-of-flight mass spectrometer (i.e., *Z*-axis) and prevents the detection of correlated D^+ pairs from certain obliquely oriented D_2 molecules.

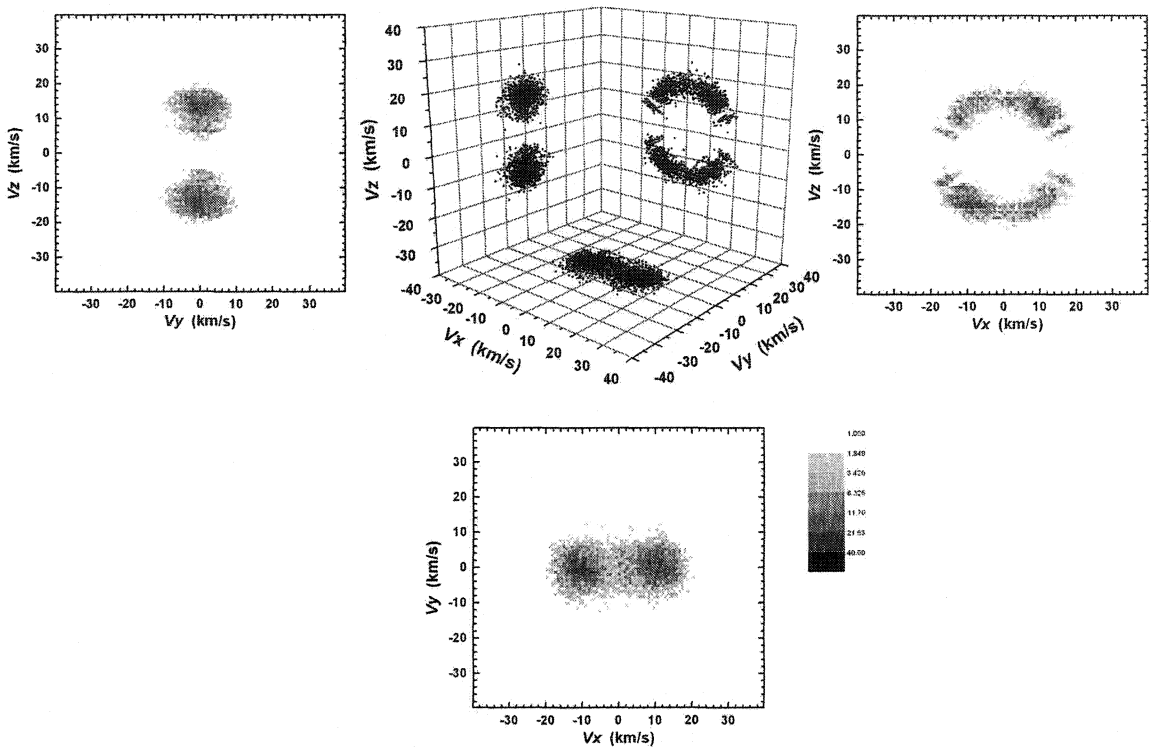

Fig. 4.9. Correlated D^+ velocity distribution (circular polarization). *Projections of the correlated data set's D^+ velocity distribution onto the three coordinate planes are shown. The $v \approx 0$ and bond softening ($v \approx 7$ km/s) dissociation channels evident in Fig. 4.2 are absent from the correlated data since each produces only one D^+ fragment per dissociated molecule. The 16 ns dead time of the five discriminators prevents the detection of some correlated D^+ pairs produced via the enhanced ionization ($v \approx 17$ km/s) channel.*

There are two key differences between the uncorrelated and correlated measured velocity distributions (Figs. 4.2 and 4.9, respectively). First, the $v \approx 0$ and bond softening ($v \approx 7$ km/s) dissociation channels do not contribute to the correlated D^+ distribution since they only produce one D^+ fragment per D_2 molecule. Second, the enhanced ionization ($v \approx 17$ km/s) channel is manifested as an unbroken torus in the uncorrelated distribution and a segmented one in its correlated counterpart.

Dead Zone Management

Dead time effects are uncommonly severe in the case of correlated D^+ pair detection. In most instances, such effects can be mitigated or eliminated altogether maximizing the difference

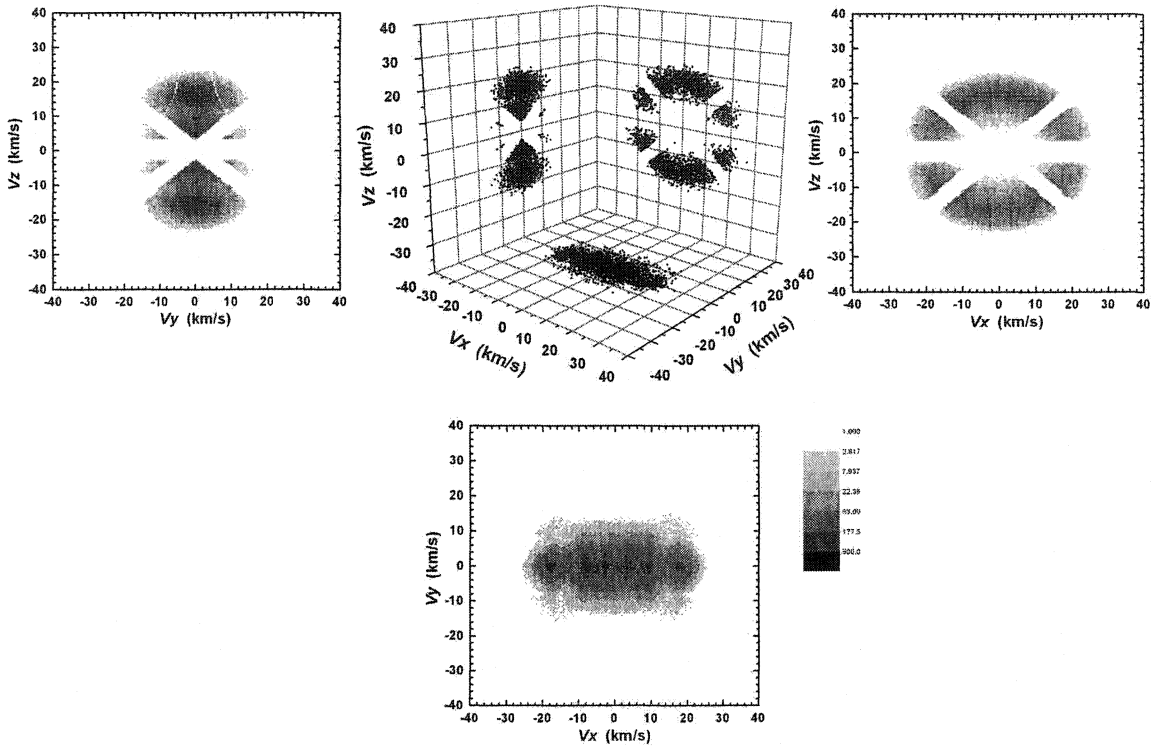

Fig. 4.10. Simulated correlated D^+ velocity distribution (circular polarization). *The simulated D^+ velocity distribution for correlated D^+ pairs and t_{dead} = 16 ns is depicted as projections onto the three coordinate planes. The simulation considers only correlated D^+ pairs produced via the enhanced ionization ($v \approx 17$ m/s) channel using circularly polarized light. A dead time of 16 ns and instantaneous switching from the inactive to the active state is assumed for all five discriminators. The simulated velocity distribution qualitatively reproduces the discriminator-induced dead zones characteristic of its experimentally determined counterpart (Fig. 4.9).*

between fragment impact times. This can be achieved in a variety of ways. By selecting a dissociation channel that yields asymmetric fragment charges (e.g. $N_2 \rightarrow N^+ + N^{2+}$) dead time effects can be completely avoided. While this is not an option for H_2 or D_2, it is readily achievable for all other diatomic molecules. When a charge-symmetric dissociation channel is required, the use of different isotopes (such as HD in place of D_2) can accomplish the same result (although it is less effective for heavier atoms). When isotopic substitution is inappropriate, increasing the total charge of the symmetric dissociation channel (e.g. by opting for $N_2^{4+} \rightarrow N^{2+} + N^{2+}$ over $N_2^{2+} \rightarrow N^+ + N^+$) would reduce the angular width of each dead zone.

Decreasing the spectrometer acceleration field would yield similar results. When Coulomb exploding linear (or slightly bent) molecules using linearly polarized pulses, orienting the polarization along the mass spectrometer's acceleration axis (i.e, *Z*-axis) should significantly mitigate or eliminate all dead time effects.

4.4 Probability of Shake-Off in D_2

In the preceding section, correlated D^+ pair detection is used to illustrate the PATRICK instrument's capacity to perform ion coincidence measurements. However, the same technique can be exploited to address a topic of longstanding interest in the field of strong field molecular physics: nonlinear "shake-off" double ionization. While a comprehensive discussion of the topic is beyond the scope of this work, a brief treatment is presented here to illustrate the PATRICK instrument's ability to perform nearly background-free studies of subfemtosecond ionization processes.

Concept

The shake-off double ionization process is an example of the sudden approximation of quantum mechanics. When an electron is removed from its parent ion so rapidly that a remaining electron cannot adiabatically adjust, the latter electron will be left in a superposition state. The superposition will include the ground and bound excited states of the parent ion as well as unbound continuum states. If the second electron's wave function collapses into a bound excited state, it is said to have been "shaken up"; if it becomes unbound, it is said to have been "shaken off".

Shake-off double ionization plays a key role in the single-photon X-ray ionization of atoms [McG1995, Sch1997]. A shake-off process was initially thought to be the principal mechanism in strong field nonsequential double ionization of helium [Fit1992]. However, the

electron recollision process [Cor1993] (that gives rise to the high-energy tail in Fig. 4.3a) was subsequently shown to be the dominant mechanism in strong field double ionization of helium [Dor1998] and other noble gases [Die1994, Bha2001]. The importance of shake-off processes in the strong field double ionization of atoms and molecules remains an open question.

Theoretical calculations suggest that the probability of shake-off double ionization in D_2 is $\sim 10^{-7}$ in the presence of a 10^{15} W/cm^2 circularly polarized laser field [Bra2003]. Furthermore, electron recollision does not occur when strong field ionization is performed using circularly polarized light (as evidenced by the lack of a high-energy tail in Fig. 4.3b). Therefore, it should be possible to observe shake-off double ionization in D_2 given a high-sensitivity detection technique.

Conservation of momentum is a powerful experimental constraint that can serve as the basis for a nearly background-free detection scheme. As demonstrated in §4.3, the constraint is sufficient to isolate D^+ pairs originating from single D_2 molecules (via the enhanced ionization channel; contrast Figs. 4.2 and 4.9). Similarly, conservation of momentum represents a strong filter against microchannel plate "dark counts" and other random noise. Moreover, since double ionization of D_2 produces correlated D^+ pairs, the approach described in §4.3 should be well suited to detect shake-off in D_2.

High kinetic energy correlated D^+ pairs are the hallmarks of double ionization due to a shake-off (or shake-up) mechanism. Shake-off ionization should yield a total kinetic energy equal to the double ionization potential of the D_2 ground state (~10 eV per fragment). Excited D_2^+ states populated via a shake-up process are expected to ionize during dissociation and yield comparable correlated D^+ fragment energies. The net result should be a high kinetic energy tail analogous to that of Fig. 4.3a.

Experiment

The output of the Ti:sapphire regenerative amplifier (45 fs duration, 500 Hz repetition rate) was circularly polarized and focused to an intensity of 1.7×10^{15} W/cm^2 within a 40 μm thick beam of D_2 molecules. To limit the likelihood of false coincidences, the molecular beam density was kept low such that an average of one D_2 molecule was exploded per six laser pulses. The mass spectrometer's acceleration field strength was 125 V/cm and the total data acquisition time exceeded 24 hours.

A total of 6.5 million D^+ fragments were detected during the course of the experiment. Of these, 5.82 million laser pulses yielded single D^+ ions, 0.68 million pulses produced D^+ pairs, and a negligible number of pulses gave rise to three or more D^+ fragments. The uncorrelated D^+ kinetic distribution is shown in Fig. 4.11a.

The net momentum **p** of each D^+ pair was calculated for those laser pulses that yielded two or more D^+ fragments (Fig. 4.11a, inset). Only those D^+ pairs with $\mathbf{p} < 10$ atomic units were

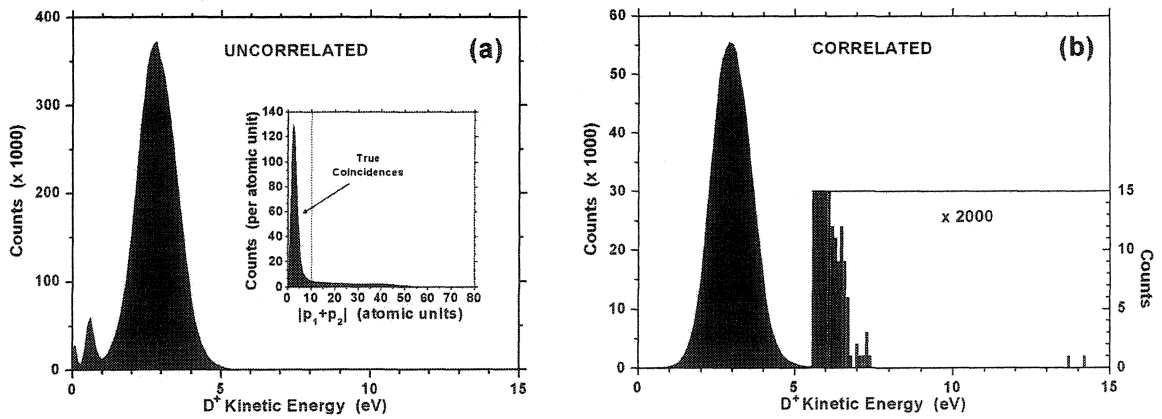

Fig. 4.11. Results of D_2 shake-off experiment. *(a) The kinetic energy spectrum of all 6.5 million detected D^+ ions is shown. The spectrum features peaks corresponding to low-energy (< 0.1 eV), bond softening (~0.5 eV), and enhanced ionization (~3 eV) dissociation channels. Inset: Histogram of total momentum $|p_1 + p_2|$ for all D^+ pairs. Those D^+ pairs with $|p_1 + p_2| < 10$ atomic units were selected to form the correlated data set. (b) The kinetic energy spectrum of the correlated data set is depicted. Only the enhanced ionization peak is present. For clarity, the vertical scale is magnified by a factor of 2000 (right axis) between 5.5 eV and 15 eV. Double ionization via a shake-off (or shake-up) process should yield ~10 eV D^+ ions, but none were observed. The lone high-energy pair's mean D^+ fragment energy (~14 eV) suggests that it is the result of a false coincidence.*

deemed to have originated from single D_2 molecules and retained.

The kinetic energy spectrum of the correlated D^+ pairs is depicted in Fig. 4.11b. No correlated D^+ fragments with fragment energies of ~10 eV were observed. The only high-energy correlated pair had an average kinetic energy of ~14 eV per fragment and was almost certainly a false coincidence.

An upper limit can be ascribed to the combined shake-off and shake-up double ionization probability of D_2 relative to the likelihood of D_2^+ production based on the quantities of ions detected. For a 45 fs, 800 nm, circularly polarized laser pulse of 1×10^{15} W/cm^2 peak intensity, the ratio of the combined shake-off and shake-up double ionization rate to the single ionization rate of D_2 is less than 1.5×10^{-6}:1.

While no shake-off or shake-up ionization was observed during the above experiment, such processes have been observed using the PATRICK instrument in conjunction with a more intense (3.2×10^{15} W/cm^2) ionization pulse. In the latter experiment, the ratio of the shake-off rate to the single ionization rate was ~10^{-5}:1.

4.5 Conclusions

The PATRICK instrument can measure the three-dimensional velocity of a single ion within a solid angle of 4π steradians and is therefore sufficient for the performance of electron self-diffraction molecular imaging. The instrument is also capable of measuring the correlated velocities of multiple molecular fragments. Conservation of momentum allows the identification of fragments that originate from a common molecule. However, the collection solid angle is somewhat less than 4π steradians unless the correlated ion impacts are sufficiently separated in time. Numerical simulations show that this limitation is due to the nonzero dead time of the instrument's five constant fraction discriminators. Nevertheless, full 4π (or near-4π) detection for

all ions can be achieved through a judicious choice of parameters in a Coulomb explosion imaging experiment. Correlated ion detection can also be employed in studies of low-probability phenomena such as intense field shake-off double ionization of molecules.

4.6 Acknowledgements

Post-doctoral fellow Igor Litvinyuk and the author jointly conducted the experiments described in this chapter. The D_2 shake-off experiment's data (Fig. 4.11) were analysed by Dr. Litvinyuk. The author performed all other analyses, including the numerical simulation of the D^+ velocity distribution.

4.7 References

[Bha2001] R. Bhardwaj, S.A. Aseyev, M. Mehendale, G.L. Yudin, D.M. Villeneuve, D.M. Rayner, M.Yu. Ivanov, and P.B. Corkum, *Phys. Rev. Lett.* **86** 3522 (2001).

[Bra2003] T. Brabec, unpublished results.

[Cod1989] K. Codling, L.J. Frasinski, and P.A. Hatherly, *J. Phys. B* **22** L321 (1989).

[Con1996] E. Constant, H. Stapelfeldt, and P.B. Corkum, *Phys. Rev. Lett.* **76** 4140 (1996).

[Cor1993] P.B. Corkum, *Phys. Rev. Lett.* **71** 1994 (1993).

[DeW2000] M.J. DeWitt, B.S. Prall, and R.J. Levis, *J. Chem. Phys.* **113** 1553 (2000).

[Die1994] P. Dietrich, N.H. Burnett, M. Ivanov, and P.B. Corkum, *Phys. Rev. A* **50** R3585 (1994).

[Dor1998] R. Dorner, H. Brauning, J.M. Feagin, V. Mergel, O. Jagutski, L. Spielberger, T. Vogt, H. Klemlichie, M.H. Prior, J. Ullrich, C.L. Cocke, and H. Schmidt-Bocking, *Phys. Rev. A* **57** 1074 (1998).

[Ell1999] Ch. Ellert and P.B. Corkum, *Phys. Rev. A* **59** R3170 (1999).

[Fit1992] D.N. Fittinghoff, P.R. Bolton, B. Chang, and K.C. Kulander, *Phys. Rev. Lett.* **69** 2642 (1992).

[Han1975] G.R. Hanson, *J. Chem. Phys.* **62** 1161 (1975).

[Lit2003] I.V. Litvinyuk, K.F. Lee, P.W. Dooley, D.M. Rayner, D.M. Villeneuve, and P.B. Corkum, *Phys. Rev. Lett.* **90** 233003 (2003).

[McG1995] J.H. McGuire, N. Berrah, R.J. Bartlett, J.A.R. Samson, J.A. Tanis, C.L. Cocke, and A.S. Schlachter, *J. Phys. B.* **28** 913 (1995).

[Nii2002] H. Niikura, F. Légaré, R. Hasbani, A.D. Bandrauk, M.Yu. Ivanov, D.M. Villeneuve, and P.B. Corkum, *Nature* **417** 917 (2002).

[Sch1997] V. Schmidt, *Electron Spectrometry of Atoms using Synchrotron Radiation*, (Cambridge University Press, Cambridge, England, 1997).

[Sei1995] T. Seideman, M.Yu. Ivanov, and P.B. Corkum, *Phys. Rev. Lett.* **75** 2819 (1995).

[Tal1998] A. Talebpour, S. Larochelle, and S.L. Chin, *J. Phys. B.* **31** L49 (1998).

[Ton2002] X.M. Tong, Z.X. Zhao, and C.D. Lin, *Phys. Rev. A* **66** 033402 (2002).

[Zav1990] A. Zavriyev, P.H. Bucksbaum, H.G. Muller, and D.W. Schumacher, *Phys. Rev. A* **42** 5500 (1990).

[Zuo1993] T. Zuo, S. Chelkowski, and A.D. Bandrauk, *Phys. Rev. A* **48** 3837 (1993).

[Zuo1995] T. Zuo and A.D. Bandrauk, *Phys. Rev. A* **52** R2511 (1995).

Chapter 5
Time-Resolved Coulomb Explosion Imaging

A fundamental assumption in any Coulomb explosion imaging experiment is that the potential surface upon which a molecule explodes will be essentially Coulombic [Vag1989]. The validity of this assumption is enhanced as the charge state of the molecular ion is increased. In an accelerator-based Coulomb explosion imaging experiment, the passage of a megaelectron-volt kinetic energy molecule through a solid target can yield a molecular ion devoid of valence electrons. Highly charged molecular ions can also be produced in laser-initiated Coulomb explosion imaging experiments since focal intensities approaching 10^{16} W/cm^2 can be readily achieved [Nis1997].

Accurate Coulomb explosion imaging also requires that nuclear motion be negligible during the multiple ionization of a molecule. This requirement is analogous to the need for fast shutter speeds in conventional motion photography. In accelerator-based Coulomb explosion imaging experiments (for which the molecular beam/foil target interaction times are ~0.1 fs), this criterion is readily met. Conversely, the need to confine nuclei inertially during molecular ionization has proven to be particularly challenging in optically triggered Coulomb explosion experiments. While relatively heavy iodine nuclei have been inertially confined using ~50 fs pulses [Str1992], significant nuclear motion occurs for lighter nuclei or when longer laser pulses are used [Cod1989, Sch1994, Sei1995, Zuo1995, Con1996]. Currently, high peak power laser pulses with durations as short as 4.5 fs can be produced [Nis1997]. Such pulses should be sufficient to confine virtually any molecule inertially during its multiple ionization.

The ability to deduce a molecule's structure from its fragmentation data is a prerequisite of any Coulomb explosion imaging experiment. While the structures of numerous small molecules and molecular ions have been determined using the accelerator-based Coulomb explosion technique, accelerator methods are ill-suited for the observation of molecular dynamics [Zaj1994]. The PATRICK instrument's ability to perform correlated two-ion measurements was illustrated in the previous chapter. In §5.2, preliminary structural images of triatomic molecules inferred from laser-initiated Coulomb explosion data are presented. Thereafter, the potential for time-resolved Coulomb explosion imaging of molecular dynamics is illustrated in §5.3 using the results of two pump-probe experiments.

5.1 Inertial Confinement of Nuclei

Molecules that contain low-mass nuclei are the most difficult to confine inertially during ionization. This is particularly true of molecules that contain the lightest nuclei (H^+ and D^+) whose motion proceeds on a timescale of just a few femtoseconds. For example, the fundamental vibrational periods of H_2, D_2, and the ubiquitous C-H bond of organic chemistry are 7.6 fs, 10.7 fs, and 11.7 fs, respectively. Nevertheless, accurate Coulomb explosion imaging of virtually any small polyatomic molecule should be possible using existing femtosecond laser technology. To this end, numerical simulations [Che1999] suggest that the structure of H_2^+ can be accurately imaged (for low vibrational states) using ~5 fs laser pulses (linearly polarized, 800 nm wavelength, 4×10^{15} W/cm^2 peak intensity). The calculations also show that the fidelity of structural images improves significantly as the masses and charge states of Coulomb explosion fragments increase. Moreover, the experiments described in this section demonstrate that near-total confinement of D_2 can be achieved during its double ionization with such pulses.

Inertial Confinement and the D_2 Molecular Clock

The degree of structural deformation (or lack of confinement) experienced by a molecule during its multiple ionization is directly related to the elapsed time between the first and final ionization steps. In the D_2 experiments described here (Fig. 5.1) and elsewhere [Lég2003], this time difference can be determined from the D^+ Coulomb explosion fragments using the "molecular clock" concept [Nii2002].

The double ionization and subsequent Coulomb explosion of D_2 were accomplished using a single, intense laser pulse. The removal of the first electron launched a vibrational wave packet in the resulting D_2^+ ion (Fig. 5.1). Prior to the second ionization step, the wave packet's propagation led to a stretching of the molecular ion that reduced its Coulomb potential energy. The removal of the second electron produced a bare D_2^{2+} ion that underwent Coulomb explosion. The asymptotic total kinetic energy of the D^+ fragments equalled the D_2^+ ion's Coulomb potential energy during the second ionization step. Consequently, the extent to which the molecule was inertially confined during the double ionization could be directly measured. By modelling the

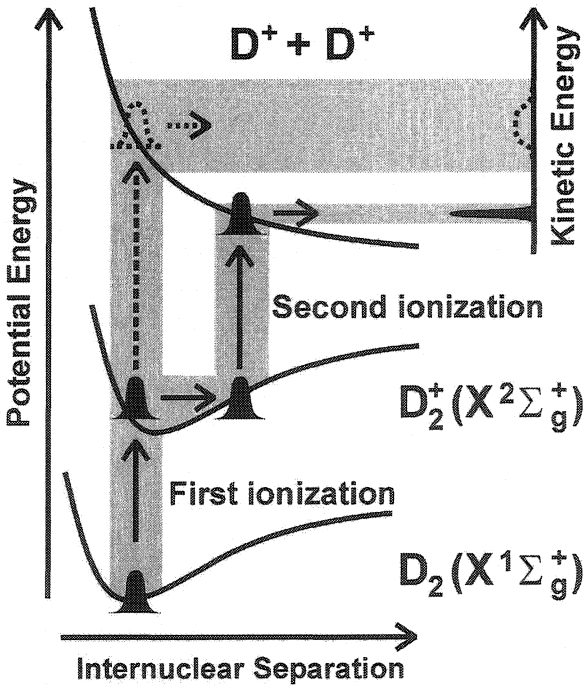

Fig. 5.1. D_2 molecular clock. *The first ionization of D_2 launches a vibrational wave packet in D_2^+. If the second ionization occurs immediately afterward (dotted arrows), the kinetic energy of the D^+ fragments will equal the Coulomb potential energy of the D_2 ground state. Otherwise (solid arrows), the wave packet will propagate, the second ionization will occur at a larger internuclear separation, and the kinetic energy of the D^+ fragments will be reduced. The time delay between the first and second ionization steps can be inferred from the difference between the D_2 Coulomb potential energy and the total D^+ fragment energy.*

propagation of the D_2^+ wave packet, the elapsed time between ionization steps was also determined.

Experimental Configuration

The D_2 confinement experiments were performed using the output of the Ti:sapphire regenerative amplifier (40 fs duration, 500 Hz repetition rate). Shorter pulses were produced via self-phase modulation in a hollow fibre (250 μm inner diameter, 1 m long) containing 1 atm of argon [Nis1997]. The fibre's output was compressed by a pair of chirped dielectric mirrors and characterized using the SPIDER technique [Iac1998]. The compressed pulses had a minimum duration of 8.6 fs and were linearly polarized. When required, circular polarization was achieved using an achromatic quarter-wave plate. Of each pulse's total energy, 84% and 95% were contained within the main peak and a 100 fs window, respectively.

The 40 μm thick molecular beam was produced by expanding 25 mbar of D_2 through the continuous gas reservoir's 100 μm diameter nozzle. The laser pulses were focused to a diameter of ~5 μm at the centre of the D_2 beam by the PATRICK instrument's parabolic mirror. The intensity experienced by molecules was nearly uniform along the laser propagation direction since the laser focus' ~100 μm confocal parameter exceeded the molecular beam width. D^+ ions were collected by the 100 V/cm spectrometer acceleration field and analysed using the helical delay line anode detector. Each D^+ ion's three-dimensional velocity and kinetic energy were calculated from the impact data.

Results and Discussion

The D^+ kinetic energy spectra obtained using linearly polarized, 5×10^{14} W/cm^2 peak intensity laser pulses of two different durations (40 fs and 8.6 fs) are depicted in Fig. 5.2. The 40 fs data (Fig. 5.2a) are analogous to those of Figs. 4.3a and 4.11a. The spectrum contains peaks

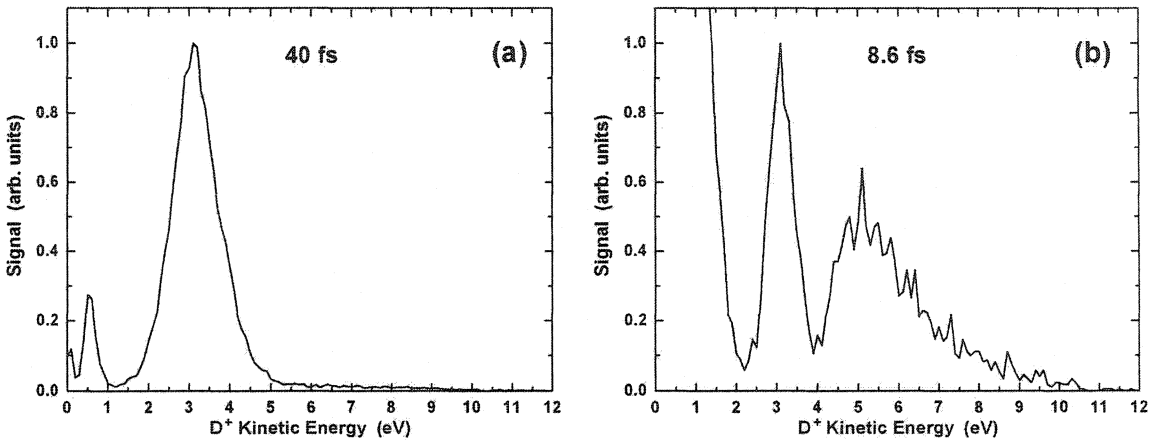

Fig. 5.2. D^+ kinetic energy spectra: effect of pulse duration. *Kinetic energy spectra for D^+ fragments arising from the intense-field dissociation of D_2 are shown. The data were obtained using linearly polarized pulses of 5 × 10^{14} W/cm^2 peak intensity and durations of (a) 40 fs and (b) 8.6 fs. Features associated with low-energy (< 0.1 eV), bond softening (~0.5 eV), enhanced ionization (~3 eV), and electron recollision (~5-10 eV) dissociation channels occur in both spectra. An additional peak (~5 eV) due to sequential double ionization of D_2 is present in the 8.6 fs pulse data. Each spectrum has been normalized to the height of its enhanced ionization peak.*

corresponding to low-energy (< 0.1 eV), bond softening (~0.5 eV) [Han1975, Zav1990], and enhanced ionization (~3 eV) [Cod1989, Sei1995, Zuo1995, Con1996] dissociation channels as well as a high-energy (~5-10 eV) tail due to electron recollision [Cor1993]. All of these features are present in the 8.6 fs spectrum (Fig. 5.2b) along with an additional "sequential ionization" peak near 5 eV.

The enhanced ionization peak, the sequential ionization peak, and the high-energy tail of Fig. 5.2 each arise from doubly ionized D_2 and illustrate the molecular clock concept. During the enhanced ionization process, the second ionization step occurs at a "critical internuclear distance" of ~2.3 Å corresponding to an asymptotic kinetic energy of ~3.1 eV per deuteron. The sequential peak's ~5 eV fragment energy suggests that the second electron's removal occurred at an internuclear separation of ~1.4 Å, before the D_2^+ wave packet reached the critical distance for enhanced ionization. Similarly, the ~5-10 eV high-energy tail indicates that electron recollision can remove the D_2^+ ion's remaining electron even earlier during the wave packet's propagation, over a range of shorter internuclear separations (~0.7-1.4 Å).

These results have an important implication for laser-initiated Coulomb explosion imaging experiments. Whereas the enhanced ionization peak dominates the 40 fs spectrum (Fig. 5.2a), the 8.6 fs pulse can ionize D_2^+ at shorter internuclear separations to yield higher energy fragments (Fig. 5.2b). Thus, for a given peak intensity, better nuclear confinement (and hence more accurate molecular imaging) can be achieved by shortening the duration of the ionizing pulse.

The polarization dependence of the D^+ fragment energy is depicted in Fig. 5.3. The data were obtained using 10.5 fs pulses of equal electric field amplitude, corresponding to respective peak intensities of 5×10^{14} W/cm^2 and 7×10^{14} W/cm^2 for the linearly and circularly polarized cases. The high-energy tail is absent from the circularly polarized spectrum (Fig. 5.3b) since electron recollision does not occur. Consequently, the D_2^+ cations ionized via electron recollision at short internuclear separations in the linear case (Fig. 5.3a) are available for sequential ionization at intermediate separations in the circular case. Thus, the lack of electron recollision in the circular case augments the sequential ionization peak versus its enhanced ionization

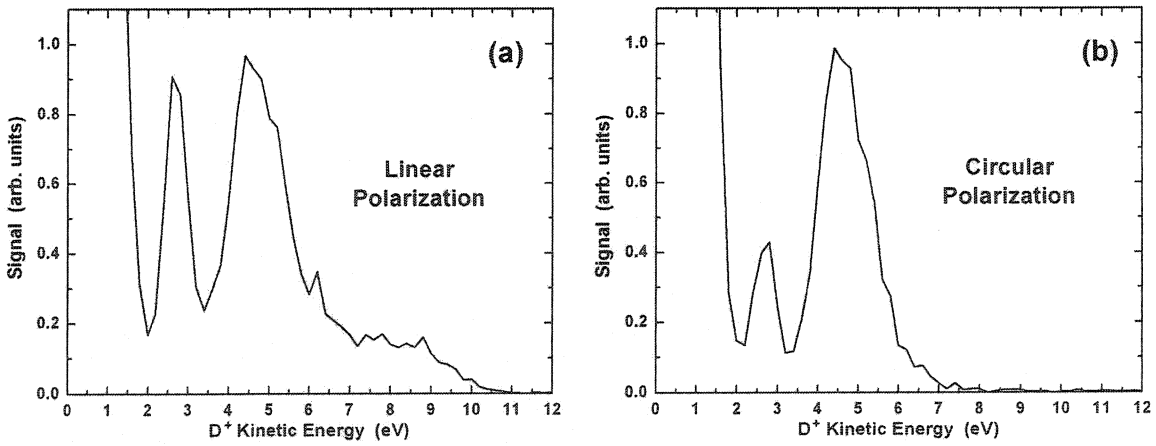

Fig. 5.3. D^+ kinetic energy spectra: effect of pulse polarization. *Depicted are D^+ kinetic energy spectra obtained using (a) linearly and (b) circularly polarized 10.5 fs pulses of equal electric field amplitude. The peak focal intensity was 5×10^{14} W/cm^2 and 7×10^{14} W/cm^2 in the linear and circular cases, respectively. The height of its sequential ionization (~4.5 eV) peak has been normalized in each spectrum. In the circularly polarized case, the enhanced ionization (~3 eV) peak is partially suppressed whereas the high-energy (~5-10eV) tail characteristic of electron recollision is absent.*

counterpart (Fig. 5.3b).

The dependence of the D^+ kinetic energy spectrum's sequential ionization peak on pulse intensity is depicted in Fig. 5.4. Measured and simulated data for circularly polarized 10.5 fs pulses with peak intensities of 1.2×10^{15} W/cm^2 (filled circles) and 2.8×10^{15} W/cm^2 (hollow circles) are presented in Figs. 5.4a and 5.4b, respectively. Despite several simplifying assumptions [Lég2003], the model calculation reproduces the trend of the experimental data. That is, as the pulse intensity is increased, the sequential ionization peak shifts to higher energy and better nuclear confinement is achieved. This is to be expected, since increasing the pulse intensity steepens the leading edge of the optical pulse and shortens the elapsed time between the first and second ionization steps.

The elapsed time between the first and second electron removals can be inferred using the simulated D_2 molecular clock. The model's predicted D_2 sequential ionization peak is plotted in Fig. 5.5a for ionization time delays of one and two optical periods (~2.7 fs and 5.3 fs, respectively). The measured sequential ionization peak obtained using linearly polarized, $2.8 \times$

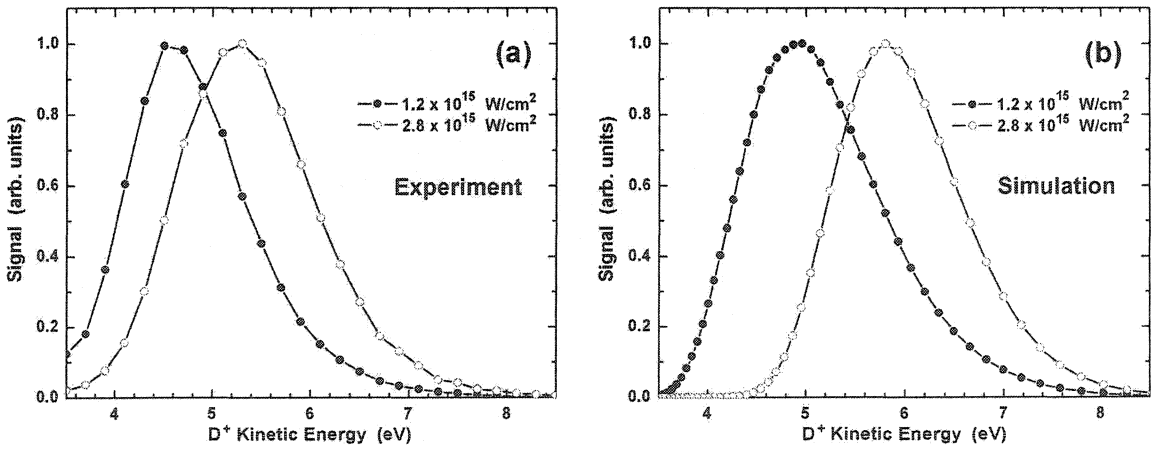

Fig. 5.4. D^+ kinetic energy spectra: effect of pulse intensity. *(a) Measured D^+ kinetic energy spectra in the vicinity of the sequential D_2 double ionization peak are depicted. The data were obtained using 10.5 fs circularly polarized pulses with peak intensities of 1.2×10^{15} W/cm^2 (filled circles) and 2.8×10^{15} W/cm^2 (hollow circles). (b) The corresponding calculated spectra are shown. In both (a) and (b), the sequential ionization peak shifts to higher energy as the peak intensity is increased.*

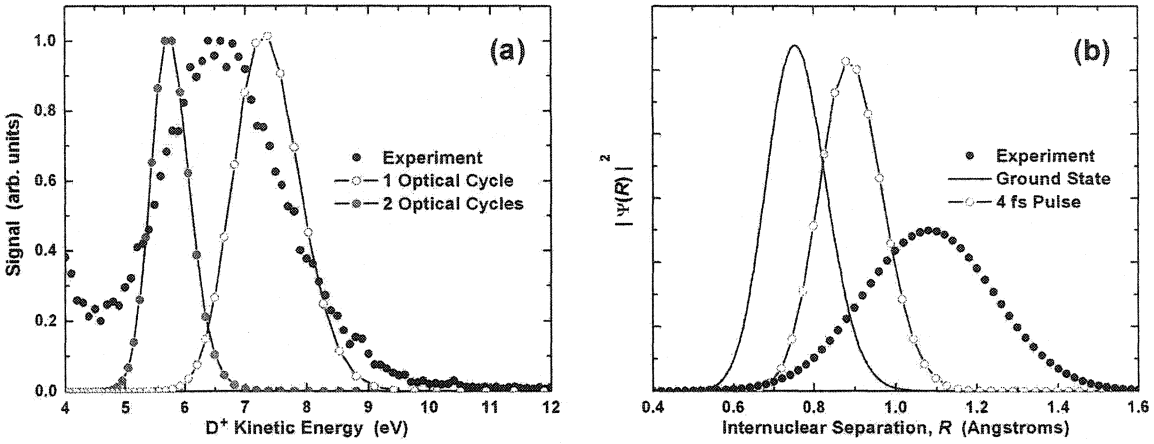

Fig. 5.5. Timing D_2 sequential ionization. *Calculated D^+ kinetic energy spectra are shown that correspond to time delays of one optical cycle (2.7 fs; hollow circles) and two optical cycles (5.3 fs; grey circles) between the sequential removal of the first and second electrons from D_2. The measured spectrum (black circles) suggests that the second electron is removed ~4 fs (i.e., 1.5 optical cycles) after the first when a linearly polarized 8.6 fs pulse of 2.8 × 10^{15} W/cm^2 peak intensity is used. (b) The calculated probability density of the D_2 wave function as a function of internuclear separation is depicted for (a) instantaneous double ionization (solid line) and (b) Coulomb explosion imaging using a 4 fs pulse (hollow circles). The probability density distribution derived from the measured D^+ kinetic energy spectrum in (a) is also shown (8.6 fs pulse duration; black circles). The data demonstrate that fidelity of a Coulomb explosion image improves as the delay time between sequential ionizations is decreased.*

10^{15} W/cm^2 peak intensity, 8.6 fs pulses is also shown (black dots). The intermediate position of the measured peak implies that ~4 fs (~1.5 optical periods) elapsed between the first and second ionization steps.

Fig. 5.5b illustrates the extent to which D_2 can be inertially confined during its double ionization with currently available laser pulses. The inversion [Che1999] of the measured D^+ kinetic energy spectrum of Fig. 5.5a (Fig. 5.5b, black dots) yields a mean D_2 bond length of ~1.1 Å. This value is ~50% greater than the 0.74 Å mean internuclear separation predicted for instantaneous double ionization of D_2 (solid line). The predicted bond length distribution (hollow circles) for state-of-the-art (linearly polarized, 5.6 × 10^{15} W/cm^2 peak intensity, 4 fs duration) pulses is centred about 0.90 Å. This represents an error of 0.16 Å (~22%) and suggests that relatively good confinement of D_2 is achievable using existing laser technology. Since heavier

nuclei move more slowly, it should be possible to confine virtually any molecule inertially using such pulses.

5.2 Structural Imaging of Triatomic Molecules

Preliminary structural images of ground state D_2O and SO_2 obtained using the PATRICK instrument are presented in this section. Coulomb explosion imaging was performed using few-cycle laser pulses generated via compression of the hollow core fibre's output [Nis1997]. The mass spectrometer's acceleration field strength (67 V/cm for D_2O, 208 V/cm for SO_2) was selected to ensure that all molecular fragments impinged upon the helical delay line anode detector. Three-dimensional fragment momenta were calculated for ions that might have originated from a specific Coulomb explosion channel (either $D_2O^{4+} \rightarrow O^{2+} + D^+ + D^+$ or $SO_2^{8+} \rightarrow S^{3+} + O^{2+} + O^{3+}$). Conservation of momentum was then applied to ensure that fragments produced via the desired explosion channel originated from the same parent molecule.

An iterative algorithm was used to infer structural information from the correlated fragment data. The algorithm assumes an initial set of nuclear positions and calculates the asymptotic momentum of each molecular fragment, based on the specified Coulomb explosion channel. The discrepancy between the measured and assumed fragment momenta is then assessed. If the discrepancy exceeds a specified tolerance, a different molecular structure is assumed and the cycle repeats. Otherwise, the algorithm terminates and the assumed structure is attributed to the molecule that produced the three detected fragments.

The Structure of D_2O

The structure of ground state D_2O was imaged using single linearly polarized, 800 nm wavelength, 8 fs duration pulses of 5×10^{15} W/cm^2 peak intensity. The polarization axis was oriented along the mass spectrometer axis in order to maximize the difference in D^+ detector

impact times. This arrangement mitigated detector dead time effects and enhanced the rate at which O^{2+}-D^{+}-D^{+} coincidences were observed.

The measured structure of D_2O retrieved via the $D_2O^{4+} \rightarrow O^{2+} + D^{+} + D^{+}$ explosion channel (Fig. 5.6) is somewhat more elongated (~1.3 Å mean O-D bond length) and linear (~119° mean bond angle) than the known ground state structure (0.96 Å bond length, 104.5° bond angle). These discrepancies are due in part to the slightly non-Coulombic nature of the D_2O^{4+} parent ion's potential surface. The main source of error, however, is the imperfect confinement of the low-mass deuterium nuclei during the ionization process. As in the case of D_2 (§5.1), significant D^{+} motion during ionization yields a measured bond length that exceeds the known value. The excessive measured bond angle is also attributable to imperfect D^{+} confinement, for two reasons. First, the deuterons will shift toward a more linear configuration during the interval between the first and second electron removals since the bond angle of D_2O^{+} exceeds that of D_2O. Second, (in

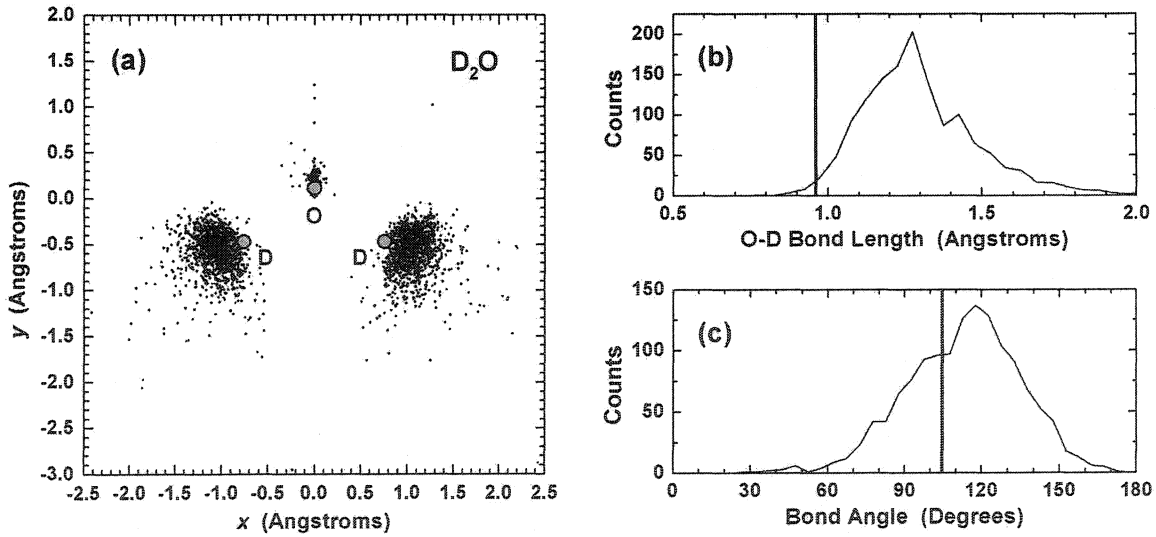

Fig. 5.6. Measured structure of D_2O. *(a) The positions of the constituent atoms of D_2O measured using laser-initiated Coulomb explosion imaging are shown (black dots). Grey circles indicate the equilibrium atomic positions within each ground state molecule. The atomic positions (x,y) are plotted in the plane of each molecule, within the centre-of-mass frame, such that the y-axis bisects the angle formed by the O-D bonds. Also shown are histograms of the measured (b) O-D bond lengths and (c) D-O-D bond angle. The equilibrium O-D bond length (0.96 Å) and bond angle (104.5°) of D_2O are indicated by thick vertical lines in (b) and (c).*

analogy with the laser-induced molecular alignment of Chapter 6) a strong linearly polarized laser field induces an oscillatory polarization of D_2O (as well as D_2O^+). For the stated experimental geometry, this will deform the molecule toward a linear geometry. As in the case of D_2, the use of shorter or more energetic laser pulses should enhance the fidelity of the Coulomb explosion image.

Previously, a different momentum-imaging technique [His1998] has been used to perform analogous structural measurements of H_2O via the $H_2O^{4+} \rightarrow O^{2+} + H^+ + H^+$ explosion channel [San1999]. Using longer (50 fs), more intense (3×10^{16} W/cm^2) linearly polarized laser pulses, a mean 2 Å O-H bond length and saturated 130°-180° H-O-H bond angle were observed, indicating that the molecule underwent severe deformation during its multiple ionization. While H_2O is somewhat harder to confine than D_2O, the measured 1.3 Å O-D bond length and 119° D-O-D bond angle suggest that the degree of confinement achieved in the latter case was relatively good.

The Structure of SO_2

Linearly polarized, ~5×10^{15} W/cm^2 peak intensity, sub-8 fs duration laser pulses were used to image the ground state structure of SO_2. The high total charge of the selected $SO_2^{8+} \rightarrow S^{3+} + O^{2+} + O^{3+}$ dissociation channel ensured that the molecular explosion proceeded on a nearly Coulombic potential energy surface. The specified fragment charge states provide unique mass-to-charge ratios (of 10.7 amu/e, 8.0 amu/e, and 5.3 amu/e, respectively) that maximize the triple fragment coincidence rate by effectively eliminating detector dead time effects.

The measured SO_2 structural data (Fig. 5.7) yield a mean S-O bond length of ~1.7 Å and a ~122° mean bond angle that closely approximate the respective known ground state values of 1.43 Å and 119.5° [Mor1964]. These results compare favourably with the values of 3.3 Å and

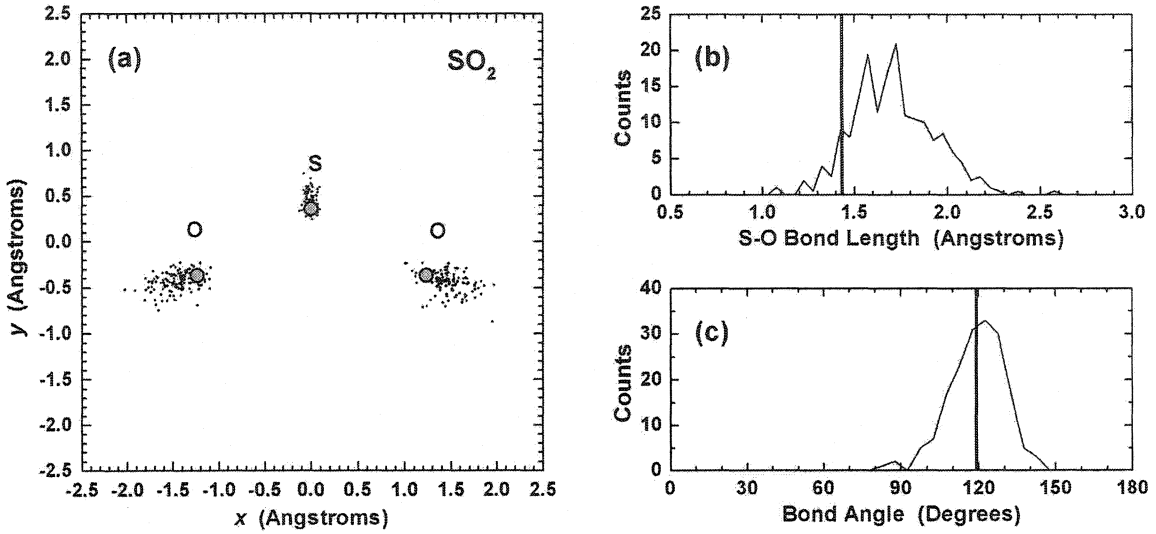

Fig. 5.7. Measured structure of SO_2. *(a) The measured (black dots) and equilibrium (grey circles) positions of the atomic constituents of SO_2 are shown using the coordinate system of Fig. 6.6a. The measured S-O bond lengths and O-S-O bond angle are histogrammed in (b) and (c), respectively. The respective equilibrium bond lengths and bond angle are 1.43 Å and 119.0°.*

130° measured using an alternative Coulomb explosion-based momentum-imaging technique (linearly polarized, 5.4 × 10^{15} W/cm^2 peak intensity, 52 fs pulses; $SO_2^{7+} \rightarrow S^{3+} + O^{2+} + O^{2+}$ explosion channel) [His1998].

A comparison of the measured D_2O and SO_2 structures (Figs. 5.6a and 5.7a, respectively) underscores the importance of inertial confinement to Coulomb explosion imaging. The good inertial confinement afforded by SO_2's relatively heavy oxygen nuclei yield discrepancies of ~19% in bond length and ~3° in bond angle. In contrast, the corresponding values for the lighter D_2O molecule are ~35% and ~15°.

5.3 Time-Resolved Measurements

In the preceding sections, a single laser pulse was used to image the ground state structures of D_2, D_2O, and SO_2. Such structural imaging could also be accomplished via accelerator-based Coulomb explosion imaging [Vag1989]. However, the optical technique's principal advantage is that structural imaging can be performed by the second pulse in a pump-

probe experiment. Consequently, the marriage of laser-initiated Coulomb explosion imaging and pump-probe techniques should enable the observation of molecular dynamics.

Currently, such time-resolved Coulomb explosion imaging experiments are being conducted with the PATRICK instrument. Preliminary data for the propagation of a vibrational wave packet in D_2^+ are described below. Unfortunately, an analogous time-sequence of structural images is not yet available for a triatomic molecule. Nevertheless, a set of time-resolved kinetic energy spectra for SO_2 is presented here to illustrate the fact that such images shall soon be forthcoming.

Observation of D_2^+ Vibrational Wave-Packet Dynamics

In the first pump-probe experiment, a vibrational wave packet was launched in D_2^+ and imaged at several moments during its time evolution. The experimental concept is analogous to the D_2 molecular clock (Fig. 5.1), save that here the pump pulse starts the clock and the probe pulse stops it. In physical terms, the pump pulse removes the first electron from D_2 whereas the probe pulse (~2×10^{15} W/cm^2 peak intensity) removes the second. Both pulses had durations of less than 8 fs and were linearly polarized. The resulting D^+ fragments were collected using an 83 V/cm acceleration field and detected using the helical delay line anode.

The correlated D^+ fragment energies are plotted in Fig. 5.8a as a function of pump-probe delay. In Fig. 5.8b, the kinetic energy data have been inverted to yield the measured spatial dependence of the D_2^+ wave packet's probability density at each delay. The data reflect the wave packet's propagation on the D_2^+ potential surface from the inner turning point (0 fs) to the outer one (~14 fs). Thereafter, the wave packet subdivides. After a delay of ~29 fs, most of the probability density returns to the inner turning point while a small fraction of the wave packet continues to dissociate. Analogous predissociative wave packet behaviour has previously been observed on a much longer timescale in IBr using pump-probe spectroscopy [Vra1996].

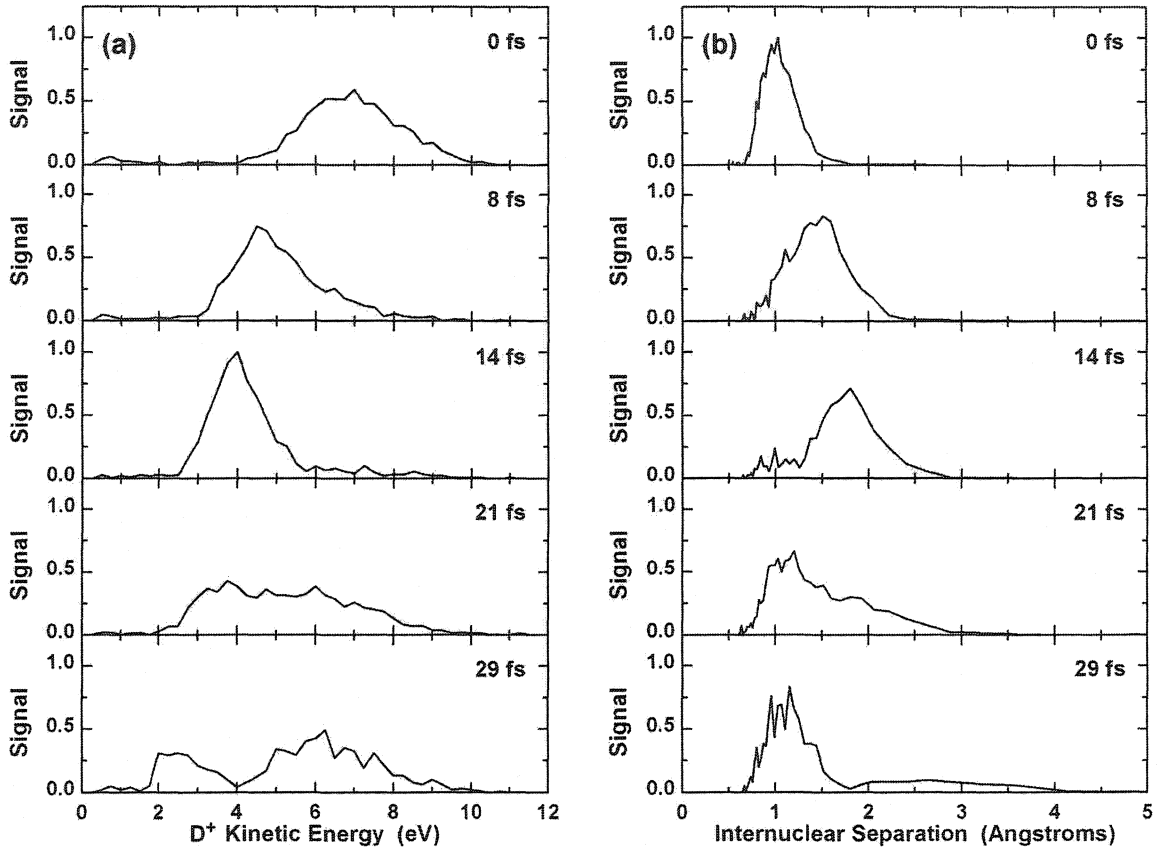

Fig. 5.8. Observed vibrational wave-packet dynamics in D_2^+. *A vibrational wave packet was launched in D_2^+ using a sub-8fs pulse and imaged via Coulomb explosion with a more intense, delayed pulse. The resulting (a) asymptotic D^+ fragment energies and (b) corresponding D_2^+ internuclear separation are depicted as a function of pump-probe delay (0-29 fs). The data span one period of the wave packet's oscillation between the inner (0 fs and ~29 fs) and outer (~14 fs) turning points of the molecular ion's potential. Following the wave packet's arrival at the outer turning point, some signal was observed at progressively larger internuclear separations (i.e., >2.5 Å). This is consistent with a branching of the wave packet into oscillatory and dissociative components at the outer turning point.*

Preliminary Measurements of SO_2^+ Vibrational Wave-Packet Dynamics

In the second pump-probe experiment, a vibrational wave packet was launched in SO_2^+ and Coulomb exploded at various delay times. The durations of the pump and probe pulses were less than 8 fs. The peak intensity of the latter pulse was ~2×10^{15} W/cm^2. To mitigate detector dead time effects, both pulses were polarized parallel to the axis of the mass spectrometer. Molecular fragments were collected 208 V/cm acceleration field and detected using the helical delay line anode.

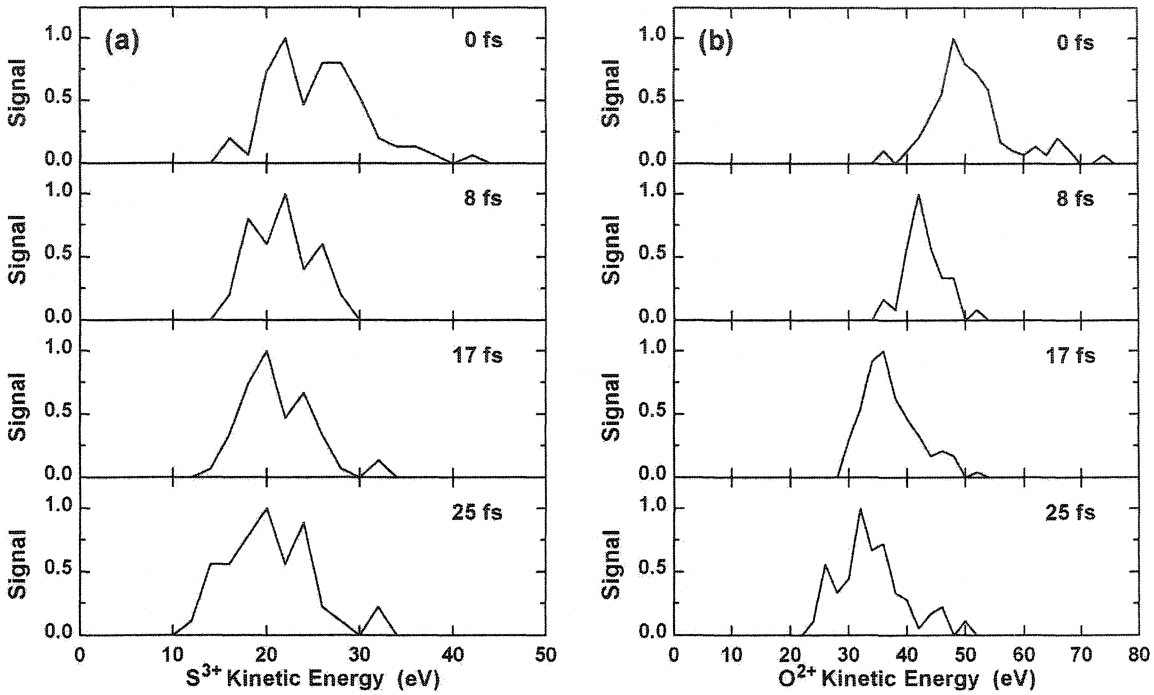

Fig. 5.9. Delayed Coulomb explosion of SO_2^+. *The kinetic energies of the ionic (a) sulphur and (b) oxygen Coulomb explosion fragments of $SO_2^{7+} \rightarrow S^{3+} + O^{2+} + O^{2+}$ are depicted as a function of pump-probe delay. The fragment energies decrease with increasing pump-probe delay, indicating a net stretching and/or straightening of the molecule.*

The correlated fragment energies originating from the $SO_2^{7+} \rightarrow S^{3+} + O^{2+} + O^{2+}$ explosion channel are plotted as a function of pump-probe delay in Fig. 5.9. As the wave packet evolved, the mean kinetic energies of the S^{3+} and O^{2+} fragments decreased. This was due to an elongation of the molecular ion rather than a bending motion, since the angle between the O^{2+} fragment momenta was independent of pump-probe delay. Moreover, the molecular ion stretched symmetrically, since the O^{2+} spectra did not become double-peaked for large pump-probe delays. Time-resolved structural images of the evolving wave packet will be obtained during the PATRICK instrument's next round of experiments.

5.4 Conclusions

The ongoing development of time-resolved Coulomb explosion imaging offers significant promise for the observation of molecular dynamics. Using few-cycle pulses,

respective good and very good degrees of inertial confinement have been demonstrated for low- and moderate-mass nuclei. With state-of-the-art laser pulses, excellent confinement of virtually any molecule should be possible. First-generation retrieval algorithms already yield reasonable structural images for highly ionized, well-confined molecules. The time-dependent kinetic energy spectra of §5.3 suggest that the realization of time-resolved structural imaging is imminent.

Thus far, structural imaging of triatomic molecules has been performed. Since the PATRICK instrument can characterize a maximum 16 ion impacts per laser pulse, it should be possible to image molecules with several more atomic constituents. For such experiments to be feasible, they must be carefully designed to achieve significant multiple-ion coincidence rates. Furthermore, a Coulomb blockade phenomenon [Ima1994] is likely to impede the removal of multiple electrons during a single optical cycle. Consequently, the use of circularly polarization is likely to become ever more important as pulse intensities and the number of atoms per molecule increase.

5.5 Acknowledgements

During the preparation of my thesis, doctoral candidate François Légaré and post-doctoral fellow Igor Litvinyuk assumed primary responsibility for the development of time-resolved Coulomb explosion imaging. Although I participated fully in the design of the experiments described in this chapter, they collected the data presented here.

5.6 References

[Che1999] S. Chelkowski, P.B. Corkum, and A.D. Bandrauk, *Phys. Rev. Lett.* **82** 3416 (1999).

[Cod1989] K. Codling and L.J. Frasinski, *J. Phys. B* **22** L321 (1989).

[Con1996] E. Constant, H. Stapelfeldt, and P.B. Corkum, *Phys. Rev. Lett.* **76** 4140 (1996).

[Cor1993] P.B. Corkum, *Phys. Rev. Lett.* **71** 1994 (1993).

[Han1975] G.R. Hanson, *J. Chem. Phys.* **62** 1161 (1975).

[His1998] H. Hishikawa, A. Iwamae, K. Hoshina, M. Kono, and K. Yamanouchi, *Chem. Phys. Lett.* **282** 283 (1998).

[Iac1998] C. Iaconis and I.A. Walmsley, *Opt. Lett.* **23** 792 (1998).

[Ima1994] A. Imamoglu and Y. Yamamoto, *Phys. Rev. Lett.* **72** 210 (1994).

[Lég2003] F. Légaré, I.V. Litvinyuk, P.W. Dooley, F. Quéré, A.D. Bandrauk, D.M. Villeneuve, and P.B. Corkum, *Phys. Rev. Lett.* **91** 093002 (2003).

[Mor1964] Y. Morino, Y. Kikuchi, S. Saito, and E. Hirota, *J. Mol. Spectrosc.* **13** 95 (1964).

[Nii2002] H. Niikura, F. Légaré, R. Hasbani, A.D. Bandrauk, M.Yu. Ivanov, D.M. Villeneuve, and P.B. Corkum, *Nature* **417** 917 (2002).

[Nis1997] M. Nisoli, S. De Silvestri, and O. Svelto, *Opt. Lett.* **22** 522 (1997).

[San1999] J.H. Sanderson, A. El-Zein, W.A. Bryan, W.R. Newell, A.J. Langley, and P.F. Taday, *Phys. Rev. A* **59** R2567 (1999).

[Sch1994] M. Schmidt, D. Normand, and C. Cornaggia, *Phys. Rev. A* **50** 5037 (1994).

[Sei1995] T. Seideman, M. Yu. Ivanov, and P.B. Corkum, *Phys. Rev. Lett.* **75** 2819 (1995).

[Str1992] D.T. Strickland, Y. Beaudoin, P. Dietrich, and P.B. Corkum, *Phys. Rev. Lett.* **68** 2755 (1992).

[Vag1989] Z. Vager, R. Naaman, and E.P. Kanter, *Science* **244** 426 (1989).

[Vra1996] M.J.J. Vrakking, D.M. Villeneuve, and A. Stolow, *J. Chem. Phys.* **105** 5647 (1996).

[Zaj1994] D. Zajfman, *Comments At. Mol. Phys.* **29** 369 (1994).

[Zav1990] A. Zavriyev, P.H. Bucksbaum, H.G. Muller, and D.W. Schumacher, *Phys. Rev. A* **42** 5500 (1990).

[Zuo1995] T. Zuo and A.D. Bandrauk, *Phys. Rev. A* **52** R2511 (1995).

Chapter 6
Imaging of Rotational Wave-Packet Dynamics

The first dynamical imaging experiments performed using the PATRICK instrument are described in this chapter. Using a pump-probe technique, rotational wave packets were created and directly imaged via Coulomb explosion in both N_2 and O_2. A linearly polarized 45 fs laser pulse was used for wave-packet creation in conjunction with a circularly polarized imaging pulse. By measuring the three-dimensional velocities of specific Coulomb explosion fragments, a series of two-dimensional projections of the evolving wave packet's angular distribution were obtained. The wave packet's evolution is highlighted near the first, second, sixth, and tenth full revival times and also in the vicinity of the one-eighth, one-quarter, one-half, and three-quarter fractional revivals.

This chapter is structured as follows. The imaging technique's concept and experimental configuration are presented in §6.1 and §6.2, respectively. Experiments conducted to characterize the Coulomb explosion of N_2 and to select N^{3+} ions originating from the $N_2^{5+} \rightarrow N^{2+} + N^{3+}$ dissociation channel are described in §6.3. In §6.4, revival structures of N_2 rotational wave packets (derived from the measured N^{3+} angular distributions) are presented, modeled, and compared with O_2 revival structures. The effects of centrifugal deformation, nuclear spin, and aligning pulse intensity on the revival structures are discussed. In §6.5, measured angular distributions corresponding to full and fractional rotational revivals in N_2 and O_2 are presented. Of particular interest is the 1/8-revival in O_2 that occurs in a featureless region of the alignment

revival structure. The time-dependent angular distributions are depicted as polar representations, intensity maps, and projections onto basis states.

6.1 Wave-Packet Alignment and Imaging

The translational and rotational behaviour of gas phase molecules can be controlled using the large Stark shifts produced by intense laser pulses [Cor1999]. Such pulses have been used to trap [Tak1998], focus [Sta1997], and spin molecules [Kar1999, Spa2001a, Spa2001b, Vil2000]. The ability of intense laser pulses to produce rotational wave packets [Fri1995, Kim1996, Lar1999, Lar2000, Sak1999, Sei1995a] that exhibit transient molecular alignment is of particular interest. Aligned molecules are advantageous for applications such as surface scattering research [Fri1991], surface catalysis [Cho1991], and surface processing [Sei1997].

Strong field alignment requires an anisotropic polarizability leading to different Stark shifts along at least two molecular axes. If the laser field is applied adiabatically, the molecule aligns with its most polarizable axis along the laser polarization direction [Fri1995, Kim1996, Lar1999, Lar2000, Sak1999, Sei1995a]. If the pulse duration is short relative to the molecular rotational period, the molecule experiences an impulse toward alignment [Ort1999, Ros2001, Ros2002a, Ros2002b, Sei1999]. In that case, the resulting rotational wave packet exhibits transient alignment after the pulse is over. For linear molecules, the alignment is reproduced in a series of full revivals at intervals of one fundamental rotational period. Rotational wave packets can also be produced by rapidly truncating an adiabatic aligning pulse [Kal2002, Und2003, Vil2002].

Many applications benefit from molecular alignment [Cho1991, Fri1991, Lit2003, Nii2002, Sei1997] but the presence of a strong aligning laser field can interfere with subsequent measurements. Therefore, transient alignment has the advantage of producing field-free aligned molecules for short pulse experiments [Ort1999, Sei1999].

To extract quantitative information in the molecular frame from measurements made in the laboratory frame, the complete angular distribution function must be known. There are two approaches to obtaining the angular distribution function. (1) The amplitude and phase of all rotational states that are thermally or nonthermally populated must be measured. This could be achieved via Fourier transformation of a single time-dependent parameter characteristic of the wave packet's dynamics and comparison with a numerical simulation for similar aligning pulse parameters [Ros2001, Ros2002a, Ros2002b]. (2) The distribution function can be measured directly at a particular time. In this chapter, the latter approach is demonstrated, as is the equivalence of the two methods.

In these experiments, a 45 fs linearly polarized "aligning" pulse creates a wave packet that exhibits macroscopic field-free molecular alignment at well-defined time delays. The time evolution of the wave packet is observed using an intense, circularly polarized "exploding" pulse. At each time delay, molecules are multiply ionized by the exploding pulse and undergo rapid dissociation (Coulomb explosion). The resultant atomic ion fragments are analyzed to yield the three-dimensional velocity of each immediately following the Coulomb explosion. For a diatomic molecule, such initial velocities are parallel to the molecular axis if the dissociation is rapid. Hence, the distribution of molecular orientations for the rotational wave packet was directly measured at various instants during its time evolution.

Only angles within the polarization plane of the circularly polarized exploding pulse were considered. This is important because Coulomb explosion is most efficient for molecules oriented parallel to the laser polarization [Con1996, Fra1987, Sei1995b, Zuo1993]. With circular polarization, the ionization probability depends solely upon the out-of-plane angle [Ell1999]. Since the in-plane angle is unbiased, the measured angular distributions accurately reflect the actual molecular ensemble.

6.2 Experimental Configuration

The laser pulses used in the wave-packet imaging experiments were derived from the linearly polarized, 800 μJ, 800 nm wavelength, 500 Hz output of the Ti:sapphire regenerative amplifier. The pulse duration after the regenerative amplifier was measured to be 39 fs using SPIDER [Iac1998] and estimated to be 45 fs in the experimental chamber. A Mach-Zehnder interferometer was used to divide the laser output into aligning and exploding pulses, to introduce a relative time delay, and to recombine the two beams collinearly. A telescope was installed in the aligning pulse arm of the interferometer to decrease the beam diameter by a factor of two. This produced an aligning focus whose minimum cross sectional area and confocal parameter were each four times greater than those of the exploding pulse and ensured that only those molecules upon which the aligning pulse had acted most strongly were exploded. A quarter-wave plate was used to polarize the exploding pulse circularly. The interferometer's beam combiner was used at near-normal incidence to preserve the polarization states of the two pulses. The 10 μJ aligning and 200 μJ exploding pulses entered an ultrahigh-vacuum experimental chamber and were focused by an on-axis parabolic mirror (*f*/2, f = 50 mm) into a well-collimated beam of nitrogen molecules.

The operating pressures in the source, intermediate, and explosion subchambers of the PATRICK instrument were 7×10^{-5} mbar, 1×10^{-8} mbar, and 2×10^{-9} mbar, respectively. The molecular beam was produced by expanding 33 mbar of N_2 through the continuous gas reservoir's 100 μm diameter circular nozzle. Beyond the piezoelectric slit, the cross section of the molecular beam was rectangular (1.5 mm × 40 μm). The laser propagation direction was along the thin (40 μm) dimension of the molecular beam. Geometric constraints limited the

molecular beam's transverse translational temperature to less than 0.01 K. The measured longitudinal temperature was 90 K.

Since the molecular beam thickness was approximately equal to the aligning focus' confocal parameter, target molecules were confined to the high-intensity region of the aligning focal volume. The number density of the molecular beam was ~10^{10} molecules/cm^3 beyond the slit, corresponding to ~10 molecules within the overlap region of the aligning laser and molecular beams. While the interaction volumes of the two foci were approximately equal, the confocal parameter of the exploding focus was a factor of four smaller than that of the aligning focus. As a result, less than one molecule per laser pulse was present in the high-intensity region of the exploding focus, i.e., the region in which the most highly charged Coulomb explosion channels were active. The selection of a high-charge Coulomb explosion channel ensured that only those molecules located at the centre of the aligning focal volume were probed.

The strength of the ion acceleration field within the time-of-flight mass spectrometer was 100 V/cm. The helical delay line anode detector was used to determine the arrival time and two-dimensional impact position of each molecular fragment. The ion impact data were used to determine the initial, three-dimensional velocity for each Coulomb explosion fragment and hence the orientation of each exploded molecule.

6.3 Coulomb Explosion Diagnostic Experiments

To perform accurate imaging of rotational wave packets using this technique, an appropriate Coulomb explosion channel must be selected. Strong field ionization of N_2 using a 4 × 10^{15} W/cm^2 exploding pulse produced parent ions ranging from N_2^+ to N_2^{6+}. Dissociation of the parent ions produced fragments ranging from N^+ to N^{3+} (Fig. 6.1a). The six active fragmentation

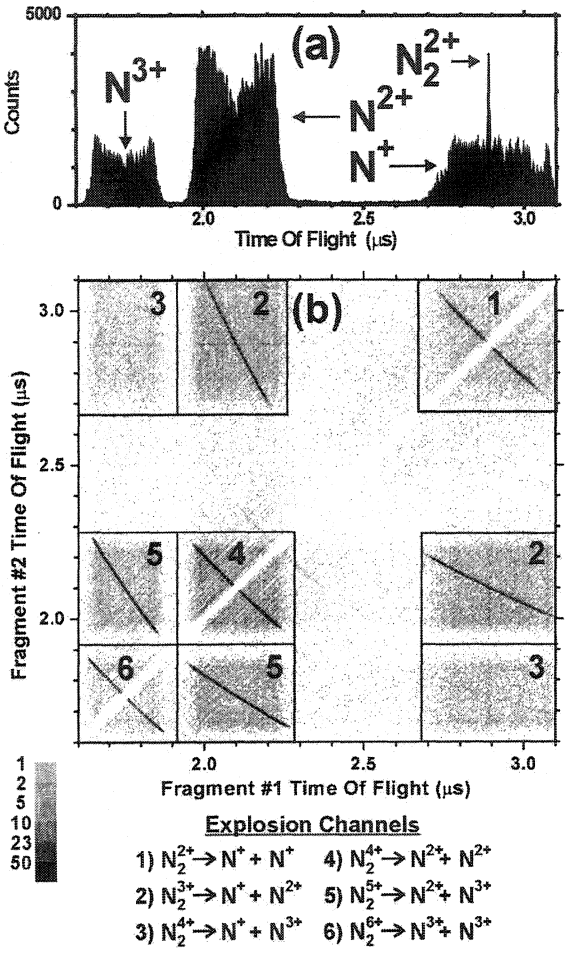

Fig. 6.1. ***(a)* Nitrogen fragment time-of-flight spectrum.** *Coulomb explosion of N_2 using the exploding pulse produces N^+, N^{2+}, and N^{3+} fragments via numerous dissociation channels. Some unexploded N_2^{2+} is also observed.* ***(b)* N_2 Coulomb explosion correlation map.** *For each exploding pulse, the individual detector impact times of all possible nitrogen fragment pairs are plotted against each other. Each numbered box contains fragment pair data for a specific dissociation channel (see legend). Within each box, the dark diagonal (top left to bottom right) streak results from correlated fragment pairs, i.e., fragments originating from the same N_2 molecule. The diffuse shading within each box stems from false coincidences. The narrow unshaded region (diagonal from bottom left to top right) arises from the 16 ns pulse pair resolution of the constant fraction discriminator used for fragment impact timing.*

channels can be identified from a correlation map analogous to that discussed by Frasinski *et al.* [Fra1989] (Fig. 6.1b). For accurate imaging, a high-charge dissociation channel must be selected to ensure that the molecule dissociates before molecular reorientation can occur. This criterion ensures that the momenta of fragment ions are parallel to the molecular axis. For the exploding pulse, the two most highly charged Coulomb explosion channels were $N_2^{5+} \rightarrow N^{2+} + N^{3+}$ and $N_2^{6+} \rightarrow N^{3+} + N^{3+}$ (Fig. 6.1b; boxes 5 and 6, respectively).

The limitations of the PATRICK instrument's detection electronics also influenced the choice of Coulomb explosion channel. The pulse pair resolution of each of its five constant-fraction discriminators is ~15 ns. As a result, certain molecular orientations are detected less efficiently for explosion channels that produce identical fragments (such as $N_2^{6+} \rightarrow N^{3+} + N^{3+}$). This inhomogeneous detection efficiency for symmetric dissociation channels gives rise to the

unshaded "dead zone" which runs diagonally through boxes 1, 4, and 6 in Fig. 6.1b. All molecular orientations are (in principle) equally detectable for asymmetric channels, however (as evidenced by the continuous dark streaks in boxes 2 and 5 in Fig. 6.1b). Therefore, wave-packet imaging was performed using only fragments originating from the asymmetric $N_2^{5+} \rightarrow N^{2+}+N^{3+}$ channel.

Conservation of momentum was used to select N^{2+} and N^{3+} fragments originating from the desired $N_2^{5+} \rightarrow N^{2+}+N^{3+}$ dissociation channel. The total N^{2+} and N^{3+} yields (Figs. 6.2a and 6.2b) are composed of overlapping contributions from various explosion channels. Since the vector sum of a N^{2+} fragment's momentum $\boldsymbol{p}_{2+}$ and a N^{3+} fragment's momentum $\boldsymbol{p}_{3+}$ is zero if they originate from the same N_2^{5+} parent ion, fragments produced via the desired channel could be identified. This constraint was imposed experimentally by summing the momenta of each

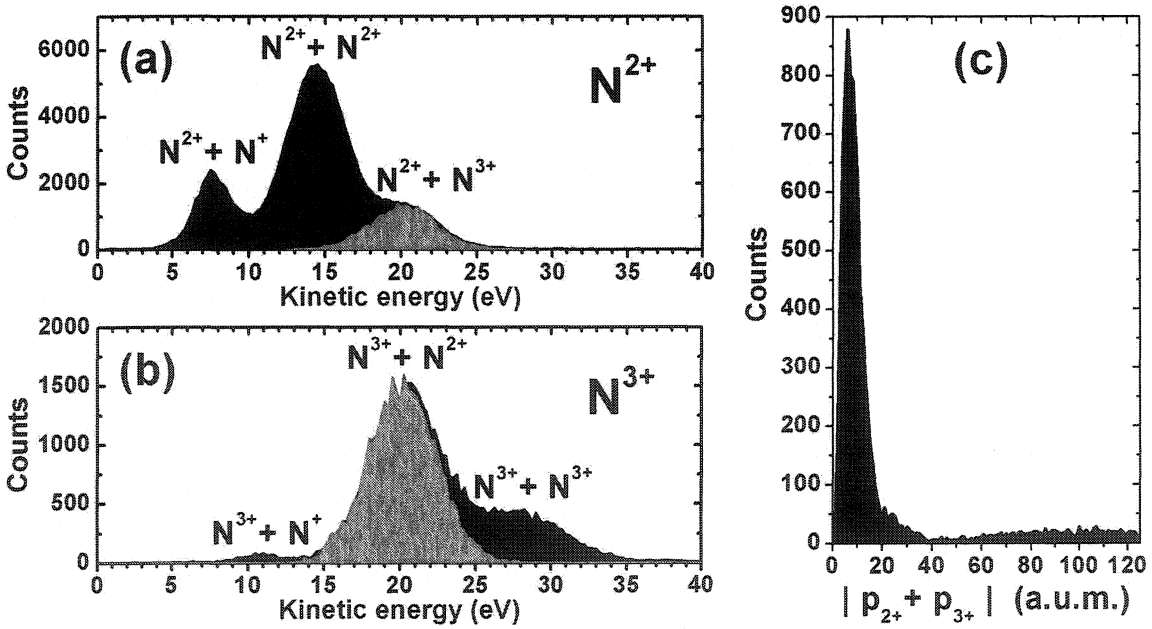

Fig. 6.2. Selection of $N_2^{5+} \rightarrow N^{2+} + N^{3+}$ explosion channel. *The kinetic energy spectra for N^{2+} and N^{3+} fragments consist of overlapping contributions from various Coulomb explosion channels (black regions in panels (a) and (b), respectively). Panel (c) is a histogram of the three-dimensional momentum sum for all N^{2+}-N^{3+} fragment pairs. The desired $N_2^{5+} \rightarrow N^{2+} + N^{3+}$ channel was selected by retaining only low (< 15 atomic units) total momentum pairs and exhibits a characteristic 15–25 eV fragment energy (grey regions in panels (a) and (b)).*

possible N^{2+}-N^{3+} pair recorded for each laser pulse (Fig. 6.2c). Only those fragment pairs that satisfied the condition $p_{2+} + p_{3+} < 15$ atomic units (i.e., the grey areas in Figs. 6.2a and 6.2b) were considered to have originated from the desired channel and retained. The imposition of this constraint clearly shows that the $N_2^{5+} \rightarrow N^{2+} + N^{3+}$ channel is characterized by fragment kinetic energies in the 15-25 eV range (Figs. 6.2a and 6.2b).

6.4 Wave-Packet Revival Structures

The time evolution of the wave packet produced by the aligning pulse can be written as a sum over the molecular rotational states:

$$\Psi(t) = \sum_J a_J e^{-i\frac{E_J}{\hbar}t} |J, M\rangle, \tag{6.1}$$

where E_J are the energy eigenvalues, $|J,M\rangle$ are spherical harmonics, and M is the projection of the total angular momentum vector onto the polarization axis of the aligning pulse. Note that the cylindrical symmetry of the optical potential prevents the coupling of different M-values. For convenience, the M-dependence of the kets is omitted in the following discussion. For the lowest vibrational state of the molecule (v = 0), the rotational energies are given by $E_J \approx hcB_0 J(J+1)$, where h is Planck's constant, c is the speed of light in vacuum, and B_0 is the ground state rotational constant. For wave packets containing high-$|J\rangle$ states, centrifugal distortion of the molecule must be taken into account. In such cases, the energy eigenvalues become

$$E_J = hc\left[B_0 J(J+1) - D_e J^2 (J+1)^2\right], \tag{6.2}$$

where D_e is the deformation constant for the nonvibrating molecule [Her1989]. For N_2, B_0 = 1.989581 cm^{-1} and $D_e = 5.76 \times 10^{-6}$ cm^{-1} [Hub2001].

Coulomb exploding N_2 at successive time delays (27 fs increments) allowed the field-free evolution of the rotational wave packet created by the aligning pulse to be observed. The peak

intensity of the aligning pulse (1.4×10^{14} W/cm^2) was chosen to achieve alignment without ionizing N_2. At each delay, 2000 N^{3+} fragments originating from the $N_2^{5+} \rightarrow N^{2+} + N^{3+}$ dissociation channel (i.e., those with kinetic energies in the 15-25 eV range) were collected. The three-dimensional initial velocity vector for each N^{3+} fragment (which was collinear with the pre-explosion orientation of the parent molecule) was then calculated.

The molecular alignment axis (i.e., the polarization axis of the linearly polarized aligning pulse) lay in the polarization plane of the circularly polarized exploding pulse (Fig. 6.3). The angle ϑ between the alignment axis and the projection of each three-dimensional fragment velocity onto the polarization plane was measured. Since the exploding pulse was circularly polarized, the Coulomb explosion probability was independent of the angle ϑ. Hence, experimental ϑ-distributions are unbiased and depend solely upon the actual ensemble of molecular orientations.

Raw ϑ-distributions were normalized using a "background" ϑ-distribution to ensure that a slightly elliptical ($\varepsilon = 0.97$) exploding pulse polarization did not bias the determination of molecular orientations. The background ϑ-distribution was obtained in a single pulse experiment by exploding an isotropic ensemble of molecules.

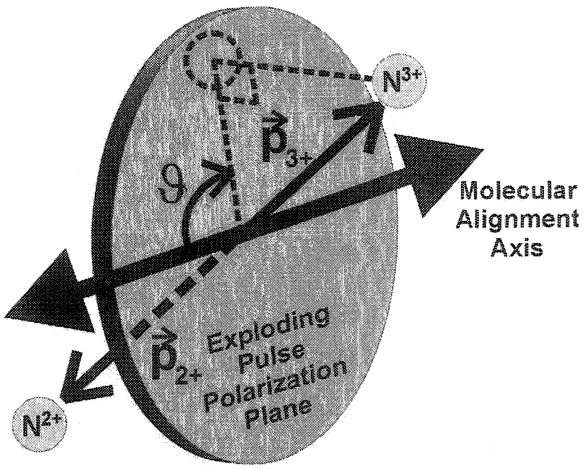

Fig. 6.3. Definition of observation angle ϑ. *Since $N_2^{5+} \rightarrow N^{2+} + N^{3+}$ is a prompt dissociation channel, the momentum of each fragment is parallel to the molecular axis. Thus, a single fragment momentum measurement is sufficient to determine a molecule's orientation. The three-dimensional momentum of each N^{3+} fragment was projected onto the polarization plane of the exploding pulse. The angle ϑ between the momentum projection and the molecular alignment (i.e., aligning pulse polarization) axis was then measured.*

While complete time-dependent ϑ-distributions were measured, it is typical (in the revival literature) to plot the first moment of such distributions ($\langle\cos^2\vartheta\rangle$ in this case) as a function of time. The measured ϑ-distributions are presented and discussed in the following section (§6.5). In keeping with convention, the degree of alignment at each aligning-exploding delay was characterized by calculating $\langle\cos^2\vartheta\rangle$ for each normalized ϑ-distribution. In this scheme, $\langle\cos^2\vartheta\rangle = 0.5$ reflects an isotropic distribution of molecular orientations while $\langle\cos^2\vartheta\rangle = 1$ indicates complete alignment. The limiting case in which all molecules are perpendicular to the alignment axis is denoted by $\langle\cos^2\vartheta\rangle = 0$. Note that the measured projection angle ϑ differs from the azimuthal angle of a spherical coordinate system θ (for which $\langle\cos^2\theta\rangle = 1/3$ reflects an isotropic distribution).

Measured $\langle\cos^2\vartheta\rangle$ Revival Structures

The time evolution of the N_2 alignment parameter $\langle\cos^2\vartheta\rangle$ is depicted in Fig. 6.4a. Prior to the arrival of the aligning pulse (i.e., $t < 0$), the molecular ensemble is isotropic (i.e., $\langle\cos^2\vartheta\rangle = 0.50$). The arrival of the aligning pulse is followed by a prompt net alignment ($t = T_0 = 0.067$ ps). Neglecting centrifugal distortion, each $|J\rangle$ state within the rotational wave packet accumulates phase with a different angular frequency given by

$$\omega_J = \tfrac{1}{2} J(J+1)\omega_1, \tag{6.3}$$

where $\omega_1 = 4\pi B_0 c$ is the fundamental phase frequency, i.e., that of $|1\rangle$. Thus, the constituent $|J\rangle$ states rapidly dephase with respect to each other and the initial net alignment quickly dissipates. The baseline for $t > 0$ is higher than the isotropic value $\langle\cos^2\vartheta\rangle = 0.5$, however. Known hereafter as "incoherent alignment", this baseline shift (which is due to the first term in Eq. A6 in [Doo2003]) can be understood as follows. Initially (i.e., $t < 0$), the relative $|J\rangle$ state populations

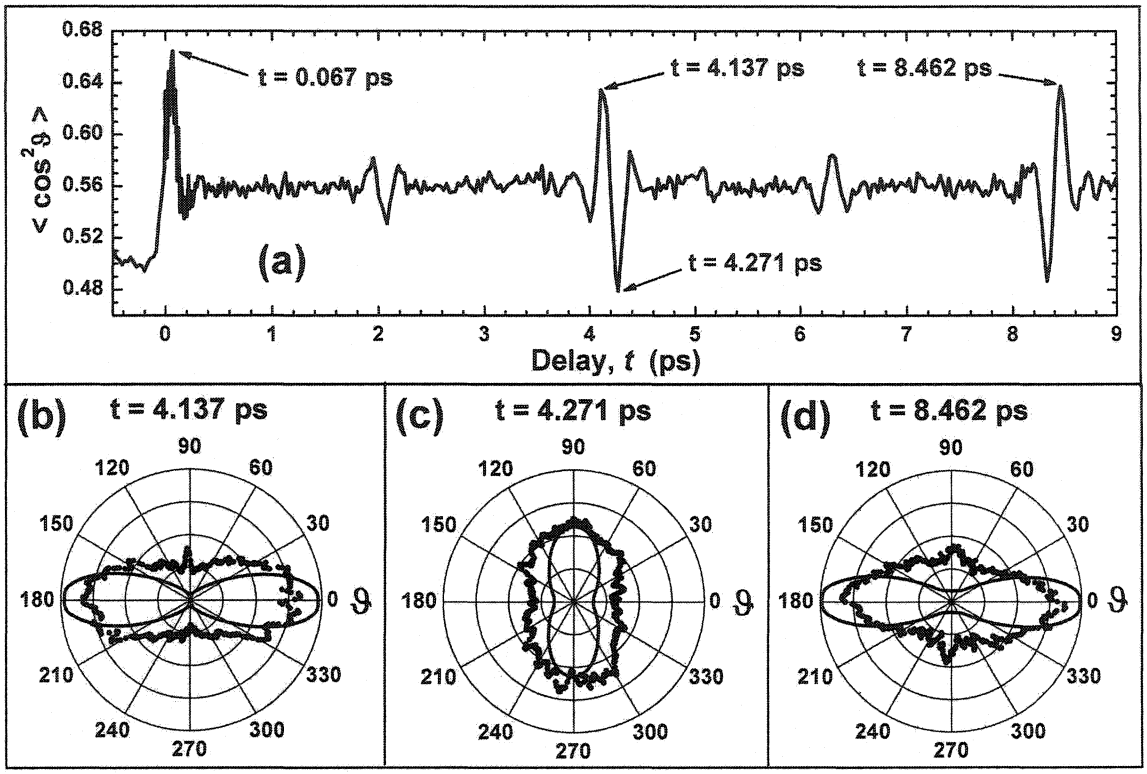

Fig. 6.4. ***(a) ⟨cos²ϑ⟩ revival structure for N_2.*** *The variation of ⟨cos²ϑ⟩ with aligning pulse-exploding pulse delay is depicted. Prior to wave-packet creation ($t < 0$), the molecular ensemble is isotropic and ⟨cos²ϑ⟩ = 0.50. The aligning pulse creates a rotational wave packet at $t = 0$ which exhibits maximum field-free alignment at $t = 0.067$ ps. Thereafter, an elevated baseline (⟨cos²ϑ⟩ ≈ 0.56) due to incoherent alignment was observed. Significant net alignment and antialignment is observed during the first revival ($t = 8.462$ ps) and half-revival ($t = 4.271$ ps) of the wave packet, respectively.* ***(b)-(d) Plots of measured (dots) and simulated (lines) N_2 ϑ-distributions.*** *The molecular alignment axis lies along $\vartheta = 0°$ and $\vartheta = 180°$ and is therefore horizontal in each figure. The rotational wave packet exhibits significant net alignment prior to the half-revival ($t = 4.137$ ps; panel (b)) and during the first revival (panel (d)). Net antialignment is observed during the half-revival (panel (c)). For clarity, the areas of the simulated plots are two-thirds those of the measured distributions.*

were given by a thermal Boltzmann distribution and M-values were uniformly populated for each $|J\rangle$ state. The aligning pulse modifies the $|J\rangle$ state distribution by inducing various rotational excitations and de-excitations via Raman transitions. Since there exists a lower bound for Raman de-excitation (i.e., $|0\rangle$) but no such limit for excitation, the resulting wave packet exhibits net rotational excitation, i.e., $\langle J \rangle_{packet} > \langle J \rangle_{thermal}$. The laser-molecule interaction does not alter the distribution of M-values, however. Thus, rather than being uniformly distributed, the angular

momentum vectors of each $|J\rangle$ state in the wave packet are preferentially oriented perpendicular to the aligning pulse polarization. In terms of molecular orientation, this corresponds to a small but persistent net alignment of the ensemble and an elevated experimental baseline (i.e., $\langle\cos^2\vartheta\rangle > 0.50$) for $t > 0$.

Since the wave packet evolves in a field-free environment, the $|J\rangle$ states eventually begin to rephase. When the accumulated phases of each $|J\rangle$ state are equal (to within multiples of 2π), the initial net alignment is reproduced in an event known as a full wave-packet revival. Since $J(J+1)$ is even for all J, all angular frequencies ω_J are integer multiples of the fundamental frequency ω_1 (Eq. 6.3). Therefore, the time of the first full revival, $t = T_0 + T_1$, is determined by ω_1 according to $T_1 = 2\pi/\omega_1 = (2B_0c)^{-1} = 8.383$ ps. The net alignment associated with the first full revival ($t = T_0 + T_1 = 8.462$ ps) maximizes 8.395 ps after the initial alignment at time T_0 (Fig. 6.4a). Since the time increment in the experiment was 27 fs, the result is in agreement with expectation.

Significant net alignment and "antialignment" also occur near fractional revival times $t = T_0 + T_\eta$, where $T_\eta = \eta T_1$ for $\eta = ¼, ½, ¾$. During the η-revival, the accumulated phases of states $|J\rangle$ and $|J+2\rangle$ differ by $2\pi\eta$ modulo 2π. For $\eta = ½$, the relative phases of all $|J\rangle$ states differ by integer multiples of π. At the half-revival, the sets of even $|J\rangle$ states corresponding to $J = 0,4,8,\ldots$ and odd $|J\rangle$ states given by $J = 3,7,11,\ldots$ are precisely in phase with each other. However, they are π out of phase with the set consisting of $J = 2,6,10,\ldots$ and $J = 1,5,9,\ldots$. The net result is destructive interference along the alignment axis and a localization of the wave packet in the plane perpendicular to it. Hence, significant net antialignment is expected at the first half-revival time $t = T_0 + ½T_1 = 4.259$ ps. In fact, the minimum value of $\langle\cos^2\vartheta\rangle$ occurred at $t = 4.271$ ps (Fig. 6.4a), in excellent agreement with the predicted half-revival time.

Full revivals of the wave packet occur at integer multiples of the first revival time, i.e., $t = T_0 + T_n$, where $T_n = nT_1$ for n = 1,2,3,.... The time evolution of the N_2 alignment parameter for the first, second, sixth, and tenth full wave-packet revivals (n = 1,2,6,10) is depicted in Figs. 6.5a to 6.5d, respectively. The measured (predicted) times of maximum net alignment for each revival were t = 8.462 ps (8.450 ps), 16.857 ps (16.832 ps), 50.476 ps (50.364 ps), and 83.990 ps (83.895 ps). Each full revival occurred slightly later than predicted. The time lag results from a perturbation of the angular frequencies ω_J due to centrifugal distortion that was neglected in Eq. 6.3. Note that the time evolution of the alignment parameter $\langle\cos^2\vartheta\rangle$ is not identically reproduced for each revival. While the n = 1 data (Fig. 6.5a) exhibit inversion symmetry about $t \sim 8.4$ ps, the modulation structure becomes increasingly asymmetric, i.e., "chirped", for each successive revival. The observed chirp is a further consequence of the additional nonlinearity introduced into the ω_J frequency spectrum by centrifugal distortion.

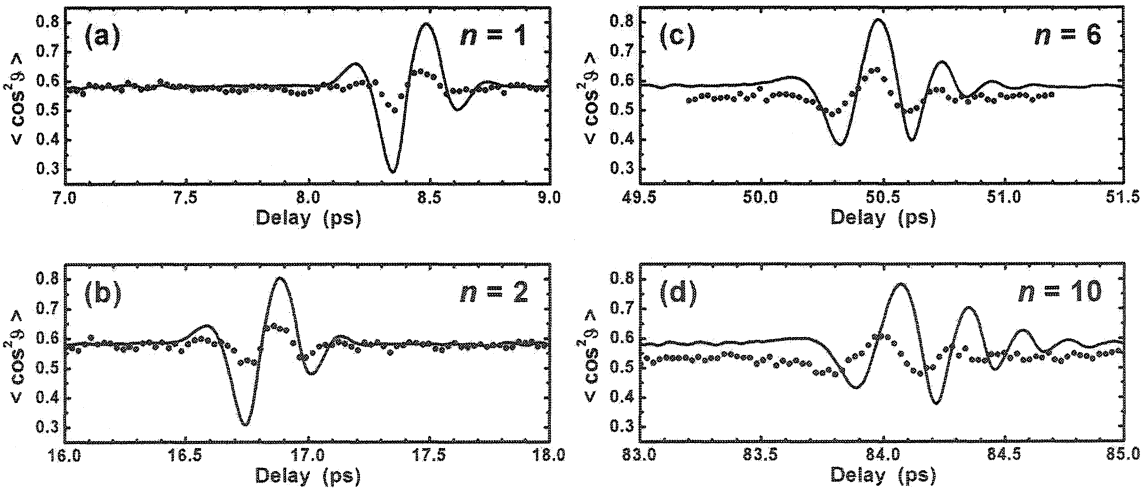

Fig. 6.5. Selected full revivals for N_2. *The measured time dependence of $\langle\cos^2\vartheta\rangle$ (dots) for the (a) first, (b) second, (c) sixth, and (d) tenth wave-packet revivals are depicted. Also shown are the results of the numerical model (line; see the appendix of [Doo2003]) that successfully predicts the times of maximum net alignment as well as the chirp that centrifugal distortion introduces into the revival structure.*

Modelling Wave-Packet Evolution

The rotational wave packet's creation by the aligning pulse and its subsequent time evolution were numerically simulated (see the appendix of [Doo2003] for details). Results for a 48.4 fs full width at half maximum $\sin^2$ pulse of peak intensity 1.7×10^{14} W/cm^2 are depicted in Fig. 6.5. An initial rotational temperature of 105 K was assumed. The model quite successfully predicts the times corresponding to maximum net alignment as well as the chirp of the revival structure. Unlike the model, the baseline of the experimental data decreases gradually toward an isotropic value of $\langle\cos^2\vartheta\rangle = 0.5$ with each successive revival. The decay is not due to molecular collisions since the mean collision time is ~ 0.1 s, nor is it a result of molecules entering or leaving the laser foci since molecules travel less than 0.1 μm during the measurement. The observed decay is most likely an artifact due to a slight relative shift of the exploding pulse focus with aligning-exploding delay. In such a case, the overlap between aligning and exploding foci would degrade with increasing delay and consequently the exploded molecules would exhibit decreasing incoherent alignment.

Wave-Packet Composition

The Fourier transform of the time-dependent alignment parameter $\langle\cos^2\vartheta\rangle$ yields information regarding the distribution of $|J\rangle$ states which comprise the rotational wave packet. The result is a spectrum of beat frequencies $\Delta\omega$ between states $|J\rangle$ and $|J+N\rangle$ whose magnitudes are proportional to the product of the quantum amplitudes $|a_J||a_{J+N}|$ (see the appendix of [Doo2003] for details). Neglecting centrifugal distortion, the beat frequencies $\Delta\omega_{J,J+N}$ are given by

$$\Delta\omega_{J,J+N} = \frac{E_{J+N}}{\hbar} - \frac{E_J}{\hbar} = \left[2NJ + N^2 + N\right]\frac{\omega_1}{2}. \qquad (6.4)$$

For a diatomic molecule, $\Delta J = 0,2$, and the dominant beat frequencies are

$$\Delta\omega_{J,J+2} = (4J+6)\frac{\omega_1}{2}. \tag{6.5}$$

The time dependence of $\langle\cos^2\vartheta\rangle$ stems directly from the Fourier sum of such frequency components. The Fourier transform of the time variation of $\langle\cos^2\vartheta\rangle$ spanning one full period of the N_2 revival structure (i.e., 0-9 ps, Fig. 6.4a) is depicted in Fig. 6.6a. The observed beat frequencies are in accord with the predictions of Eq. 6.5. The corresponding distribution of $|J\rangle$ states is approximately Gaussian, spans $J \sim 4$ to $J \sim 22$, and has a mean value of $J \sim 13$.

Nuclear Spin Statistics

The nuclear spin statistics of N_2 are evident in the Fourier transform of its revival structure. Since ^{14}N has nuclear spin $I = 1$, the molecule's total nuclear spin can take on the values $T = 0$, 1, or 2 and N_2 exists in ortho ($T = 0$, 2; J even) and para ($T = 1$; J odd) forms. Since a state with total nuclear spin T has degeneracy $2T+1$, the expected statistical weights of ortho-N_2 and para-N_2 are 6 (i.e., 1+5) and 3, respectively. Hence, the relative abundance of ortho-N_2 versus para-N_2 is 2:1. This is reflected in the ~2:1 intensity alternation between spectral lines corresponding to J even and J odd in the Fourier transform (Fig. 6.6a). Conversely, ^{16}O has

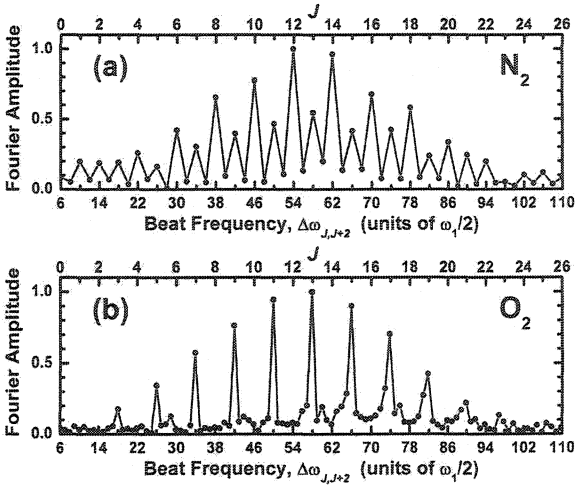

Fig. 6.6. Fourier transforms of *(a)* N_2 and *(b)* O_2 $\langle\cos^2\vartheta\rangle$ revival structures. *Each spectrum represents the decomposition of a molecular revival structure into beat frequencies between constituent $|J\rangle$ states. In both cases, the observed beat frequencies are in accord with the prediction $\Delta\omega_{J,J+2} = (4J+6)(\omega_1/2)$. For O_2, only odd $|J\rangle$ states are populated. N_2, however, exists in both ortho (J even) and para (J odd) forms. The ~2:1 intensity alternation in (a) arises from the 2:1 relative abundance of ortho-N_2 versus para-N_2.*

nuclear spin $I = 0$. Hence, O_2 exists in a single form for which only odd $|J\rangle$ states are populated. The Fourier transform of the alignment parameter $\langle\cos^2\vartheta\rangle$ for two full periods of the O_2 revival structure is depicted in Fig. 6.6b. As expected, only spectral lines corresponding to odd $|J\rangle$ states appear, whose positions are given by Eq. 6.5.

The different nuclear spin statistics of N_2 and O_2 are also evident in their revival structures. At the first quarter-revival (i.e., $t = T_0 + \frac{1}{4}T_1$), the phase difference (modulo 2π) between states $|J\rangle$ and $|J+2\rangle$ is $\pi/2$. Near the quarter-revival time, the even $|J\rangle$ states form a secondary wave packet while the odd $|J\rangle$ states form another. The two secondary wave packets are oppositely localized. That is, when one secondary packet is principally distributed along the alignment axis, the other is localized primarily in the perpendicular plane. For a wave packet in which even and odd $|J\rangle$ states are equally populated, the opposite localizations would cancel at the time of the quarter-revival and no net alignment (or antialignment) would be observed. In the case of N_2, both even and odd $|J\rangle$ states are populated but twice as much population exists in even states than in odd states. As a result, the temporary localization of the even secondary wave packet is only partially cancelled by its odd counterpart. Thus, some net N_2 alignment and antialignment is observed near $t = T_0 + \frac{1}{4}T_1 = 2.163$ ps (Fig. 6.4a). In the case of O_2, however, odd $|J\rangle$ states alone are populated. Since only a single localized wave packet exists at the time of a quarter-revival, strong net alignment and antialignment is observed in the vicinity of the 2.25 and 2.75 revivals ($t = 26.293$ ps and $t = 32.059$ ps, respectively) for O_2 (Fig. 6.7).

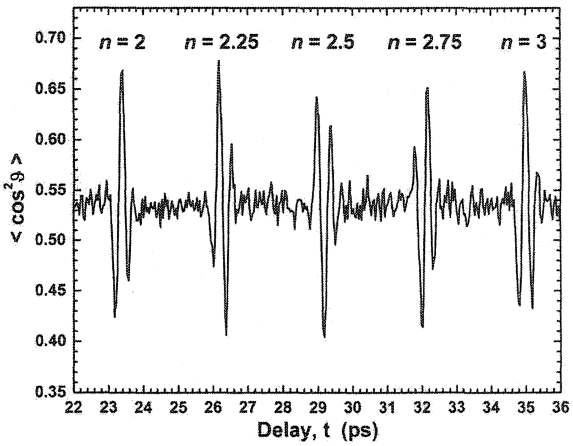

Fig. 6.7. $\langle\cos^2\vartheta\rangle$ revival structure of O_2. *The time variation of $\langle\cos^2\vartheta\rangle$ is depicted, spanning the second and third full revivals as well as the 2.25, 2.5, and 2.75 fractional revivals. Since only odd $|J\rangle$ states are populated in O_2, the 2.25 and 2.75 revivals are not suppressed (as is the case in N_2; Fig. 6.4).*

Intensity Dependence

The dependence of the N_2 $\langle\cos^2\vartheta\rangle$ revival structure on aligning pulse intensity was investigated in the vicinity of the first half-revival (Fig. 6.8). The baseline value of $\langle\cos^2\vartheta\rangle$ increases monotonically as the aligning pulse intensity is increased from 0.4×10^{14} W/cm^2 to 3.4×10^{14} W/cm^2, reflecting an increased degree of incoherent alignment. The revival structure amplitude increases up to an intensity of 2.0×10^{14} W/cm^2. This behaviour is as expected since the aligning pulse intensity reflects the depth of the associated optical potential well. The higher the aligning intensity, the deeper the potential well, and the larger the range of trapped $|J\rangle$ states. As observed, the maximum degree of alignment increases with the number of rotational states present in the superposition. At aligning intensities greater than 2.0×10^{14} W/cm^2, significant

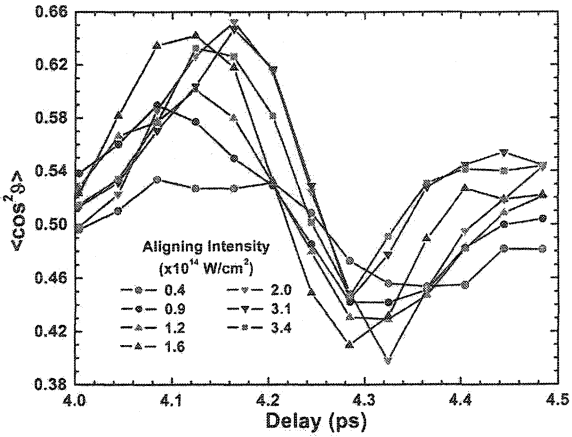

Fig. 6.8. Intensity variation of half-revival for N_2. *The time variation of $\langle\cos^2\vartheta\rangle$ in the vicinity of the first half-revival is depicted for several aligning pulse intensities. The baseline increases with aligning intensity. The amplitude of the revival structure increases for intensities up to 2.0×10^{14} W/cm^2. The transition from peak net alignment to maximum net antialignment becomes more rapid as the aligning intensity is increased.*

ionization of the N_2 molecules occurs and consequently the revival structure amplitude decreases.

As the aligning pulse intensity is increased, the alignment parameter $\langle\cos^2\vartheta\rangle$ also varies more rapidly with time (Fig. 6.8). To illustrate this effect better, a single-cycle sinusoid was fitted to each revival structure shown in Fig. 6.8. The oscillation frequency ω_{osc} corresponding to each sinusoid increases monotonically over the intensity range for which little N_2 ionization occurs, i.e., 0.4×10^{14} W/cm^2 to 2.0×10^{14} W/cm^2 (Fig. 6.9). This trend can be understood in terms of the central $|J\rangle$ state of the rotational wave packet. The revival structure's dominant oscillation frequency ω_{osc} corresponds (according to Eq. A6 of [Doo2003]) to the beat frequency $\Delta\omega_{J',J'+2}$ between the wave packet's two most highly populated $|J\rangle$ states J' and $J'+2$. Hence, the central rotational state of the wave packet (i.e., $J'+1$) can be determined from the measured value of ω_{osc} using Eq. 6.5. As shown in Fig. 6.9, the central rotational state is also observed to increase with aligning intensity. This is as expected since increasing the aligning intensity produces a deeper optical potential well and an increased value of $J'+1$.

6.5 Time-Dependent Angular Distributions

The rotational dynamics of molecules were observed by directly imaging molecular ϑ-distributions at various moments during the time evolution of its rotational wave packet. While

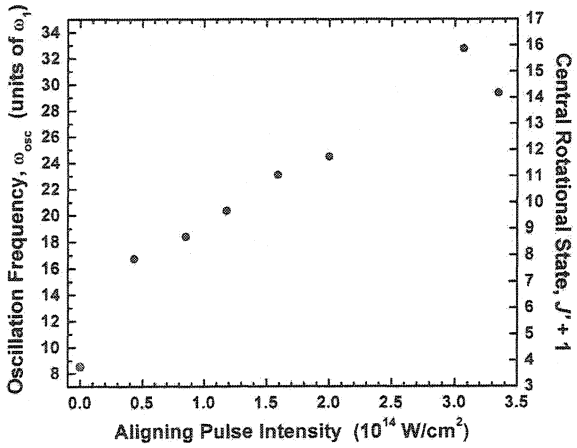

Fig. 6.9. Intensity variation of instantaneous frequency for N_2. *The dominant oscillation frequencies, ω_{osc}, of the measured N_2 revival structures (Fig. 6.8) as a function of aligning pulse intensity are shown (black circles). The central rotational states $|J+1\rangle$ of the corresponding wave packets are shown on the right axis. The increase in central rotational state corresponds to a deepening of the optical potential well with aligning intensity. For comparison, the most populated rotational state of the 105 K molecular beam is plotted at zero intensity (grey circle).*

conventional revival structures (i.e., plots of $\langle\cos^2\vartheta\rangle$ vs. time) such as Fig. 6.4a reflect net wave-packet behaviour, the time-dependent ϑ-distributions yield considerably more insight regarding the actual distributions of molecular orientations.

Measured Angular Distributions: Polar Representations

To illustrate the utility of the imaging technique, measured ϑ-distributions corresponding to significant points in the revival structure of N_2 (Fig. 6.4a) are presented. The molecular alignment axis lies along $\vartheta = 0°$ and $\vartheta = 180°$ and is therefore horizontal in the ϑ-distribution plots (Figs. 6.4b to 6.4d). During the first full wave-packet revival (t = 8.462 ps), the wave packet exhibits significant net alignment. This is reflected by measured (dots) and simulated (line) angular distributions (Fig. 6.4d) that are strongly peaked about the alignment axis and a corresponding peak value of $\langle\cos^2\vartheta\rangle$ in the revival structure (Fig. 6.4a). The simulated angular distribution was obtained using the approach described in the appendix of [Doo2003] followed by a projection of the entire wave packet onto the plane of polarization of the exploding pulse. At the half-revival time (t = 4.271 ps), molecules lie predominantly in the plane perpendicular to the alignment axis. As a result, the corresponding ϑ-distributions (Fig. 6.4c) are concentrated primarily along $\vartheta = 90°$ and $\vartheta = 270°$ and $\langle\cos^2\vartheta\rangle$ attains its minimum value. At t = 4.137 ps, the wave packet exhibits significant net alignment (Fig. 6.4b) just prior to the first half-revival which gives rise to a peak value of $\langle\cos^2\vartheta\rangle$.

Since they reflect net wave-packet behaviour, $\langle\cos^2\vartheta\rangle$ revival structures (such as Figs. 6.4a, 6.5, and 6.7) are useful for identifying times that correspond to significant net alignment or antialignment. Instances of net behaviour are rare during the evolution of a rotational wave packet, however. Hence, $\langle\cos^2\vartheta\rangle$ revival structures consist of a relatively flat baseline punctuated by regions of peaks and troughs. While such baselines indicate a wave packet's

degree of time-independent incoherent alignment, they provide no insight regarding molecular angular distributions at such times. Although minimal net alignment is observed in such baseline regions, the corresponding angular distributions can differ considerably. For instance, ϑ-distributions for the isotropic case (analogous to a circle (○) in Figs. 6.4b to 6.4d), a plus (+), a cross (×), and an asterisk (*) would each yield a net alignment parameter of $\langle\cos^2\vartheta\rangle = 0.5$. To distinguish such qualitatively different distributions, an angle-resolved imaging technique is required.

Since the molecular angular distribution at each time delay is measured, the wave packet's evolution can be followed even during periods of minimal net alignment. As an illustration, the results of imaging performed in the vicinity of the 1/8-revival in O_2 ($t \sim 1.4$ ps) are presented. The 1/8-revival occurs in the baseline region of the $\langle\cos^2\vartheta\rangle$ revival structure of O_2 (Fig. 6.10a). Figs. 6.10b to 6.10j depict both measured (dots) and simulated (lines) ϑ-distributions in the vicinity of the 1/8-revival. The value of $\langle\cos^2\vartheta\rangle$ is approximately equal for each distribution and the time increment for most of those shown is just 27 fs. Nevertheless, structures such as a bowtie (Fig. 6.10c), a plus (Fig. 6.10f), and a butterfly (Fig. 6.10h) can be qualitatively resolved.

Measured Angular Distributions: Intensity Maps

The time-dependent angular distributions can be compactly represented using the scheme of Fig. 6.11. Intensity maps for the measured (Fig. 6.11a) and simulated (Fig. 6.11b) angular distributions in the vicinity of the 1/8-revival of O_2 are depicted. White, grey, and black represent regions of high, intermediate, and low probability density, respectively. Although the 27 fs temporal resolution introduces a noticeable graininess, the measured intensity map captures the essential features of the molecular dynamics. Incoherent alignment is manifested by light streaks

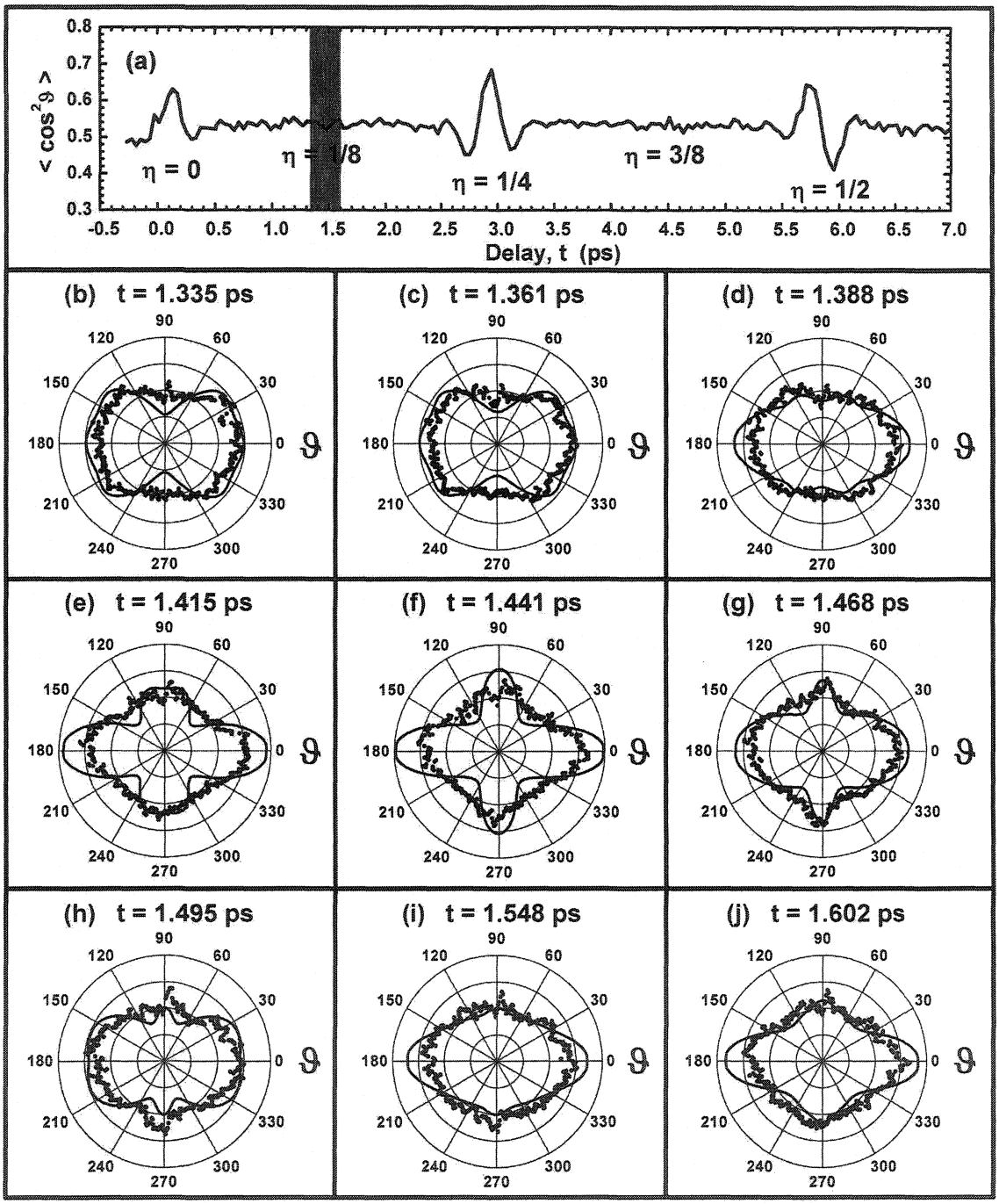

Fig. 6.10. Measured angular distributions near 1/8-revival of O_2. *(a)* $\langle\cos^2\vartheta\rangle$ revival structure of O_2. *Locations of the η-revivals are shown. The 1/8-revival occurs in the shaded region. (b)-(j)* Plots of O_2 ϑ-distributions near 1/8-revival. *The measured distributions (dots) follow the evolution of the model results (lines). Each measured distribution contains the results of 25,000 determinations of molecular orientation.*

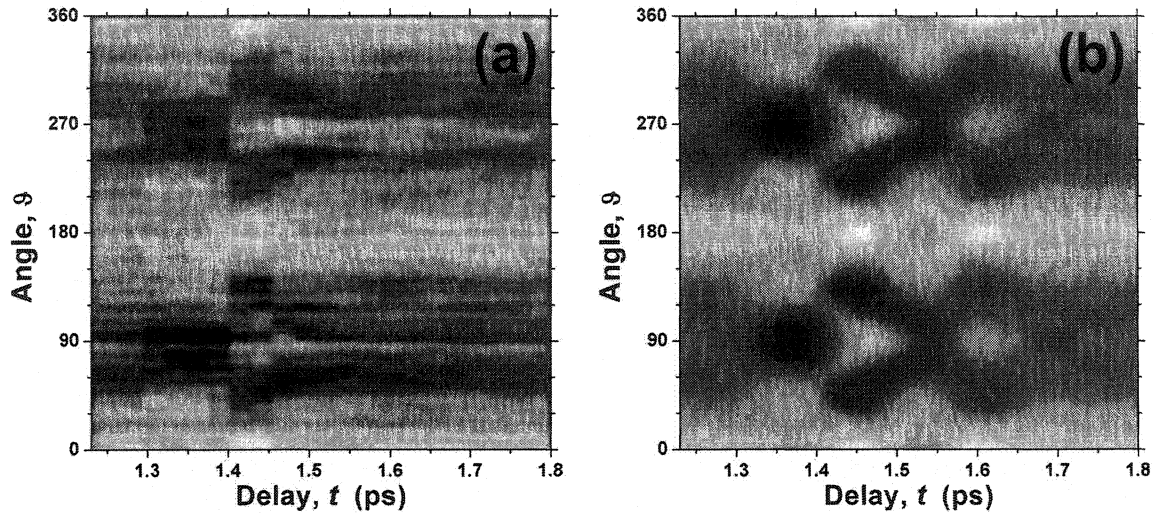

Fig. 6.11. Intensity maps of *(a)* measured and *(b)* simulated O_2 ϑ-distributions near 1/8-revival. *The ϑ-distribution (in degrees) at each time delay is plotted and labelled by shades of grey. Low probability density is represented by black, high density by white. Although grainy (due to the 27 fs experimental time increment), the measured intensity map captures the essence of the molecular dynamics.*

along the alignment axis (i.e., ϑ = 0°, 180°, and 360°). Dark regions centred at ϑ = 90° and ϑ = 270° reflect the appearance of the bowtie distribution (Fig. 6.10c) at t = 1.361 ps. The plus distribution (Fig. 6.10f) appears at t = 1.441 ps as four bright centres (at ϑ = 0°, 90°, 180°, 270°, and 360°) with two intervening diamond-shaped dark regions. A lower contrast replica of the plus distribution occurs at t = 1.602 ps (Fig. 6.10j). As a result, the corresponding centres and diamonds are less distinct in the intensity maps.

Measured Angular Distributions: Projections onto Basis States

The measured ϑ-distributions $S(\vartheta,t)$ can also be represented as projections onto an arbitrary angular basis set. For example, the angular data can be expanded in terms of squared cosines i.e., $S(\vartheta,t) = \sum_{n=0}^{\infty} c_n(t)\cos^2(n\vartheta)$. Note that the n = 1 term of this expansion corresponds to the $\langle\cos^2\vartheta\rangle$ revival structure used throughout this chapter to characterize the degree of wave-packet alignment along the aligning pulse polarization (e.g. Fig. 6.10a). Since $S(\vartheta,t)$ is measured,

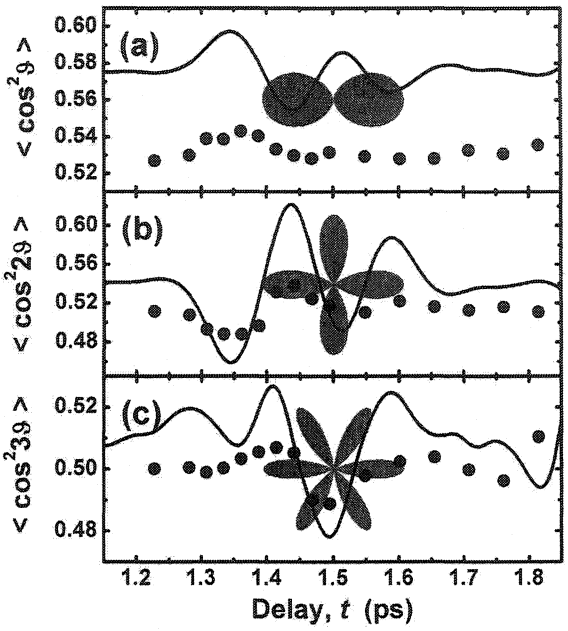

Fig. 6.12. Projections of O_2 ϑ-distributions onto angular basis states. *Time-dependent projections of the measured (dots) and simulated (line) ϑ-distributions onto the (a) $\cos^2\vartheta$, (b) $\cos^2 2\vartheta$, and (c) $\cos^2 3\vartheta$ basis states are depicted in the vicinity of the 1/8-revival of O_2. Polar representations of the basis states are superimposed in grey.*

however, higher order $\langle\cos^2(n\vartheta)\rangle$ revival structures corresponding to other terms of the expansion can also be computed. To illustrate this, projections of the measured (dots) and simulated (lines) O_2 angular distributions in the vicinity of the 1/8-revival onto the n = 1,2,3 states of the $\cos^2(n\vartheta)$ basis are shown in Fig. 6.12.

Of practical interest is the ability to search efficiently for an arbitrary target angular distribution $F(\vartheta)$ using this technique, even during data acquisition. This can be achieved in the laboratory by monitoring the generalized revival structure

$$G(t) = \frac{\int S(\vartheta,t)F(\vartheta)d\vartheta}{\int S(\vartheta,t)d\vartheta \int F(\vartheta)d\vartheta}. \tag{6.6}$$

Peaks in $G(t)$ denote times at which the measured angular distribution best corresponds to the target distribution, just as peaks in a $\langle\cos^2\vartheta\rangle$ revival structure indicate times of maximum net molecular alignment.

6.6 Conclusions

By conducting pump-probe experiments within the PATRICK instrument, the rotational dynamics of two diatomic molecules have been observed. Using molecular Coulomb explosion as a probe, direct imaging of rotational wave packets was performed and $\langle\cos^2\vartheta\rangle$ revival structures for N_2 and O_2 were obtained with up to 27 fs time resolution. Angular distributions corresponding to net field-free molecular alignment of N_2 during a full rotational wave-packet revival as well as net antialignment during a half-revival have been presented. Further, a series of angular distributions are shown that reflect the rich dynamical behaviour near the eighth-revival in O_2 for which no significant alignment occurs.

The ability to produce field-free ensembles of aligned molecules has enabled both our measurement of the directional dependence of the multiphoton ionization rate of N_2 [Lit2003] and our unambiguous demonstration of electron self-diffraction imaging. In the future, the ability to minimize orientational averaging should simplify experiments involving ultrafast electron diffraction [Wil1997], electron self-diffraction [Nii2002], and photoelectron angular distributions [Geβ2002].

To perform rotational imaging, the three-dimensional velocity vector was measured for a single ion fragment per molecule. Since the PATRICK instrument is capable of measuring and correlating the three-dimensional momenta of multiple ion fragments. This capability should permit time-resolved Coulomb explosion imaging [Doo2000, Vag1989] of the internal dynamics of small and intermediate polyatomic molecules.

6.6 Acknowledgements

Post-doctoral fellow Igor Litvinyuk, doctoral candidate Kevin Lee, and the author collaborated to collect the data presented in this chapter. The author performed the analysis of all

data presented in this chapter except the Fourier transformations of Fig. 6.6 (which were calculated by Mr. Lee).

6.7 References

[Cho1991] V.A. Cho and R.B. Berstein, *J. Phys. Chem.* **95** 8129 (1991).

[Con1996] E. Constant, H. Stapelfeldt, and P.B. Corkum, *Phys. Rev. Lett.* **76** 4140 (1996).

[Cor1999] P.B. Corkum, Ch. Ellert, M. Mehendale, P. Dietrich, S. Hankin, S. Aseyev, D. Rayner, and D. Villeneuve, Faraday Discuss. **113** 47 (1999).

[Doo2000] P.W. Dooley, V.R. Bhardwaj, and P.B. Corkum in *Proceedings of the International Conference on Lasers '99* (STS Press, McLean, VA, 2000), p. 8.

[Doo2003] P.W. Dooley, I.V. Litvinyuk, K.F. Lee, D.M. Rayner, M. Spanner, D.M. Villeneuve, and P.B. Corkum, *Phys. Rev. A* **68** 023406 (2003).

[Ell1999] Ch. Ellert and P.B. Corkum, *Phys. Rev. A* **59** R3170 (1999).

[Fra1987] L.J. Frasinski, K. Codling, P. Hatherly, J. Barr, I.N. Ross, and W.T. Toner, *Phys. Rev. Lett.* **58** 2424 (1987).

[Fra1989] L.J. Frasinski, K. Codling, and P.A. Hatherly, *Science* **246** 1029 (1989).

[Fri1991] B. Friedrich, D.P. Pullman, and D.R. Herschbach, *J. Phys. Chem.* **95** 8118 (1991).

[Fri1995] B. Friedrich and D. Herschbach, *Phys. Rev. Lett.* **74** 4623 (1995).

[Geβ2002] O. Geβner, Y. Hikosaka, B. Zimmerman, A. Hempelmann, R.R. Lucchese, J.H.D. Eland, P.-M. Guyon, and U. Becker, *Phys. Rev. Lett.* **88** 193002 (2002).

[Her1989] G. Herzberg, *Molecular Spectra and Molecular Structure: Volume I – Spectra Of Diatomic Molecules*, 2nd ed. (Krieger, Malabar, FL, 1989).

[Hub2001] K.P. Huber and G. Herzberg (data prepared by J.W. Gallagher and R.D. Johnson III) in *NIST Chemistry WebBook, NIST Standard Reference Database Number 69*, edited by P.J. Linstrom and W.G. Mallard, National Institute of Standards and Technology, Gaithersburg, MD, 2001, (http://webbook.nist.gov).

[Iac1998] C. Iaconis and I.A. Walmsley, *Opt. Lett.* **23** 792 (1998).

[Jag1998] O. Jagutzki, V. Mergel, K. Ullmann-Pfleger, L. Spielberger, U. Meyer, R. Dörner, and H. Schmidt-Böcking, *Proc. SPIE* **3438** 322 (1998).

[Kal2002] V. Kalosha, M. Spanner, J. Herrmann, and M.Yu. Ivanov, *Phys. Rev. Lett.* **88** 103901 (2002).

[Kar1999] J. Karczmarek, J. Wright, P. Corkum, and M. Ivanov, *Phys. Rev. Lett.* **82** 3420 (1999).

[Kim1996] W. Kim and P.M. Felker, *J. Chem. Phys.* **104**, 1147 (1996).

[Lar1999] J.J. Larsen, H. Sakai, C.P. Safvan, I. Wendt-Larsen, and H. Stapelfeldt, *J. Chem. Phys.* **111** 7774 (1999).

[Lar2000] J.J. Larsen, K. Hald, N. Bjerre, H. Stapelfeldt, and T. Seideman, *Phys. Rev. Lett.* **85** 2470 (2000).

[Lit2003] I.V. Litvinyuk, K.F. Lee, P.W. Dooley, D.M. Rayner, D.M. Villeneuve, and P.B. Corkum, *Phys. Rev. Lett.* **90** 233003 (2003).

[Nii2002] H. Niikura, F. Légaré, R. Hasbani, A.D. Bandrauk, M.Yu. Ivanov, D.M. Villeneuve, and P.B. Corkum, *Nature* **417** 917 (2002).

[Ort1999] J. Ortigoso, M. Rodríguez, M.Gupta, and B. Friedrich, *J. Chem. Phys.* **110** 3870 (1999).

[Pre1992] W.H. Press et al., *Numerical Recipes*, 2nd ed., (Cambridge University Press, Cambridge, England, 1992).

[Ros2001] F. Rosca-Pruna and M.J.J. Vrakking, *Phys. Rev. Lett.* **87** 153902 (2001).

[Ros2002a] F. Rosca-Pruna and M.J.J. Vrakking, *J. Chem. Phys.* **116** 6567 (2002).

[Ros2002b] F. Rosca-Pruna and M.J.J. Vrakking, *J. Chem. Phys.* **116** 6579 (2002).

[Sak1999] H. Sakai, C.P. Safvan, J.J. Larsen, K.M. Hilligsøe, K. Hald, and H. Stapelfeldt, *J. Chem. Phys.* **110** 10235 (1999).

[Sei1995a] T. Seideman, *J. Chem. Phys.* **103** 7887 (1995).

[Sei1995b] T. Seideman, M.Yu. Ivanov, and P.B. Corkum, *Phys. Rev. Lett.* **75** 2819 (1995).

[Sei1997] T. Seideman, *Phys. Rev. A* **56** R17 (1997).

[Sei1999] T. Seideman, *Phys. Rev. Lett.* **83** 4971 (1999).

[Sob1988] S.E. Sobottka and M.B. Williams, *IEEE Trans. Nucl. Sci.* **35** 348 (1988).

[Spa2001] M.Spanner and M.Yu. Ivanov, *J. Chem. Phys.* **114** 3456 (2001); M. Spanner, K.M. Davitt, and M.Yu. Ivanov, *J. Chem. Phys.* **115** 8403 (2001).

[Sta1997] H. Stapelfeldt, Hirofumi Sakai, E. Constant, and P.B. Corkum, *Phys. Rev. Lett.* **79** 2787 (1997).

[Tak1998] T. Takekoshi, B.M. Patterson, and R.J. Knize, *Phys. Rev. Lett.* **81** 5105 (1998).

[Und2003] J. Underwood, M. Spanner, M.Yu. Ivanov, J. Mottershead, B.J. Sussman, and A. Stolow, *Phys. Rev. Lett.* **90** 223001 (2003).

[Vag1989] Z. Vager, R. Naaman, and E.P. Kanter, *Science* **244** 426 (1989).

[Vil2000] D.M. Villeneuve, S.A. Aseyev, P. Dietrich, M. Spanner, M. Yu. Ivanov, and P.B. Corkum, *Phys. Rev. Lett.* **85** 542 (2000).

[Vil2002] D.M. Villeneuve, S.A. Aseyev, A. Avery, and P.B. Corkum, *Appl. Phys. B: Lasers Opt.* **74** S157 (2002).

[Wil1997] J.C. Williamson, J. Cao, H. Ihee, H. Frey, A.H. Zewail, *Nature* **386** 159 (1997).

[Zuo1993] T. Zuo, S. Chelkowski, and A.D. Bandrauk, *Phys. Rev. A* **48** 3837 (1993).

Chapter 7
Conclusions and Perspectives

The desire to behold the unseen motivates many fields of human endeavour. In science, knowledge of fundamental natural processes is the most prized. However, such processes occur on time and length scales that differ greatly from those of our common experience. Consequently, scientific advancement is heavily dependent upon technological innovation.

As the participants in chemical reactions, atoms and molecules are both fundamental and pervasive. The equilibrium structures of countless molecules have been elucidated using conventional spectroscopic and diffraction techniques. Although internal motion is as intrinsic to a molecule as its equilibrium structure, our capacity to observe molecular dynamics has been limited. However, recent advances in ultrafast lasers, multidimensional particle detectors, and computer technology have put dynamical imaging within reach. As a result, several complementary imaging approaches are under development in laboratories worldwide. Dynamical imaging has been a key objective of the National Research Council's Femtosecond Science program for nearly a decade. Having joined the group early in its effort, I have been fortunate to partake in the dream of time-resolved Coulomb explosion imaging and to contribute to its realization.

The PATRICK instrument was initially developed to perform time-resolved Coulomb explosion imaging and has proved equal to the task. Thus far, we have imaged the structures of D_2, D_2O, and SO_2 and observed vibrational wave-packet dynamics in D_2^+. Dynamical imaging of SO_2^+ and NH_3^+ vibrational wave packets shall soon be performed. Our results confirm that two of the criteria for accurate optically driven Coulomb explosion imaging can be met. First, existing

laser technology is sufficient to confine virtually any molecule inertially during its multiple ionization. Second, although we cannot remove every electron from most molecules, the potential surfaces of highly charged molecular ions are sufficiently Coulombic.

Accurate time-resolved Coulomb explosion imaging of most small polyatomic molecules should be possible. The extent to which the technique is applicable to large molecules is limited by both physical and practical considerations. Beyond a certain molecular size, plasma effects will become important and the gas of liberated electrons will partially shield the explosion. Furthermore, the multiple fragment correlation rate decreases exponentially with the number of atoms present in a molecule. Finally, the molecular structure retrieval algorithms used to invert the fragmentation data are bound to fail when the number of fragments becomes large. Despite the molecular size limitation, however, the wealth of insight into the wave-packet dynamics of small molecules (and their ions) that the technique could yield is unprecedented.

Our successful demonstration of laser-initiated Coulomb explosion imaging is a testament to the PATRICK instrument's high degree of sophistication. Several years were required to develop the unique apparatus that marries various state-of-the-art technologies. In the two years following its completion, however, the versatile machine has rapidly produced a series of diverse experimental results. In addition to laser-initiated Coulomb explosion imaging (Chapter 5), we have demonstrated how femtosecond pulses and Coulomb explosion can be applied to yield the world's smallest mass spectrometer (Chapter 3). The industrial potential of such devices will be enhanced as fibre lasers (for compact, energetic femtosecond pulse generation) and photonic band gap fibre technology (for high-power pulse delivery) continue to improve. In other experiments, we used Coulomb explosion to search for shake-off double ionization in D_2 (Chapter 4) and to measure the elapsed time between sequential electron removals (Chapter 5). Molecular Coulomb explosion also enabled our novel rotational wave-

packet imaging technique (Chapter 6). The first demonstration of electron self-diffraction imaging was also performed using the PATRICK instrument.

Our demonstration of electron self-diffraction imaging is an example of the fruitful interplay between science and technology. The PATRICK instrument was designed to measure the three-dimensional velocities of the ~10 eV fragment ions produced in time-resolved Coulomb explosion imaging experiments. While characterizing the completed apparatus, however, we found that even sub-millielectron-volt molecular ion recoil velocities could be measured. This unforeseen technical capability soon led us to conceive (and ultimately demonstrate) the electron self-diffraction imaging concept.

Significant efforts were made to demonstrate electron self-diffraction imaging during the doctoral research described here. However, a detailed account has been omitted since unambiguous results have only recently been obtained. Post-doctoral fellow Igor Litvinyuk and the author conducted the original experiments that involved argon and an isotropic ensemble of molecular nitrogen. A comparison of the Ar^+ and N_2^+ recoil momenta yielded results analogous to those of a powder diffraction experiment for the molecular case. Although highly suggestive, the finding was not conclusive, given the different scattering properties of argon and atomic nitrogen. The definitive experiment (conducted by Dr. Litvinyuk, doctoral candidate Kevin Lee, and post-doctoral fellow Daniel Comtois) involved an aligned ensemble of molecular nitrogen and was therefore analogous to a crystal diffraction measurement. By comparing two components of the N_2^+ recoil momentum, an unambiguous diffraction signature was observed that confirmed our original finding.

Time-resolved Coulomb explosion and electron self-diffraction imaging are complementary and represent the first half-scattering molecular imaging techniques yet developed. However, the latter method is likely to have the greater impact, since it could be

generalized to image relatively large molecules. By analyzing diffracted electrons (rather than ions), imaging of biomolecules might be possible. The electron self-diffraction concept is partially responsible for the funding of Montreal's forthcoming Advanced Laser Light Source.

The dynamic nature of a molecule ensures that its totality cannot be represented in a single structural image. That recognition motivated the doctoral research described here. Similarly, a single dissertation cannot definitively chronicle an ongoing program of research. In either case, one can only aspire to capture the essence of one's subject at a point in time. That has been my goal here. The PATRICK instrument is a powerful and versatile machine. Its development has led to the experimental realization of both optically driven Coulomb explosion and electron self-diffraction imaging. Development of the techniques will be continued by others at the National Research Council, the Advanced Laser Light Source, and – perhaps – elsewhere.